Formation and crystal-chemical studies of metastable and stable mullite-type aluminum borates

Dissertation

zur Erlangung des Doktorgrades der Naturwissenschaften (Dr. rer. nat.)

am Fachbereich Geowissenschaften

der Universität Bremen

vorgelegt von

Kristin Hoffmann

Kristallographie

Bremen, September 2016

Universität Bremen*

Reviewer:

Prof. Dr. Reinhard X. Fischer, Universität Bremen

Prof. Dr. Josef-Christian Buhl, Leibniz Universität Hannover

Date of public colloquium:

25 November 2016

This cumulative thesis is funded by the Deutsche Forschungsgemeinschaft (DFG), bonded to the grants **Fi442/19-1** and **GE1981/5-1** (Formation and crystal-chemical studies of metastable and stable mullite-type aluminum borates). It was carried out from October 2011 until September 2016 in a cooperated project of the faculties Geoscience and Chemistry/Biology at the University of Bremen.

Contents

Abstract

Aluminum borate compounds studied here belong to the family of mullite-type materials with the characteristic chains of edge-sharing octahedra. Depending on the individual phases the octahedral chains are linked by different arrangements of AlO_4- AlO_5-, BO_3- and eventually BO_4-polyhedra. This work is focused on the conditions of phase formation in the system Al_2O_3-B_2O_3, on the thermal and compositional stability ranges of the related phases and on their individual crystal-chemical characterization.

The formation of aluminum borate compounds synthesized from sol-gel derived precursors was investigated dependent on the initial Al/B ratio, with a special focus on the compositional range between the thermodynamically stable polymorphs $Al_4B_2O_9$ and $Al_{18}B_4O_{33}$. Upon increasing initial boron content a decrease of the formation temperature is observed, as revealed by thermal analyses. The formation of $Al_{6-x}B_xO_9$ compounds was observed for the compositional range of $1.09 \leq x \leq 2$ and the conditions of synthesis were optimized. The lattice parameters represent an orthorhombic metric with $a \neq b$, decreasing in all three directions with increasing boron content, most pronounced in **c**-direction. Based on Distance Least Squares (DLS) refinements, an improved model for $Al_{6-x}B_xO_9$ is presented, simulating a local geometry avoiding long B-O distances. In this model two octahedral chains are linked by planar BO_3 groups, yielding split positions for the oxygen atoms and strongly distorted octahedral chains.

The crystal structure of $Al_4B_2O_9$ was re-evaluated by electron diffraction experiments, resolving the question of oxygen disorder in the channels of the crystal structure. Inside crystallites the structural details vary. Domains are found with an ordered distribution of oxygen atoms without any significant signal for the second postulated channel oxygen atom O5, and other domains with a probable disordered configuration of the atoms O5 and O10. Diffuse scattering along the **b**-direction is assigned to a superstructure with a threefold **b**-axis.

For a series of samples with $Al_4B_2O_9$ structure a slightly increasing cell volume upon increasing initial boron content is observed. This is suggested to be caused by minor structural differences, which is supported by the results of Nuclear Magnetic Resonance (NMR) spectroscopy, revealing a small increase of the BO_4/BO_3 ratio upon increasing initial boron content.

A new study of $(Al_{1-x}Ga_x)_4B_2O_9$ compounds is presented is this thesis. For the first time the influence of foreign cations on the $Al_4B_2O_9$ and $Ga_4B_2O_9$ structure was investigated, representing a substitution limit of about 70 mol% Ga^{3+} and Al^{3+} in the $Al_4B_2O_9$ and $Ga_4B_2O_9$ structure, respectively. It is demonstrated that the thermal stability of a given member is a function of Al/Ga ratio in the crystal structure: increasing substitution of gallium reduces the decomposition temperature of $Al_4B_2O_9$ successively, whereas the incorporation of aluminum improves the thermal stability of $Ga_4B_2O_9$.

The compositional range for $Al_{18}B_4O_{33}/Al_{20}B_4O_{36}$ was investigated, based on a series of samples prepared along different synthesis routes and with various initial Al/B ratios. Combining the results of NMR spectroscopy and prompt gamma activation analysis (PGAA) a solid solution is assumed, expressed as $Al_{20-x}B_{4+x}O_{36}$ with Al substituting B in the range of about 1 – 3%. This is supported by powder diffraction data refinements, observing vacancies on the Al2 site by combining the data of neutron and X-ray powder diffraction. Furthermore, the results of X-ray diffraction experiments indicate disorder effects for samples synthesized from sol-gel precursors with a high amount of aluminum. This is supported by ^{27}Al NMR spectroscopy, representing a differing AlO_4/AlO_5 ratio for these samples, compared to samples synthesized with an excess of boron or prepared from solid-state reactions. The decomposition process of $Al_{20-x}B_{4+x}O_{36}$ is observed to start at 1473 K, revealed by thermal analysis and X-ray diffraction experiments. Complete decomposition takes place during a long-term experiment at 1673 K, confirming an incongruent melting of the Al-rich aluminum borate phase, yielding Al_2O_3 and liquid.

Zusammenfassung

Die hier untersuchten Aluminiumborate gehören zur Familie der Mullit-Typ Materialen, die sich durch die charakteristischen Ketten ecken-verknüpfter Oktaeder auszeichnen. Die individuellen Phasen weisen verschieden angeordnete AlO_4-, AlO_5-, BO_3- und eventuell BO_4-Polyheder auf, die die Oktaederketten verknüpfen. Die vorliegende Arbeit befasst sich mit der Phasenbildung im System Al_2O_3-B_2O_3, der thermischen Stabilität und der chemischen Zusammensetzung der Phasen sowie deren individueller kristallchemischer Charakterisierung.

Die Phasenbildung von Aluminiumboraten, synthetisiert über Sol-Gel Verfahren, wurde in Abhängigkeit vom Al/B Verhältnis der Ausgangsmaterialien untersucht. Ein spezieller Fokus lag auf dem Bereich der chemischen Zusammensetzung zwischen den thermodynamisch stabilen Polymorphen $Al_4B_2O_9$ und $Al_{18}B_4O_{33}$. Die thermische Analyse zeigt eine Abnahme der Bildungs-temperatur mit zunehmendem Boranteil im Ausgangsmaterial. Die Phasenbildung von $Al_{6-x}B_xO_9$ wird für $1.09 \leq x \leq 2$ beobachtet; die Synthesebedingungen wurden optimiert. Die Gitterparameter präsentieren eine orthorhombische Metrik für die $Al_{6-x}B_xO_9$-Phasen, wobei $a \neq b$ ist und eine Abnahme der Gitterparameter in allen drei Raumrichtungen mit zunehmendem Boranteil beobachtet wird. Diese Abnahme ist am stärksten in **c**-Richtung ausgeprägt. Auf Basis von Distance Least Squares (DLS) modeling wird ein verbessertes Kristallstrukturmodell für $Al_{6-x}B_xO_9$ präsentiert, wobei eine lokale Symmetrie simuliert wird, die zu lange B-O Atomabstände vermeidet. Dieses Modell basiert auf der Verbindung von zwei Oktaederketten durch eine planare BO_3 Gruppe, wodurch sich Split-Positionen für die Sauerstoff-Atome und eine starke Verzerrung der Oktaederketten ergeben.

Die Kristallstruktur von $Al_4B_2O_9$ wurde überarbeitet. Mittels Elektronenbeugungs-Experimenten konnte die Fragestellung nach der Unordnung der Sauerstoff-Atome in den Kanälen der Kristallstruktur gelöst werden. Innerhalb einzelner Kristallite gibt es strukturelle Unterschiede. Es wurden Domänen gefunden die eine geordnete Verteilung der Sauerstoff-Atome aufzeigen, ohne einen signifikanten Hinweis für das zweite Sauerstoff-Atom O5, während andere Domänen eine möglicherweise ungeordnete Anordnung der Atome O5 und O10 zeigen. Diffuse Streuung entlang der **b**-Richtung wird einer Überstruktur mit dreifach vergrößerter **b**-Achse zugeordnet.
Für eine Serie von Proben mit $Al_4B_2O_9$-Struktur wurde eine leichte Zunahme des Elementarzellen-Volumens mit zunehmendem Boranteil in der Ausgangszusammensetzung beobachtet. Es wird angenommen, dass diese Zunahme des Volumens auf geringfügige strukturelle Unterschiede zurückzuführen ist, was durch die Ergebnisse der Kernspinresonanzspektroskopie (NMR-Spektroskopie) gestützt wird, die eine leichte Zunahme des BO_4/BO_3 Verhältnisses mit zunehmendem Boranteil in der Ausgangszusammensetzung aufzeigen.

Diese Arbeit präsentiert erstmals Untersuchungen an $(Al_{1-x}Ga_x)_4B_2O_9$ Verbindungen. Der Einfluss von Fremdkationen auf die Kristallstruktur der Verbindungen $Al_4B_2O_9$ und $Ga_4B_2O_9$ wurde untersucht und zeigt ein Substitutions-Limit von etwa 70-mol% Ga^{3+} in $Al_4B_2O_9$ bzw. Al^{3+} in $Ga_4B_2O_9$ auf. Es wurde aufgezeigt, dass die thermische Stabilität der einzelnen Phasen als Funktion des Al/G Verhältnisses in der Kristallstruktur beschrieben werden kann: zunehmende Substitution von Gallium reduziert die Zersetzungstemperatur von $Al_4B_2O_9$ schrittweise, während der Einbau von Aluminium die thermische Stabilität von $Ga_4B_2O_9$ verbessert.

Die Variationsbreite in der chemischen Zusammensetzung von $Al_{18}B_4O_{33}/Al_{20}B_4O_{36}$ wurde für eine Serie von Proben in Abhängigkeit von den Synthesebedingungen in dem Al/B Verhältnis der Ausgangssubstanzen untersucht. Basierend auf den Ergebnissen aus NMR spektroskopischen Untersuchungen und prompt gamma activation Analysen (PGAA) wird eine Mischkristallreihe angenommen, ausgedrückt als $Al_{20-x}B_{4+x}O_{36,}$ wobei Aluminium Bor in einer Größenordnung von 1 – 3% substituiert. In einer kombinierten Verfeinerung von Neutronen- und Röntgen-Beugungsdaten werden Leerstellen auf der Al2 Position beobachtet, die diese Annahme unterstützen. Weiterhin deuten die Ergebnisse aus Röntgenbeugungsexperimenten auf Fehlordnungseffekte in Proben hin, die mittels Sol-Gel-Synthesen und einem hohen Anteil an Aluminium hergestellt wurden. Diese Effekte zeigen sich ebenfalls in den ^{27}Al NMR spektroskopische Untersuchungen, die ein leicht verändertes AlO_4/AlO_5 Verhältnis dieser Proben im direkten Vergleich mit den restlichen Proben aufzeigen, die mit einem Bor-Überschuss oder mittels Festkörperreaktion synthetisiert wurden. Die Kombination von thermischen Analysen und Röntgenbeugungsexperimenten zeigt auf, dass bereits bei einer Temperatur von 1473 K die Zersetzung von $Al_{20-x}B_{4+x}O_{36}$ beginnt. Für eine Temperatur von 1673 K wurde eine komplette Zersetzung in Langzeituntersuchungen beobachtet. Es wurde aufgezeigt das $Al_{20-x}B_{4+x}O_{36}$ inkongruent schmilzt, wobei Al_2O_3 und Schmelze als Zersetzungsprodukte auftreten.

1 General introduction

This thesis covers the formation and crystal chemistry of metastable and stable mullite-type aluminum borates in the Al_2O_3-B_2O_3 system. These aluminum borates belong to the family of mullite-type materials [1, 2] with the characteristic chain of edge-sharing MO_6 octahedra. With properties similar to mullite they are also termed as "boron-mullites" [3].

Mullite is a natural mineral with the general formula $3Al_2O_3 : 2SiO_2$, being reported to be the stable aluminosilicate in the Al_2O_3-SiO_2 system [4]. Due to its high temperature - low pressure formation conditions mullite occurs only rarely in nature [5]. However, mullite is an important material in advanced structural and functional ceramics due to a number of outstanding properties, such as low thermal expansion and conductivity and high creep resistance [6]. Commonly mullite is described to exist in a solid solution series with a compositional range of $Al_2(Al_{2+2x}Si_{2-2x})O_{10-x}$ with $0.18 \leq x \leq 0.82$, corresponding to 57-89 mol% Al_2O_3 [7]. An anisotropy relationship is observed between the *a* lattice parameter and the chemical composition, showing a linear decrease of a with increasing alumina content [7, 8]. The compositional stage of $x = 0$ refers to sillimanite (Al_2SiO_5), closely related to the crystal structure of mullite, those of $x = 1$ to Al_2O_3.

Mullite crystallizes in the orthorhombic space group *Pbam*. The fundamental building units in mullite are chains of edge-sharing AlO_6-octahedra running parallel to the **c**-axis. These chains are cross-linked by SiO_4 and AlO_4 tetrahedra, forming double chains along [001]. Whereas the SiO_4 and AlO_4 tetrahedra are strictly ordered in sillimanite, this is not the case for mullite where oxygen vacancies and tri-clusters of tetrahedra are present. An increasing number of oxygen vacancies occur in the mullite crystal structure with increasing Al content. This can be expressed with the substitution:

$2Si^{4+} + O^{2-} \rightarrow 2Al^{3+}$ + vacancy. As a result of this substitution tri-clusters of three MO_4 tetrehedra (M = Al, Si) are formed, leaving a vacancy at the position formerly occupied by the oxygen atom bridging two tetrahedra forming $(Al,Si)_2O_7$ groups [9], which is illustrated in Figure 1.1.

The topological arrangement of the AlO_4 chains[1] in mullite is a common feature, which represents a whole group of compounds, varying in their chemical composition. This group is designated as "mullite-type family", as mullite represents its most prominent member [1]. In the following part of chapter 1 the criteria for mullite-type structures as defined by Fischer and Schneider [1, 2] are specified. An overview about the boron containing mullite type compounds is given, with a focus on the linkage of the octahedral chains. Based on a literature review, the current state of knowledge is summarized and the motivation for this work is outlined and is leading to the central questions of this thesis, which are formulated in chapter 2.

[1] Because of the edge-sharing linkage of the MO_6 octahedra, always two neighboring octahedra share two O atoms. Therefore, the overall composition of the chain is MO_4.

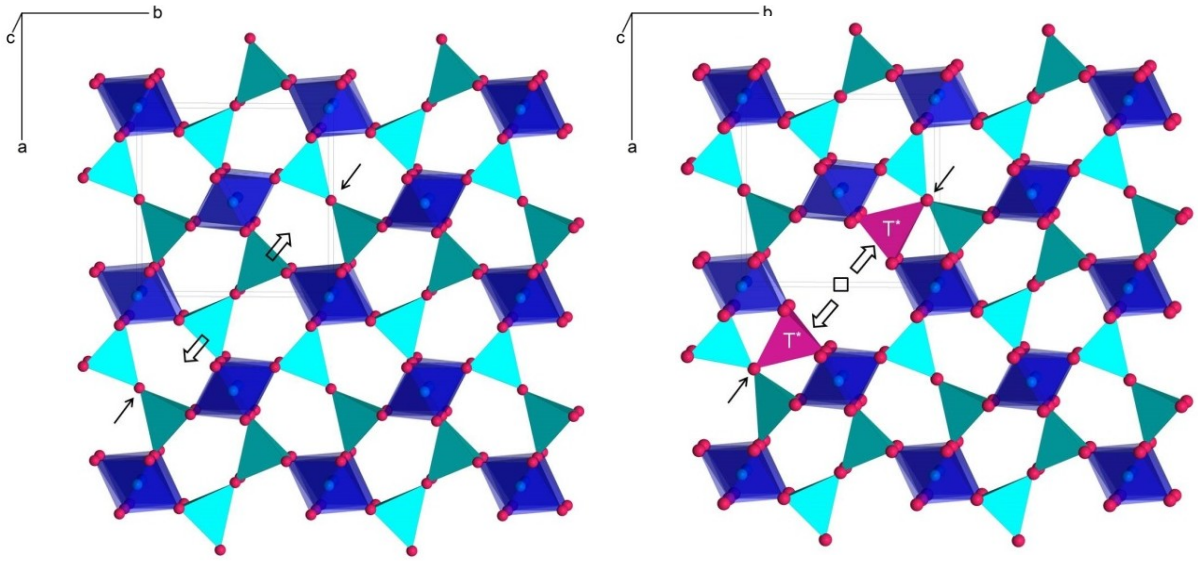

Figure 1.1: Crystal structure mullite solid solution compounds derived from sillimanite, presenting the linkage of the AlO_4 chains im sillimanite by T_2O_7 groups (a) and modelling of oxygen vacancies and tri-cluster forming (b). Migration direction of T atoms is presented by arrows. Modified after Fischer and Schneider [1]. Blue polyhdedra: AlO_6 octahedra, turquoise polyhedra: AlO_4/SiO_4 tetrahedra.

1.1 Classification of mullite-type crystal structures

The denotation „mullite-type“ includes all compounds which contain the characteristic chain of edge-sharing MO_6 octahedra, representing the fundamental structural unit in mullite [1]. The members of the “mullite-type family”, including natural and synthetic compounds, can have individual chemical compositions with various cations in the center of the octahedra and different arrangements of cations or cationic groups linking the octahedral chains. The following criteria were specified by Fischer and Schneider [1] to define the mullite-type structural arrangement[2] (see Fig.1.2):

1. “The space group of a mullite-type structure must be a subgroup of the aristotype in spacegroup P4/mbm.”

*2. “The chains of edge-sharing **M**O_6 octahedra (M = octahedrally coordinated cation) must be linear representing single Einer-chains in their highest topological symmetry in space group P4/mbm.”*

3. “The axis through the terminating atoms (non edge-sharing atoms) of the octahedra must point towards the edges (parallel to the chain direction) of adjacent octahedra ($30° \leq \omega \leq 90°$).”

4. “The chain structure should resemble the orthogonal metric of the aristotype perpendicular to the chain direction as closely as possible (angle $\gamma' = 90 \pm 5°$).”

[2] Criteria given from Fischer and Schneider (2005, p.1-2)

Fischer and Schneider [2] extended the fourth criterion by introducing and defining the two parameters Q_a and Q_r. Q_a specifies the "*ratio of the absolute values of the vectors enclosing γ'*" which should be close to 1. Q_r (given in %) represents "*the ratio of the ionic radius [10] of the octahedrally coordinated atom in the chains divided by the distance between neighboring chains*" and is a parameter to quantify the spacing between neighboring octahedral chains, which should be "*as close as the mullite-type linkages in a broad sense*".

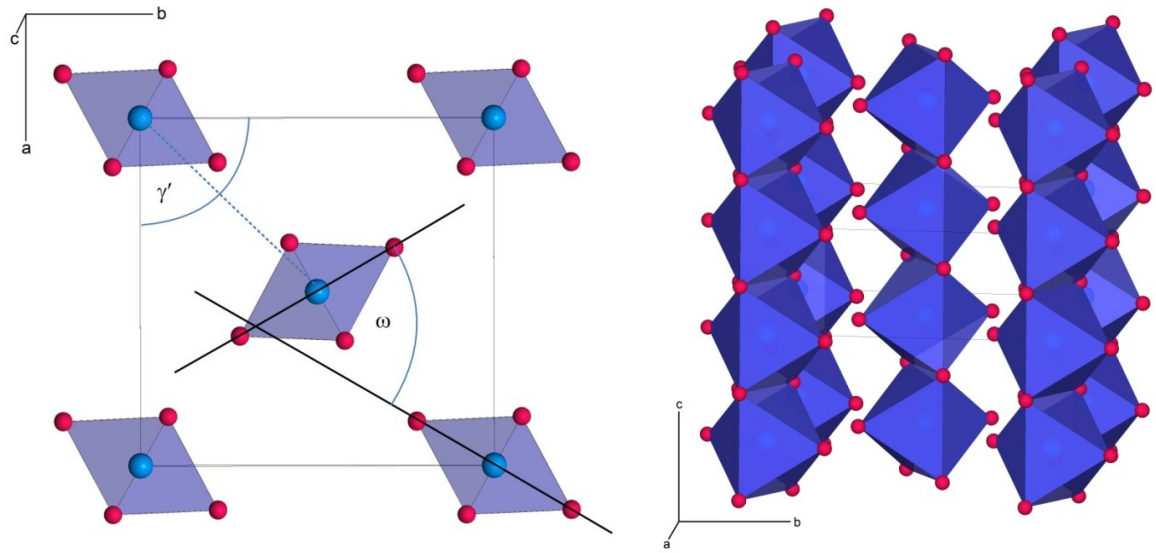

Figure 1.2: Crystal structure projections of mullite [11] exemplarily illustrating (a) the tilting angle ω between adjacent octahedral chains and the angle γ' between the projections of the basis vectors vertical to the chain direction; the dotted line represents the distance between octahedrally coordinated atoms, used for the calculation of the parameter Q_r (modified after Fischer and Schneider [2]) and (b) the characteristic octahedral chains along the **c**-direction.

1.2 Boron compounds in the mullite family

The mullite structure is able to incorporate varieties of foreign cations, including the element boron [12]. A comprehensive overview of foreign cation incorporation in mullite is given by Schneider [12]. The term "boron-mullite" or "B-mullite" was initially introduced by Werding and Schreyer [3] based on work reported by Scholze [13], who suggested a solid solution series between mullite and a silicon-free aluminum borate compound identified as $Al_{18}B_4O_{33}$. Consequently Werding and Schreyer [3] referred to this compound as "B-mullite". Later on this term was specified to a compositional range between the mullite solid solution series on the one hand and the aluminum borates Al_5BO_9 and $AlBO_3$ on the other hand (Figure 1.3) [14]. Not all compounds in the field of "boron-mullites" as defined by Werding and Schreyer [14] represent the characteristic mullite structure. Therefore Fischer and Schneider [2] recommended to designate all boron compounds which contain the characteristic mullite-type MO_4 chains as "mullite type boron compounds". In Figure 1.3 the chemical compositions

of all boron-mullite compounds are plotted within the ternary system Al_2O_3-B_2O_3-SiO_2 including $AlBO_3$, as this phase represents the corner point of the compositional range for "boron-mullites".
Several additional phases in the Al_2O_3-B_2O_3 system are mentioned in the literature whose existence is not proven yet or whose crystal structures are unknown so far. This includes the compounds $Al_8B_2O_{15}$, $Al_6B_4O_{15}$ and $Al_6B_8O_{21}$: $Al_8B_2O_{15}$ was first mentioned by Alley and Johnson [15] 1967 and later on by Reynaud [16], however no further structural investigation is available for this compound. The latter two compounds are described to be synthesized under hydrothermal conditions. $Al_6B_4O_{15}$ was described by Lehman and Teske [17] to crystallize in a tetragonal unit cell with unknown crystal structure; $Al_6B_8O_{21}$ was mentioned by Reynaud [16], however with doubtful existence.

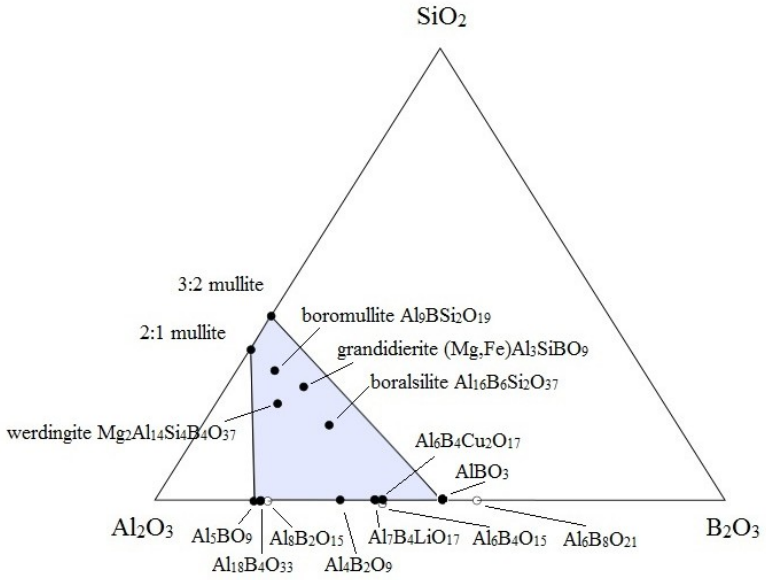

Figure 1.3: The ternary system Al_2O_3-B_2O_3-SiO_2, presenting the compositional range for "boron mullites", shown as light blue field, as defined by Werding and Schreyer [14]. Open circles refer to compounds with unknown crystal structure. Modified after Fischer and Schneider [2] and Fisch [18].

In the following an overview is given on the boron compounds in the mullite-type family. All structures are described in a standardized setting for a better comparison to mullite. A systematic description of the linkage of the mullite-type octahedral chains is given for the specific groups, summarized from Fischer and Schneider [2]:

MUL-IV.4, *I*4/*m*: $Al_6B_4Cu_2O_{17}$ group

This group includes the compounds $Al_6B_4Cu_2O_{17}$ [19] and $Al_7B_4LiO_{17}$ [20], both crystallizing in the tetragonal space group *I*4/*m* with aluminum as the representative cation in the characteristic octahedral chains. In the Cu-rich compound $Al_6B_4Cu_2O_{17}$ the AlO_4 chains are linked by BO_3 groups and $(Cu,Al)O_5$ bipyramids, thus forming $(Cu,Al)_4O_{13}$ clusters with one common O atom in the center of the cluster. In the Li-rich compound $Al_7B_4LiO_{17}$ the clusters solely contain aluminum atoms (Al_4O_{13}).

These clusters and disordered Li atoms are statistically distributed in the channels, which are empty in $Al_6B_4Cu_2O_{17}$. A slight "wave-like appearance" of the chains is observed for both, the Li and the Cu compounds, compared to mullite.

MUL-VIII.2, *Pbnm*: Grandidierite group

The group is represented by grandidierite ($(Mg,Fe)Al_3SiBO_9$), the Mg-rich member of the grandidierite - ominelite series. The crystal structure of grandidierite was determined by Stephenson and Moore [21], with AlO_4 chains linked by AlO_5 and MgO_5 bipyramids, as well as SiO_4 tetrahedra and BO_3 triangles. The crystal structure of the Fe-dominant analogue ominelite was determined by Hiroi et al. [22] to be isostructural with grandidieriete. Several minerals representing an intermediate composition were described by Dzikowski et al. [23].

MUL-II.3, *Pbam*: Mullite group

This group is mainly represented by a series of $Al_{6-x}B_xO_9$ ($1 \leq x \leq 3$) compounds, reported by Mazza et al. [24], who studied the substitution of aluminum against boron. Crystal structure refinements are reported for the two compounds with $x = 1$ and $x = 2$, described to crystallize in the orthorhombic space group *Pbam* with pseudo-tetragonal lattice parameters $a = b$ and an average structure close to mullite. The octahedral chains are linked by AlO_4, BO_4 or BO_3 groups, whereas boron substitutes aluminum with increasing boron content. Both compounds are described to be metastable, transforming to the thermodynamically more stable polymorphs $Al_4B_2O_9$ [25] and $Al_{20}B_4O_{36}$ [26].
Additionally, this group includes two compounds with the composition $Al_{8+x}P_{1-x}B_{1+x}O_{16+x/2}$ ($x = 0$ and $x = 0.6 \pm 0.1$) reported by Mazza et al. [27]. Boron is described to occur in three-fold coordination, no information is provided about the space group. However, the authors present the possible substitution of P and B for Si in 2:1 mullite [27].
Griesser et al. [28] presented a study on boron-doped mullite. A linear decrease of the lattice parameters with increasing initial B_2O_3 content is interpreted by the authors to be caused by an increasing substitution amount of boron into the crystal structure. Boron is confirmed in three-fold coordination, revealed by IR spectra, assuming an incorporation of about 20 mol%. Further studies on B-mullites were performed by Lührs et al. [29, 30], presenting the crystal structure of B-mullite with a replacement of silicon by boron and suggesting a substitution limit of about 15%.

MUL-IV.32, *Pbnm*: Sillimanite group

The sillimanite group is represented by a group of $PbMBO_4$ phases, with M = Al^{3+}, Ga^{3+}, Fe^{3+}, Cr^{3+} and Mn^{3+} [31-33]. The octahedral chains in $PbMBO_4$ are linked by BO_3 groups and four-fold coordinated Pb^{2+} atoms, distinguished by a lone-pair electron configuration. The incorporation of transition metals leads to specific magnetic behavior. The structural details of these compounds vary significantly compared to

sillimanite although they are reported to have the same symmetry. Boron-incorporation into the crystal structure of sillimanite (Al_2SiO_5) was investigated by Grew and Hinthorne [34] who reported an incorporation of about 0.43 wt% boron into the sillimanite structure, being too less to be determined in structural studies.

MUL-VIII.33, *Bb*2$_1$*m*: A$_9$B$_2$ (Al$_{18}$B$_4$O$_{33}$) group

This group is represented by the synthetic compound $Al_{18}B_4O_{33}$ and the mineral boromullite. $Al_{18}B_4O_{33}$ is the thermodynamically stable polymorph in the Al_2O_3-B_2O_3 system and due to its industrial utilization the most important aluminum borate compound. Commercially it is available under the trade names Alborex and Alborite (Shikoku Chemical Corporation, Japan). The octahedral chains of $Al_{18}B_4O_{33}$ are linked by AlO_5 bipyramids, AlO_4 tetrahedra and BO_3 triangles. The correct chemical composition and the thermal stability of this phase is an ongoing discussion (see chapter 1.3). Based on the idealized model $Al_{20}B_4O_{36}$ the $Al_{18}B_4O_{33}$ composition is obtained by a replacement of less than 2% of the Al atoms by B ($Al_{20}B_4O_{36}$ vs. $Al_{19.64}B_{4.36}O_{36}$) [26, 35].
The crystal structure of boromullite, presenting an ideal composition of $Al_9BSi_2O_{19}$ is described by Buick et al. [36]. It is described to be a 1:1 polysome of Al_5BO_9 and Al_2SiO_5 (sillimanite) with half of its structure consisting of sillimanite modules and the other half of Al_5BO_9 modules.

MUL-XVI.351, *B*112/*m*: Boralsilite and Al$_4$B$_2$O$_9$ group

This group is represented by the synthetic compound $Al_4B_2O_9$ and the mineral boralsilite. Boralsilite is represented by the ideal composition $Al_{16}B_6Si_2O_{37}$. Its crystal structure was determined by Peacor et al. [37] presenting an eightfold superstructure compared to mullite, with all lattice parameters doubled. The octahedral chains of boralsilite are linked by Si_2O_7 groups, BO_4 terahedra, BO_3 groups and AlO_5 bipyraminds. The synthetic analogue was successfully prepared by Grew et al. [38].
$Al_4B_2O_9$ is closely related to boralsilite with 2 Si + 1 O replaced by 2 B. Fischer et al. [25] determined the crystal structure of $Al_4B_2O_9$ in the monoclinic space group *C*2/*m*, with all lattice parameters doubled compared to the orthorhombic compound described by Mazza et al. [24].

MUL-XXXII.352, $P\bar{1}$: Werdingite group

This group is represented by the mineral werdingite with an ideal composition of $Mg_2Al_{14}Si_4B_4O_{37}$, determined by Moore et al. [39]. Further on, the occurrence of Fe-dominant analogues are reported by Grew et al. [40]. The pure Mg-compound was successfully synthesized by Werding and Schreyer [41]. The crystal structure is presented by AlO_4 chains, linked by either AlO_4 tetrahedra or BO_3 groups with $(Al,Fe)O_4$ and SiO_4 as well as AlO_5 and $(Fe,Mg)O_5$ bipyramids [42].

1.3 Thermal stability and chemical composition of selected phases in the Al_2O_3-B_2O_3 system

Based on literature study, this chapter covers the state of knowledge for the phases relevant for this work with respect to their thermal stability and chemical composition. In the binary phase diagram of Al_2O_3-B_2O_3 reported by Gielisse and Foster [43], the compounds $Al_4B_2O_9$ (A_2B) and $Al_{18}B_4O_{33}$ (A_9B_2) are described to be the thermodynamically stable phases (see Fig.1.4). In addition, Mazza et al. [24] published a series of compounds, with a composition given as $Al_{6-x}B_xO_9$ ($1 \leq x \leq 3$) having an average structures close to mullite.

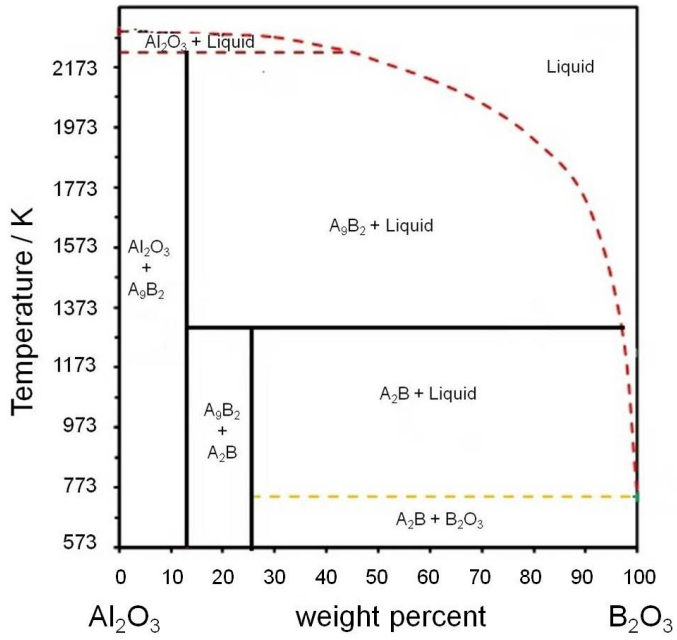

Figure 1.4: The binary phase diagram of Al_2O_3-B_2O_3, according to Gielisse and Foster [43].

The thermodynamically more stable polymorphs A_9B_2 and A_2B are of considerable research interest, because of their outstanding properties, such as low thermal expansion, high elastic modules and high tensile strength ([44] and references therein). The reinforcement of aluminum alloys by the incorporation of these aluminum borate whiskers in order to obtain composite materials with high mechanical strength is one of their most important applications ([44] and references therein). A further advantage of A_9B_2 is its favorable corrosion resistance against boron-rich glass melts, which makes it a suitable material for refractory linings [26]. Due to its low density it is further on used as lining on fire-proof doors in ships, and as fire-protection lining in nuclear plants due to its capability to absorb neutrons ([26] and references therein). However, although these compounds are particularly interesting for industrial applications, little is known about the exact conditions of formation, stability ranges and details of the crystal structures.

$Al_{6-x}B_xO_9$. Up to now no meaningful crystal chemical composition is available for these $Al_{6-x}B_xO_9$ compounds. The main difference in the crystal structures published for $x = 1$ and $x = 2$ is the substitution of one boron atom for one aluminum atom in the tetrahedral site [24]. Figure 1.5 exemplarily presents the crystal structure for $x = 1$, displaying possible arrangements for the linkage of the AlO_4 chains across several unit cells. The range of B-O distances in both crystal structures is 140 pm – 160 pm in case of BO_3 and 150 pm – 248 pm in case of BO_4, what is too large for a meaningful crystal-structure model. In contrast, the Al-O distances in the AlO_4 tetrahedra are unrealistically short for both compounds of the $Al_{6-x}B_xO_9$ series.

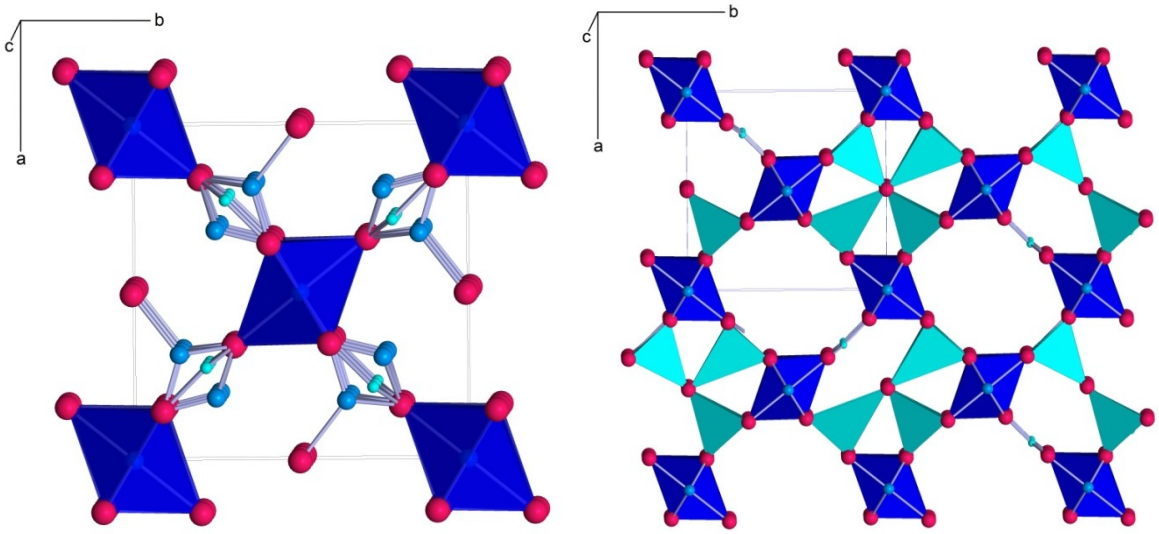

Figure 1.5: Crystal structures of mullite-type aluminum borate $Al_{6-x}B_xO_9$ with $x = 1$ (left), displayed with split positions; illustration of a possible structural arrangement (right). Blue polyhedra: AlO_6-octahedra, turquoise polyhedra: AlO_4-tetrahedra, green spheres: B (in BO_3-groups).

$Al_{18}B_4O_{33}$ / $Al_{20}B_4O_{36}$. The correct chemical composition of the Al-rich aluminum borate (Fig. 1.6, left) is an ongoing discussion. A solid solution between aluminum and boron is suggested. Primarily the Al-rich compound was reported to have $Al_{18}B_4O_{33}$ composition [13, 45]. Later on Sokolova et al. [46] performed crystal structure refinements in accordance with the previous results, however, calculating a unit cell content of $Al_{19.4}B_{4.6}O_{36}$ based on chemical analysis. Rounded to $Al_{20}B_4O_{36}$ this compound was further on referenced as Al_5BO_9, representing the idealized model with an ordered distribution of boron and aluminum. The $Al_{18}B_4O_{33}$ composition is obtained if about 2% of the aluminum in $Al_{20}B_4O_{36}$ is substituted by boron [26, 35]. However, this is difficult to be detected by diffraction methods. Gatta et al. [47] presented a study on the "pressure-induced structural evolution of Al_5BO_9" performing single crystal X-ray diffraction refinements thus representing a chemical composition better expressed in the compositional range close to Al_5BO_9. This was confirmed just recently by Fisch et al. [48].

The thermal stability of the Al-rich compound is discussed controversially in literature. Incongruent melting was observed at about 2223 K by Bauman and Moore [45] and at about 1713 K by Scholze [13]. Gielisse and Foster [43] investigated the thermal stability at 1923 K using sealed capsules. As they did not observe any fusion at 1923 K after a dwelling period of 6h they assumed that decomposition at 2223 K is more likely. Later on Rymon-Lipinski et al. [49] described a decomposition into Al_2O_3 and liquid B_2O_3 at 1473 K.

$Al_4B_2O_9$. Scholze [13] reported a B-rich aluminum borate compound crystallizing from a mixture of Al_2O_3 and B_2O_3 at 1273 K, assumed to have $2Al_2O_3$:B_2O_3 composition. An orthorhombic metric was indicated by the author, however, with unknown space group. Mazza et al. [24] described a compound with A_2B composition, assumed to be metastable, crystallizing in the orthorhombic space group *Pbam* with pseudotetragonal symmetry. In 2008 Fischer et al. [25] determined the monoclinic superstructure of A_2B in the space group *C*2/*m* (Fig. 1.6, right), using a combination of NMR spectroscopy and X-ray diffraction methods. The structure was solved in an enlarged unit cell with all lattice parameters doubled with respect to the *Pbam* structure given by Mazza et al. [24]. However, crystal chemical details of the structure concerning disorder of the channel oxygen atoms and of the interstitial cations have not been solved prior to this work. A_2B is reported by Gielisse and Foster [43] to be stable up to 1323 K, melting incongruently into $Al_{18}B_4O_{33}$ and a liquid phase [43]. This is in good agreement with the value of 1323 K ± 20 K, as given by Scholze [13].

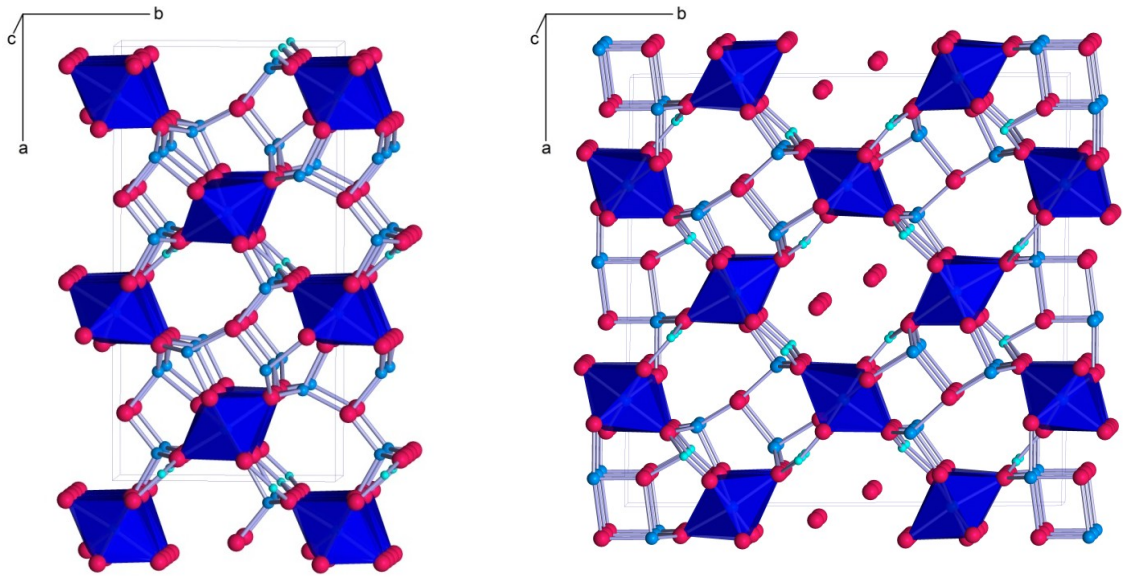

Figure 1.6: Crystal structures of mullite-type aluminum borates: $Al_{20}B_4O_{36}$ (left) presented in its *Bb*2_1*m* setting, transformed from the original setting in *A*2_1*am* [26] by P = (**b**, **a**, **-c**); $Al_4B_2O_9$ (right) presented in its *B*112/*m* setting transformed from the original setting in *C*12/*m*1 [25] by P = (**a**, **c**, **-b**). Blue polyhdedra: AlO_6-octahedra, blue spheres: Al (in AlO_4- or AlO_5-polyhedra), green spheres: B (in BO_3- or BO_4-polyhedra).

2 Research intention and Thesis outline

2.1 Scopes and objectives

The scope of this research work results from the DFG project "Formation and crystal-chemical studies of metastable and stable mullite-type aluminum borates". Based on the key points listed in the DFG proposal, the working program of the thesis was focussed on the following objectives:

Objective 1: The formation process of $Al_{18}B_4O_{33}$ (Al_5BO_9), $Al_4B_2O_9$ and $Al_{6-x}B_xO_9$

The study comprises the phase formation of mullite-type aluminum borate compounds in the chemical range up to 90 wt% initial B_2O_3, dependent on dwell period and heating temperature. A special focus is put on the chemical range between the two compounds $Al_{18}B_4O_{33}$ (Al_5BO_9) and $Al_4B_2O_9$. The investigation of these compounds applies differential thermal analysis (DTA) methods and high temperature X-ray diffraction (HT-XRD).

Objective 2: Detailed analysis of the crystal structure of $Al_4B_2O_9$ and analogous studies on $Ga_4B_2O_9$

Main task is the complete structure determination of the $Al_4B_2O_9$ crystal structure. Structural particularities have not been solved up to present, especially concerning the oxygen disorder and the boron environment. Therefore, investigations of structural details are carried out based on neutron powder diffraction (NPD) experiments and electron diffraction (ED) methods. Structural differences shall be studied by XRD experiments and ^{11}B and ^{27}Al Magnetic Angle Spinning Nuclear Magnetic Resonance (MAS NMR) spectroscopy dependent on the initial Al_2O_3/B_2O_3 ratio.
The phase formation of $(Al_{1-x}Ga_x)_4B_2O_9$ compounds is studied, including the substitution limit of Al^{3+} and Ga^{3+} into the $Al_4B_2O_9$ and $Ga_4B_2O_9$ structure, respectively. The thermal behavior of the crystalline materials is characterized.

Objective 3: Crystal structure analyses of the metastable compounds $Al_{6-x}B_xO_9$

A meaningful crystal-chemical description for the $Al_{6-x}B_xO_9$ compounds is developed. The only existing model represents B-O distances which are too large for a meaningful crystal structure model. Changes in the crystal structure are investigated by diffraction methods and NMR analyses dependent on the initial Al_2O_3/B_2O_3 ratio. The thermal stability is studied by HT-XRD.

Objective 4: The compositional and thermal stability range of $Al_{18}B_4O_{33}$ / $Al_{20}B_4O_{36}$

The study comprises the investigation of the chemical composition / compositional range of the Al-rich aluminum borate compound dependent on different synthesis routes and varying initial Al_2O_3/B_2O_3 ratios. Limits of a probable compositional range are investigated by chemical analysis and

NPD experiments. Structural differences are studied by XRD and NMR spectroscopy. The thermal stability is investigated up to 1773 K by DTA methods.

2.2 Thesis outline

This thesis is submitted as cumulative research work, based on three manuscripts, represented in chapter 4 - 6. The manuscripts represented in the chapters 4 and 5 are published in scientific journals, the one of chapter 6 will be submitted soon. A fourth manuscript related to this thesis is in preparation, in corporation with the University of Mainz, who reserves the right for publication; the corresponding samples were synthesized by K. Hoffmann. The abstract of that manuscript is attached in Appendix A.

Synthesis and characterization of mullite-type $(Al_{1-x}Ga_x)_4B_2O_9$

Kristin Hoffmann, M. Mangir Murshed, Reinhard X. Fischer, Hartmut Schneider and Thorsten M. Gesing

Published in: Z. Kristallogr. 2014; 229(10): 699–708

DOI: 10.1515/zkri-2014-1785

Formation, stability and crystal structure of mullite-type $Al_{6-x}B_xO_9$

Kristin Hoffmann, Thomas J. N. Hooper, M. Mangir Murshed, Oleksandr Dolotko, Zsolt Révay, Anatoliy Senyshyn, Hartmut Schneider, John V. Hanna, Thorsten M. Gesing and Reinhard X. Fischer

Published in: Journal of Solid State Chemistry, 2016; 243: 124-135

DOI: 10.1016/j.jssc.2016.08.018

Crystal chemical characterization of mullite-type aluminum borate compounds

Kristin Hoffmann, Thomas J. N. Hooper, Haishuang Zhao, Ute Kolb, M. Mangir Murshed, Michael Fischer, Hanna Lührs, Gwilherm Nénert, Petra Kudějová, Anatoliy Senyshyn, Hartmut Schneider, John V. Hanna, Thorsten M. Gesing and Reinhard X. Fischer

In preparation

Elucidating structural order and disorder phenomena in mullite-type $Al_4B_2O_9$ by automated electron diffraction tomography

Haishuang Zhao, Yasar Krysiak, Kristin Hoffmann, Bastian Barton, Leopoldo Molina-Luna, Reinhard Neder, Hans-Joachim Kleebe, Thorsten M. Gesing, Hartmut Schneider, Reinhard X. Fischer and Ute Kolb

In preparation

For unification purposes, units and denotations of figures and tables are standardized and references are adapted across the chapters compared to the original manuscripts. Further changes were added as footnotes. The three manuscripts (chapter 4 - 6) are written by Kristin Hoffmann, contributions are pointed out as followed:

The first manuscript (chapter 4)

Synthesis and characterization of mullite-type $(Al_{1-x}Ga_x)_4B_2O_9$

describes the characterization of mullite-type $(Al_{1-x}Ga_x)_4B_2O_9$ compounds. The formation of two different structures, $Al_4B_2O_9$ and $Ga_4B_2O_9$, is discussed, illustrating their atomic site relationship. The incorporation limit of Al^{3+} into the gallium borate structure and of Ga^{3+} into the aluminum borate structure is determined, respectively. Rietveld refinements are performed to represent the development of the lattice parameters and of the metal-oxygen distances with increasing incorporation level. The influence of the substitution on the thermal expansion and stability of both structures is determined. For a better comparison of the two structures the $Al_4B_2O_9$ structure is reported in this chapter in a setting which conforms to the mullite-type setting, different from the setting used in the previous and following chapters.

All syntheses, experiments and data evaluation were done by Kristin Hoffmann. Thermal expansion modelling was performed by Thorsten M. Gesing (Universität Bremen), the evaluation of decomposition temperatures was done by Lars Robben (Universität Bremen). The Figures 4.2, 4.5 and 4.6 are provided by Thorsten M. Gesing.

The second manuscript (chapter 5)

Formation, stability and crystal structure of mullite-type $Al_{6-x}B_xO_9$

studies the formation and thermal stability of aluminum borate compounds in the Al_2O_3-B_2O_3 system. The development of the lattice parameters is discussed for two series of samples, synthesized with different Al/B ratio in their initial gel composition. Structural changes are determined for samples with $Al_{6-x}B_xO_9$ structure, based on ^{11}B and ^{27}Al MAS NMR data. Rietveld refinements and distance least square modeling is performed to calculate split positions for the oxygen atoms, presenting a theoretically model restricted to the case that the octahedral chains are linked by a BO_3 group. The thermal expansion behaviour is modelled by Debye-Einstein-Anharmonicity (DEA) calculations, based on high temperature XRD- and low temperature neutron powder diffraction data.

Syntheses and experiments were performed by Kristin Hoffmann (sample series B) and Thorsten M. Gesing (sample series A). The neutron diffraction experiments at room temperature and low temperature were performed by Oleksandr Dolotko (FRM II, Garching) and Anatoliy Senyshyn

(FRM II, Garching). The PGA analysis was done by Zsolt Révay (FRM II, Garching). All NMR experiments and data fitting, including the related figures (Fig. 5.5 and 5.6) and parts of the text passages, were performed and provided by Thomas J. N. Hooper and John V. Hanna (University of Warwick). Figure 5.3 was provided by Thorsten M. Gesing, as well as the thermal expansion modeling, including Figure 5.9. The refinements of low temperature neutron diffraction data for the DEA fits and the corresponding text passage were provided by M. Mangir Murshed (Universität Bremen). All other experiments, data evaluation and processing were done by Kristin Hoffmann.

The third manuscript (chapter 6)

Crystal chemical characterization of mullite-type aluminum borate compounds

investigates the characterization of mullite-type aluminum borate compounds of two different structure types. The first aspect of the manuscript is the determination of the correct chemical composition of $Al_{18}B_4O_{33}/Al_{20}B_4O_{36}$. Two series of samples are compared, synthesized with different synthesis routes and initial Al/B ratios. Combining the results of powder diffraction refinements, PGA analysis and ^{11}B NMR spectroscopy a range for the substitution of Al by B is assumed. The thermal stability is discussed. The second part refers to the structure of the B-rich compound $Al_4B_2O_9$. Combining the methods of electron diffraction, powder diffraction Rietveld refinements and density-functional theory (DFT) calculations, the structure is re-investigated. A detailed structural description is given by ^{11}B and ^{27}Al NMR data.

All syntheses were done by Kristin Hoffmann. The neutron diffraction experiments were performed by Gwilherm Nénert (ILL, Grenoble) and Anatoliy Senyshyn (FRM II, Garching). The PGA analysis was performed by Petra Kudějová (FRM II, Garching). All NMR experiments and data fitting, including Figures 6.3, 6.4 and 6.10, were performed and provided by Thomas J. N. Hooper and John V. Hanna (University of Warwick). Electron diffraction experiments, including Figure 6.8, were performed and evaluated by Haishuang Zhao (Universität Mainz). DFT calculations and the related text passages were provided by Michael Fischer (Universität Bremen). Figure 6.6 was provided by M. Mangir Murshed (Universität Bremen). All other experiments, data evaluation and processing were done by Kristin Hoffmann.

3 Material and analytical methods

3.1 Synthesis of aluminum borate compounds

Series of samples were synthesized using the sol-gel synthesis [24] (glycerin method) or the common solid state reaction. Using the glycerine method the corresponding ratios of the nitrate reagents and boric acid were dissolved in glycerine at 353 K until a homogeneous low viscous slurry was obtained. The resulting foam was dried at 473 K, crushed into powder and finally heated at crystallizing temperature. Using the solid state reaction the stoichiometric mixtures of the oxide reagents were grained, pressed as a pellet and finally crystallized at high temperature. All samples were crystallized in covered platinum or corundum crucibles. To remove possible impurities of amorphous B_2O_3 they were washed with hot deionized water. The used chemicals are given in Table 3.1. Detailed information is given in the respective chapters.

Table 3.1: Chemicals used for the synthesis of aluminum borate compounds

Chemical	Chemical formula	Purity	Producer
Aluminum nitrate nonahydrate	$Al(NO_3)_3 \cdot 9H_2O$	99.2%	VWR Chemicals
		≥ 98%	Fluka
Gallium nitrate hydrate	$Ga(NO_3)_3 \cdot xH_2O$	99.99%	abcr
Boric acid	$B(OH)_3$	≥ 99.8%	Merck
^{11}B Boric acid	$^{11}B(OH)_3$	≥ 99 at% ^{11}B	Sigma-Aldrich
Aluminum oxide	α-Al_2O_3	99%	Alfa Aesar
Boron oxide	B_2O_3	≥ 97%	Fluka
1,2,3-Propantriol Glycerol	$C_3H_8O_3$	99.5 %	VWR Chemicals

3.2 Instruments, methods and software

A number of analytic methods were performed on the synthesized samples and/or on the precursor material. Here, a brief summary about the used methods and instruments is listed, including the corresponding evaluation software. Detailed information and measuring parameters are given in the respective chapters.

Powder Diffraction

X-ray Powder Diffraction

X-ray powder-diffraction experiments were carried out for all samples, using two instruments in the group Crystallography, Department of Geoscience (University of Bremen):

Measurements were performed at the Philips X'Pert diffractometer (Panalytical, Almelo, Netherlands) in Bragg-Brentano geometry with $CuK\alpha_{1,2}$ radiation (tube settings: 45 kV, 40 mA). The instrument is equipped with an 0.25° divergence slit, an 0.5° anti scatter slit, a soller slit (0.04 rad) and a masc (10 mm) in the primary beam, as well as with a soller slit (0.04 rad), a Ni-filter and a X'Celerator detector system in the secondary beam. For high temperature experiments the instrument is additionally equipped with the high-temperature chamber HTK1200N (Anton Paar, Vienna, Austria).
Measurements at the Bruker D8 diffractometer (Bruker AXS GmbH, Karlsruhe, Gemany) were performed in Debye-Scherrer geometry using a primary Johansson type Ge(111)-monochromator and glass capillaries for small amounts of sample. The instrument is equipped with an antiscatter slit (0.1 mm) and a soller slit (4°) in the primary beam, as well as a soller slit (2.5°), an iris aperture (6.42 mm) and a position sensitive detector (LynxEye) in the secondary beam. Two different radiation sources were used: monochromatic $CuK\alpha_1$ radiation (λ = 154.06 pm, tube settings: 40 kV, 40 mA) and monochromatic $MoK\alpha_1$ radiation (λ = 70.93 pm, tube settings: 50 kV, 40 mA).
Data evaluation was performed using the the "DiffracPlus Topas 4.2" (Bruker AXS GmbH, Karlsruhe, Germany) software.

Neutron Powder Diffraction

Neutron powder-diffraction (NPD) experiments were carried out for selected samples, enriched with ^{11}B. NPD experiments were performed as boron has a low scattering factor and therefore cannot be located accurately from X-ray powder diffraction data. Two different instruments were used, located at the FRM II (Garching) and at the Institut Laue Langevin (Grenoble), respectively:
Measurements at the FRM II were performed at ambient conditions and at low temperature (LT) on the powder diffractometer SPODI. The instrument is equipped with a Ge(551)-monochromator, with a take-off angle of 155°. Room temperature measurements were performed by O. Dolotko and A. Senyshyn in high-resolution mode with a wavelength of λ = 155.01(1) pm and λ = 154.838(2) pm, respectively. LT experiments were performed by A. Senyshyn, using a closed cycle cryostat and a wavelength of λ = 154.81(1) pm.
Measurements at the Institut Laue Langevin (ILL) were performed at room temperature by G. Nénert. The instrument is equipped with a Ge(335)-monochromator (λ = 159.4 pm).
Rietveld refinements were carried out using the "DiffracPlus Topas 4.2" (Bruker AXS GmbH, Karlsruhe, Germany) software. Difference Fourier calculations including the corresponding Rietveld refinements were performed using the BRASS [50] software.

Electron Diffraction

Electron diffraction experiments were performed at room temperature by H. Zhao in the Institute of Inorganic Chemistry and Analytical Chemistry (University of Mainz), using a TECNAI F30 S-TWIN transmission electron microscope.

Magnetic Angle Spinning Nuclear Magnetic Resonance (MAS NMR) Spectroscopy

MAS NMR spectroscopy experiments were performed by the NMR group of the Department of Physics (University of Warwick). The ^{11}B MAS NMR measurements were carried out on a Varian-600 spectrometer, acquired at a magnetic field of 14.1 T and a frequency of 192.50 MHz. The ^{27}Al MAS NMR measurements were performed at a Bruker Avance II+-600 spectrometer or a Bruker Avance 400 spectrometer, using magnet fields of 14.1 T and 9.40 T and frequencies of 156.34 MHz and 104.23 MHz, respectively. The simulation of the spectra was performed with the DMFit program [51] and/ or the QuadFit program [52].

Infrared (IR) Spectroscopy

Fourier-transform infrared (FTIR) spectra were collected in the Solid State Chemical Crystallography group, Department of Chemistry (University of Bremen) on a Bruker Vertex 80v FTIR spectrometer. The main intention was the qualitative proof of boron in its different coordination environments.

Raman Spectroscopy

Powder Raman spectra were carried out in the Solid State Chemical Crystallography group, Department of Chemistry (University of Bremen), on a Horiba LabRam Aramis spectrometer. Spectra were collected at room temperature using a laser of $\lambda = 532.04$ nm wavelength. The main intention was the qualitative proof of boron in its different coordination environments. Data evaluation was performed using the LabSpec software, version 5.

Differential Thermal Analysis (DTA)

Thermal analyses were performed in the group Crystallography, Department of Geoscience (University of Bremen) on a Netzsch 449 F3 Jupiter STA (Netsch GmbH, Selb, Germany), combining the signals of differential scanning-calorimetry (DSC) and thermal gravimetric analysis (TG). Dry synthetic air atmosphere was used for all measurements. Data evaluation was performed with the Proteus Netzsch software [53].

Prompt Gamma Activation Analysis (PGAA)

Quantitative boron analytic is still difficult, as boron is not detectable with X-ray fluorescence spectrometers [54]. Just recently it was shown by Söllradl et al. [55] that PGAA is a suitable method to analyse boron-bearing samples. PGA Analyses were performed by P. Kudějová and Zs. Révay at the FRM II (Garching), using Hypermet-PC [56] and the ProSpeRo [57] program for data evaluation.

Additional Software

All crystal structure drawings were performed using the program Struplo, included in the BRASS [50] software package. Distance Least Squares modelling was performed using the DLS program [58].

4 Synthesis and characterization of mullite-type $(Al_{1-x}Ga_x)_4B_2O_9$

Kristin Hoffmann[a,b], M. Mangir Murshed[b], Reinhard X. Fischer[a], Hartmut Schneider[c], Thorsten M. Gesing[a,*]

[a]Kristallographie, FB05, Universität Bremen, Klagenfurter Straße, 28359 Bremen, Germany
[b]Chemische Kristallographie fester Stoffe, Institut für Anorganische Chemie, Universität Bremen, Leobener Straße /NW2, 28359 Bremen, Germany
[c]Institut für Kristallographie, Universität Köln, Greinstraße 6, 50939 Köln, Germany

Published in: Z. Kristallogr. 2014; 229(10): 699–708
DOI: 10.1515/zkri-2014-1785

Submitted: 01.07.2014; accepted: 19.08.2014; online: 01.10.2014

*corresponding author; email address: gesing@uni-bremen.de; phone: +49 (0)421 218 63140; fax: +49 (0)421 218 98 63140

Abstract

Mullite-type $(Al_{1-x}Ga_x)_4B_2O_9$ compounds were synthesized using the glycerine method. The end members $Al_4B_2O_9$ and $Ga_4B_2O_9$ were produced at different temperatures. Starting from the $Al_4B_2O_9$ composition the incorporation limit of Ga ranges between 60 - 70 mol%, while starting from $Ga_4B_2O_9$ the Al incorporation limit is 70 mol% in the $Ga_4B_2O_9$ structure. The crystal structures were refined from the X-ray powder diffraction data and analyzed by the Rietveld method. The positions of B atoms were determined by distance least squares modeling. The temperature-dependent investigations demonstrate that the stability of a given member is a function of Al/Ga ratio in the structure. The incorporation of Ga in the $Al_4B_2O_9$ structures leads to a successive decrease of the decomposition temperatures. Pure $Al_4B_2O_9$ decomposes above 1323 K, whereas pure $Ga_4B_2O_9$ is stable up to 1073 K. The thermal expansions of the lattice parameters were fit using extended Grüneisen first-order approximation for the zero-pressure equation of state. Changes of the internal energy of the crystal were calculated by the Debye-Einstein-Anharmonicity model. The thermal stability of each member has been explained in terms of the obtained Debye temperature.

Keywords: chemical synthesis; inorganic compounds; mullite-type structure; thermal expansion; X-ray diffraction.

4.1 Introduction

The aluminum borate $Al_4B_2O_9$ and the gallium borate $Ga_4B_2O_9$ belong to the family of mullite-type materials [1, 2] with the characteristic chain of edge-sharing MO_6 (here M = Al, Ga) octahedra. Aluminum borates with properties similar to mullites ($Al_{4+2x}Si_{2-2x}O_{10-x}$), are also termed as "boron-mullites" [3]. The compound $Al_4B_2O_9$ (A_2B) represents an important material due to its usage as whiskers in oxidation-resistant reinforced composites or chemical and heat-insulating materials [44] (and references therein). For A_2B two different polymorphs are reported. Mazza et al. [24] describe an A_2B form in the orthorhombic space group *Pbam* with pseudo-tetragonal lattice parameters $a = b$ and an average structure close to mullite. Fischer et al. [25] determined the monoclinic superstructure using a combination of NMR spectroscopy and X-ray diffraction methods in the space group *C*2/*m*. The structure was solved in an enlarged unit cell with all lattice parameters doubled with respect to the *Pbam* structure [25]. The crystal structure of $Ga_4B_2O_9$ (G_2B) is described by Cong et al. [59] in the same space group *C*2/*m*, but with a crystal structure and lattice parameters distinctly different from that of A_2B (see chapter 2 – structural relationships). The crystal structures of A_2B and G_2B are reported here in the *B*112/*m* and *I*112/*m* settings, respectively, which conform to the mullite-type setting [1], for a better comparison of the two structures. This results in an orientation of the characteristic mullite octahedral chains parallel to the **c**-axis, and $\gamma = 90.43°$ corresponds to the monoclinic angle instead of $\beta = 135.24°$ for the G_2B structure in its C-centered setting.

Here, we report on the synthesis and characterization of a series of $(Al_{1-x}Ga_x)_4B_2O_9$ compounds produced at two different temperatures. The aim of this work is to study the incorporation of gallium into the A_2B structure compared to the incorporation of aluminum into the G_2B structure. We explain the formation of two different structures with two ions, Al^{3+} and Ga^{3+}, however, with similar crystal-chemical properties.

4.2 Structural relationships

The crystal structures of the two compounds A_2B and G_2B are represented in their standardized settings as subgroups of the mullite aristotype structure in *P*4/*mbm,* with the octahedral chains running parallel to the **c**-axis (see [1, 2] for more details). The Bärnighausen tree illustrates the symmetry relationships in this branch of the mullite-type family as shown in Figure 4.1; the atomic site relationships are given in Table 4.1. The designations of cations and oxygen atoms in the octahedral chains are derived from the corresponding name in the aristotype appended by numbers and characters. Therefore, the position of oxygen atom O1 in the aristotype, e.g., is split into an O11 and O12 site in the subgroup followed by further splitting into O11a1 and O11a2 etc. in A_2B. Consequently, the crystal structure of A_2B is presented here in *B*112/*m* as a subgroup of *I*112/*m*, representing the standard setting of the G_2B structure. The transformation matrices transforming the

crystal structures from their original settings in *C*12/*m*1 are P = (**a**, **c**, **-b**) in the case of A_2B and P = (**-a-c**, **c**, **b**) with an origin shift of **p** = (0, 0, -1/2) in the case of G_2B. It should be noted, that all atom names following given, refer to the standardized ones, as given in the Tables 4.1-3.

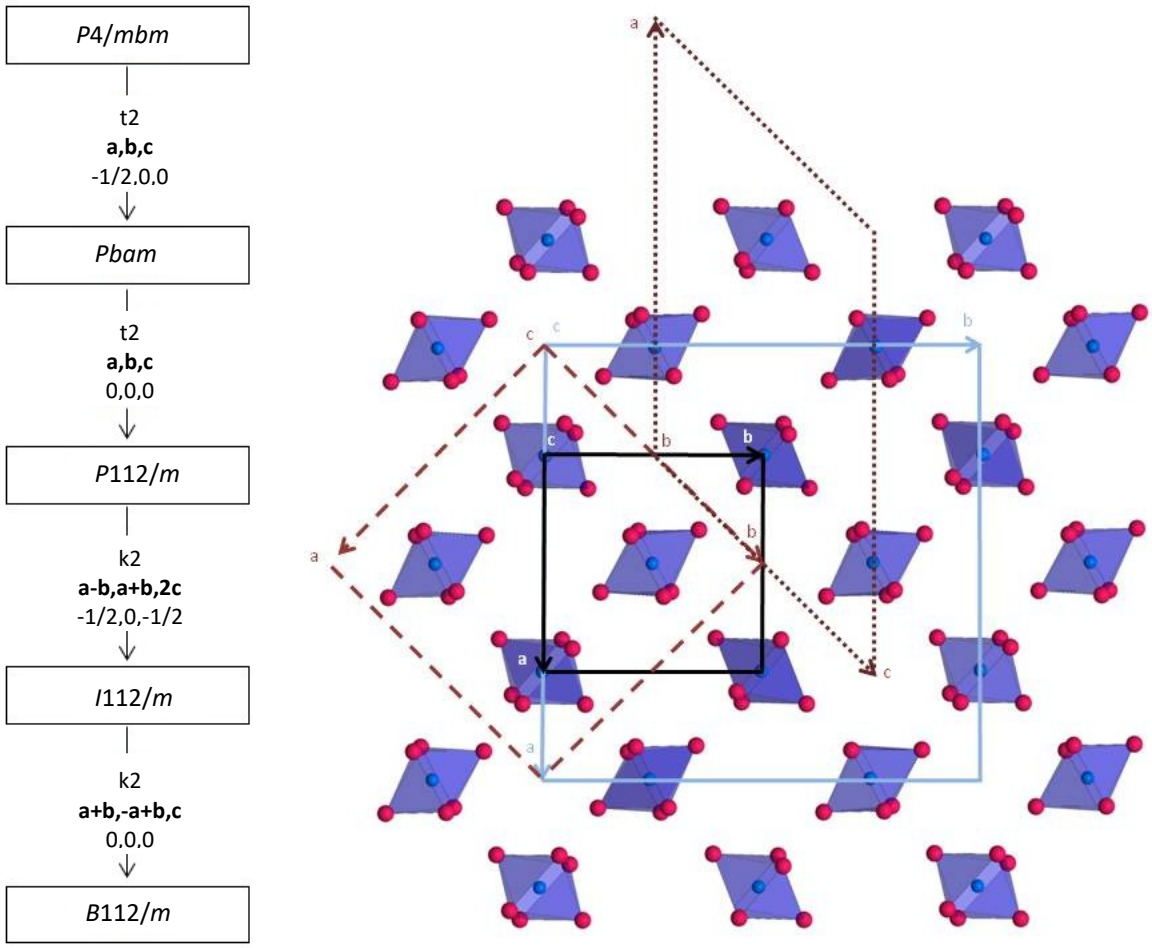

Figure 4.1. The Bärnighausen tree illustrating the group-subgroup relations of this branch of the mullite family (left), showing the symmetry relationships between $Al_4B_2O_9$, $Ga_4B_2O_9$, and mullite structures. The projection of the octahedral chains is based on the $Al_4B_2O_9$ structure [25]. The dark solid line represents the unit cell of mullite (*Pbam*), the light blue line corresponds to the A_2B structure in its mullite-type setting (*B*112/*m*), the dotted line corresponds to the G_2B structure in its first reported setting (*C*12/*m*1) [59] and the dashed line refers to the unit cell of G_2B in its mullite-type setting (*I*112/*m*) (right).

The characteristic structural units in both A_2B and G_2B are the octahedral chains parallel to the **c**-axis. These chains are cross-linked by BO_3 and BO_4 groups and by AlO_4 and AlO_5 groups in A_2B (Fig. 4.2 left, Table 4.2), and solely by GaO_5 in G_2B (Fig. 4.2 right, Table 4.3). As already mentioned by Cong et al. [59], the main difference between the A_2B and the G_2B structure is the order-disorder arrangement of the interchain-groups, which are more ordered in the A_2B structure. According to Cong et al. [59], the positions of Al2 and Al4 in A_2B have similar local environments to those of Ga3

and Ga4 in G_2B, excluding their disordered distribution. Analogously, Al3 and Al5, basically four-coordinated in A_2B, but with an additional longer bond, correspond to Ga2 in a highly distorted bi-pyramid with four short and one long Ga-O bond [59].

Table 4.1. Atomic site relationships for $Al_4B_2O_9$ and $Ga_4B_2O_9$ derived from the tetragonal aristotype.

P4/mbm	Pbam (mullite)	P112/m	G_2B, I112/m	G_2B, original name	A_2B, B112/m	A_2B original name
M1 [2d]	Al1 [2a]	M11 [1a]	M11 [4e]	Ga2	M11a [4e]	Al6
					M11b [4f]	Al7
		M12 [1g]	M12 [4f]	Ga1	M12 [8j]	Al5
O1 [4h]	O1 [4h]	O11 [2n]	O11a [4i]	O4	O11a1 [4i]	O12
					O11a2 [4i]	O3
			O11b [4i]	O2	O11b1 [4i]	O13
					O11b2 [4i]	O14
		O12 [2n]	O12a [4i]	O1	O12a1 [4i]	O8
					O12a2 [4i]	O2
			O12b [4i]	O3	O12b1 [4i]	O15
					O12b2 [4i]	O6
O2 [4g]	O2 [4g]	O21 [2m]	O21 [8j]	O6	O21a [8j]	O7
					O21b [8j]	O11
		O22 [2m]	O22 [8j]	O5	O22a [8j]	O4
					O22b [8j]	O9
[1]	[1]	[1]	[this work]	[24]	[this work]	[58]

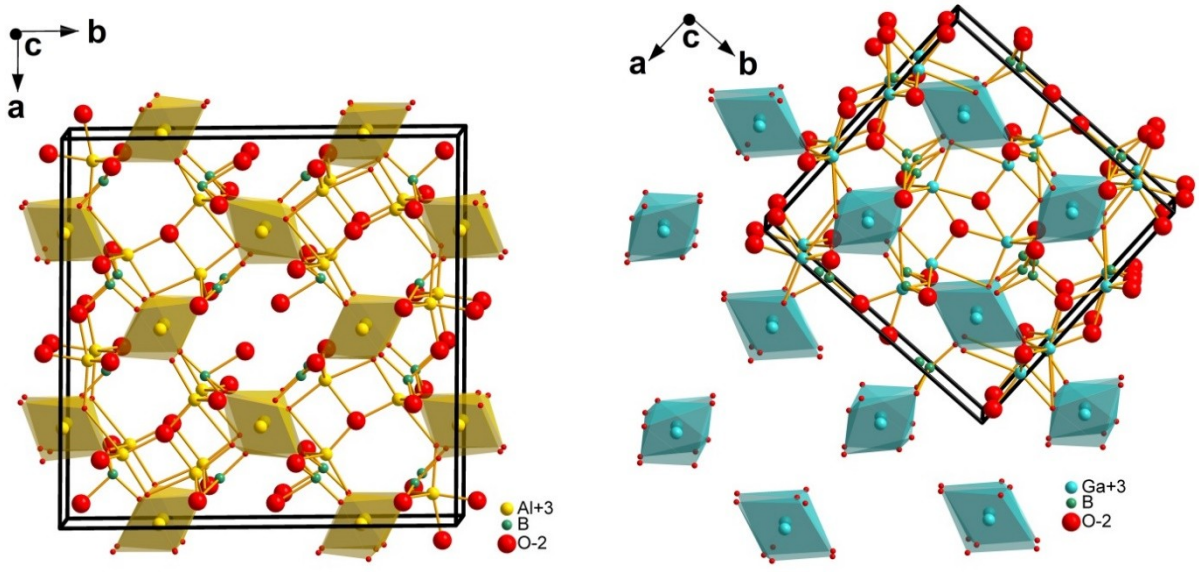

Figure 4.2. Projection of the crystal structure of $Al_4B_2O_9$ [25] represented in its *B*112/*m* setting (left), transformed from the original setting in *C*12/*m*1 by P = (**a**, **c**, -**b**) and of $Ga_4B_2O_9$ [59] represented in its *I*112/*m* setting (right), transformed from the original setting in *C*12/*m*1 by P = (-**a**-**c**, **c**, **b**) and **p** = (0, 0, -1/2). The oxygen atoms in the octahedra are reduced in size for better clarity.

Table 4.2. Refined atomic positional parameters for $Al_4B_2O_9$ in space group $B112/m$ (12) with a = 1479.20(6) pm, b = 15028.3(5) pm, c = 553.46(2) pm, γ = 90.9657(17)° and V = 1230.17(7) 10^{-6} pm^{-3}.

Atom	Std	Ox	W	S	SOF	x	y	z	B /10^{-4} pm^2
Al1	Al2	3	4i	m	1	0.86302(67)	0.34176(57)	0	0.35(22)[a]
Al2	Al3	3	4i	m	1	0.81186(69)	0.15646(68)	0	0.35(22)[a]
Al3	Al4	3	4i	m	1	0.56949(63)	0.06830(58)	0	0.35(22)[a]
Al4	Al5	3	4i	m	1	0.67248(71)	0.33848(69)	0	0.35(22)[a]
Al5	Al12	3	8j	1	1	0.99800(66)	0.24489(51)	0.2501(19)	0.35(22)[a]
Al6	Al11a	3	4e	-1	1	1/4	0	3/4	0.35(22)[a]
Al7	Al11b	3	4f	-1	1	1/4	1/2	3/4	0.35(22)[a]
B1	B1	3	4i	m	1	0.1090(26)	0.1051(24)	0	0.4
B2	B2	3	4i	m	1	0.3743(25)	0.1231(24)	0	0.4
B3	B3	3	4i	m	1	0.1243(25)	0.3547(22)	0	0.4
B3	B4	3	4i	m	1	0.3870(27)	0.3935(23)	0	0.4
O1	O3	-2	4i	m	1	0.7580(15)	0.2629(11)	0	0.61(25)[b]
O2	O12a2	-2	4i	m	1	0.7897(13)	0.4337(12)	0	0.61(25)[b]
O3	O11a2	-2	4i	m	1	0.9150(14)	0.22014(98)	0	0.61(25)[b]
O4	O22a	-2	8j	1	1	0.92558(76)	0.35213(73)	0.2758(25)	0.61(25)[b]
O5p	O4	-2	4i	m	0.5	0.0612(27)	0.4558(24)	0	0.61(25)[b]
O6	O12b2	-2	4i	m	1	0.3247(15)	0.4580(13)	0	0.61(25)[b]
O7	O21a	-2	8j	1	1	0.81840(77)	0.10581(70)	0.2727(24)	0.61(25)[b]
O8	O12a1	-2	4i	m	1	0.6923(13)	0.0604(13)	0	0.61(25)[b]
O9	O22b	-2	8j	1	1	0.06657(81)	0.12995(71)	0.2216(28)	0.61(25)[b]
O10	O5	-2	4i	m	0.5	0.4494(27)	0.0436(24)	0	0.61(25)[b]
O11	O21b	-2	8j	1	1	0.66781(79)	0.40105(69)	0.7095(24)	0.61(25)[b]
O12	O11a1	-2	4i	m	1	0.5714(15)	0.2811(11)	0	0.61(25)[b]
O13	O11b1	-2	4i	m	1	0.4390(14)	0.1911(11)	0	0.61(25)[b]
O14	O11b2	-2	4i	m	1	0.0621(13)	0.2913(12)	0	0.61(25)[b]
O15	O12b1	-2	4i	m	1	0.8276(14)	0.9551(12)	0	0.61(25)[b]

Std, standardized atom name; Ox, formal valence; W, Wyckoff symbol; S, site symmetry; SOF, site occupation factor, and isotropic displacement parameter B.
[a,b]Parameters with the same letter are linearly constrained to each other.

Table 4.3. Refined atomic positional parameters for $Ga_4B_2O_9$ in space group *I*112/*m* (12) with a = 1080.92(12) pm, b = 1099.28(12) pm, c = 571.43(5) pm, γ = 90. 5468(99)° and V = 678.97(12) 10^{-6} pm^{-3}.

Atom	Std	Ox	W	S	SOF	x	y	z	B /10^{-4} pm^2
Ga1	Ga12	3	4f	-1	1	3/4	1/4	1/4	0.75
Ga2	Ga11	3	4e	-1	1	3/4	3/4	1/4	0.75
Ga3	Ga2	3	4i	m	1	0.01446(69)	0.84068(53)	0	0.75
Ga4	Ga3	3	4i	m	0.5	0.21975(92)	0.0175(12)	0	0.75
Ga5	Ga4	3	4i	m	0.5	0.3519(10)	0.0007(13)	0	0.75
B1	B1	3	4i	m	1	0.81791	0.48745	0	0.50
B2	B2	3	4i	m	0.5	0.49690	0.25273	0	0.50
B3	B3	3	4i	m	0.5	0.50595	0.21322	0	0.50
O1	O12a	-2	4i	m	1	0.8533(25)	0.7843(27)	0	1.03
O2	O11b	-2	4i	m	1	0.2028(30)	0.8542(24)	0	1.03
O3	O12b	-2	4i	m	1	0.3761(27)	0.2646(27)	0	1.03
O4	O11a	-2	4i	m	1	0.7827(25)	0.3651(29)	0	1.03
O5	O22	-2	8j	1	1	0.5861(15)	0.2726(14)	0.2229(35)	1.03
O6	O21	-2	8j	1	1	0.7882(15)	0.5622(13)	0.1950(36)	1.03
O7	O3	-2	4i	m	0.5	0.0617(46)	0.0042(82)	0	1.03
O8	O4	-2	4i	m	0.5	0.4917(68)	0.9274(40)	0	1.03

Std, standardized atom name; Ox, formal valence; W, Wyckoff symbol; S, site symmetry; SOF, site occupation factor, and isotropic displacement parameter B.[3]

4.3 Experimental methods

4.3.1 Synthesis

Powder samples [$(Al_{1-x}Ga_x)_4B_2O_9$ - A] with the A_2B crystal structure were synthesized using the glycerine method described in [61]. The corresponding ratios of $Al(NO_3)_3 \cdot 9H_2O$, $Ga(NO_3)_3 \cdot 7H_2O$ and $B(OH)_3$ were dissolved in 10 wt% glycerine at 353 K until a homogeneous low viscous slurry was obtained. The reduction of the metal nitrates caused by the added glycerine is indicated by the ascent of brownish NO_x gases accompanied by evaporation of water. The resulting foam was dried at 473 K

[3] Table 4.3: modified reproduction from 60. Hoffmann, K., M.M. Murshed, R.X. Fischer, H. Schneider, and T.M. Gesing (2014): *Synthesis and characterization of mullite-type* $(Al_{1-x}Ga_x)_4B_2O_9$. Zeitschrift für Kristallographie - Crystalline Materials, **229**(10): p. 699-708.

for 2 hours, crushed into powder and finally crystallized at 1223 K for two days in a covered platinum crucible. Remaining boric acid, which was used with a small excess during the synthesis, was removed by washing the powder with hot deionized water.
For the powder samples [$(Al_{1-x}Ga_x)_4B_2O_9$ - G] with the G_2B crystal structure, the synthesis was modified according to Cong et al. [59], using a solid-state reaction. Accordingly, $Ga(NO_3)_3 \cdot 7H_2O$, $Al(NO_3)_3 \cdot 9H_2O$ and $B(OH)_3$ were intensively ground and crystallized with an excess of boric acid at 923 K for 5 hours in an open porcelain crucible. Again boric acid was identified as an additional phase and removed by washing the powder with hot deionized water.

The incorporation of aluminum and gallium cations in all samples was proven by energy dispersive X-ray spectroscopy (EDX) for A_2B and G_2B structure, respectively. EDX data were recorded on a Jeol JSM-6510 scanning electron microscope [Jeol (Germany) GmbH, Echingen, Germany] with a Bruker QUANTAX spectrometer using an excitation voltage of 20 kV.

4.3.2 Powder X-ray diffraction at ambient temperature

Powder X-ray diffraction data were collected at room temperature on a Bruker D8 diffractometer (Bruker AXS GmbH, Karlsruhe, Gemany) in Debye-Scherrer geometry using a primary Johansson type Ge(111)-monochromator and capillaries of 0.5 mm in diameter. The instrument was equipped with an antiscatter slit (0.1 mm) and a soller slit (4°) in the primary beam, as well as a soller slit (2.5°), an iris aperture (6.42 mm) and a position sensitive detector (LynxEye) in the secondary beam. Two different radiation sources were used. For monochromatic $CuK\alpha_1$ radiation (λ = 0.15406 nm, 40 kV, 40 mA) data were collected in a range from 5 - 120° 2θ, with a step size of 0.02° and a measuring time of 16 s per step. And, for monochromatic $MoK\alpha_1$ radiation (λ = 0.07093 nm, 50 kV, 40 mA) data were collected in the range from 5 - 60° 2θ, with a step size of 0.02° and a measuring time of 120 s per step. Rietveld refinements for all collected data were carried out using the “DiffracPlus Topas 4.2” (Bruker AXS GmbH, Karlsruhe, Germany) software. The fundamental parameter approach was used for all refinements. The fundamental parameters for each configuration were fitted against a LaB_6 standard sample and fixed the associated parameters during the refinements.

In case of powder samples [$(Al_{1-x}Ga_x)_4B_2O_9$ - A] with the A_2B type crystal structure, data were collected using $CuK\alpha_1$ radiation. For the A_2B end member, general parameters (zero point of the counter, scale factor, background) as well as lattice parameters, average crystallite size, micro-strain and atomic coordinates were refined. Constrains were applied setting the atomic displacement parameters of the metal atoms as well equal as those of the O atoms. The displacement parameters of the B atoms were fixed to values taken from Fischer et al. [25].

For the powder samples [$(Ga_{1-x}Al_x)_4B_2O_9$ - G] with the G_2B crystal structure, data were collected using $MoK\alpha_1$ radiation. As we found the impurity of gallium oxide decreased by reducing the crystallization

time, this sample was used for the characterization of the G_2B end member. Refinements were carried out following the A_2B structure type solid solution. The atomic displacement parameters were fixed for all atoms (values were taken from [59]). The theoretical boron positions were again calculated by DLS modeling and fixed in the Rietveld refinements. Possible positions for B atoms obtained from DLS calculations still have distances to O atoms being too long. This could be avoided by assuming local distortions of the O atoms in the octahedra.

4.3.3 High-temperature X-ray diffraction

The thermal stability and expansion of the crystalline powder samples were studied by means of high-temperature X-ray powder diffraction between 298 K and 1423 K on a Philips X'Pert diffractometer (Panalytical, Almelo, Netherlands), equipped with the high-temperature chamber HTK1200N (Anton Paar, Vienna, Austria), using $CuK\alpha_{1,2}$ radiation. The instrument was equipped with an 0.25° divergence slit, an 0.5° anti scatter slit, a soller slit (0.04 rad) and a masc (10 mm) in the primary beam, as well as with a soller slit (0.04 rad), a Ni-filter and a X'Celerator detector system in the secondary beam. Data were collected from 5 to 120° 2θ, with a step-size of 0.017° and a measuring time of 120 s per step for $Al_4B_2O_9$ and from 10 to 80° 2θ, with a step size of 0.017° and a measuring time of 180 s per step for $Ga_4B_2O_9$. The temperature was increased stepwise in 50 K steps. Data were evaluated using Rietveld refinements as described above.

All samples were characterized between ambient conditions and 1423 K by means of Rietveld refinements based on high-temperature X-ray powder diffraction data. The lattice parameters of samples in both series were refined using the Pawley method up to an incorporation of 70 mol% of the corresponding atom. Notably, the X-ray pattern did not show an accurate decomposition point, because decomposition proceeded during the measurement.

Decomposition temperatures of the A_2B series were determined using the autocorrelation (AC) analysis [62] of the diffraction data between 15° and 17° 2θ (Cu). The intercept point between the linear developments of the Corr-Norm parameter of synthesized phase with those of decomposition product was used as decomposition temperature.

4.4 Results and discussion

The well crystallized pure A_2B was found in its *B2/m* polymorph with the crystal structure described by Fischer et al. [25] with lattice parameters *a*, *b*, *c* slightly smaller than the reported ones. For the G_2B series the structure model of Cong et al. [59] was used. The lattice parameters, average crystal size L_{Vol}(IB) and micro-strain ε_0 of all crystalline samples were refined using the Pawley method. Figure 4.3 shows the variation of the unit-cell volumes of A_2B and G_2B solid solutions as a function of

the initial gallium content. In order to compare the parameters, the volume of G_2B was doubled corresponding to the same number of 8 formula units per unit cell as in A_2B.

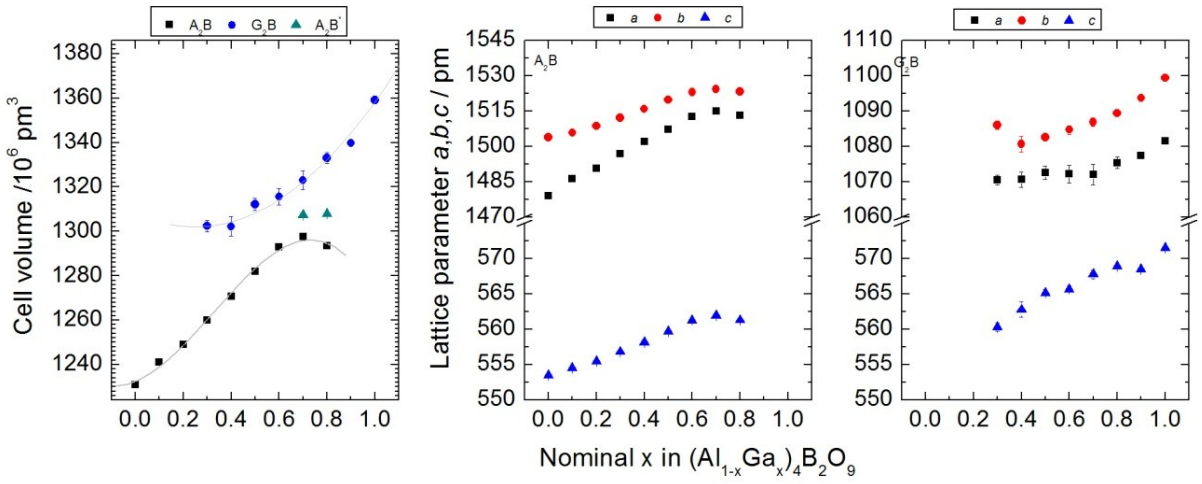

Figure 4.3. Unit-cell volume of A_2B and doubled unit-cell volume of the G_2B structure type solid solution and the corresponding lattice parameter of A_2B (middle) and G_2B (right) as a function of the initial content of aluminum and gallium.[4]

Up to an initial weight of 70 mol% gallium could be successfully incorporated into the A_2B structure. The successive expansions of the unit-cell volume caused by the expansion of all three lattice parameters can be observed for A_2B with an increasing amount of gallium, indicating the successful incorporation of gallium into the A_2B structure. Between 40 - 60 mol% gallium, a small hump at about 14° 2θ (MoKα) could be observed in the X-ray pattern. As Ga_2O_3 has two reflections of high intensity in this area, there is a high probability that these reflections belong to a small amount of gallium oxide. Above approximately 60 mol% gallium incorporation into the A_2B structure the lattice parameters do not further increase and Ga_2O_3 clearly started appearing as an additional phase in the samples. The incorporation limit of gallium in the A_2B structure was estimated to be between 60 mol% and 70 mol% gallium. Due to the scattering from amorphous gallium components in the X-ray pattern of gallium-doped A_2B it is difficult to determine how much of the initial content of Ga is really incorporated in the synthesis. Therefore, the incorporation limit with respect to the synthesis conditions might be assumed to be slightly higher. Similarly, a decrease of the unit-cell volume and lattice parameters is observed for the G_2B structure with an increasing initial amount of aluminum instead of gallium. The incorporation limit of aluminum into G_2B produced at 873 K is approximately 70 mol% as well (Fig. 4.3). Alike the findings in the A_2B series the small hump at about 14° 2θ

[4] Figure 4.3: modified reproduction from 60. Hoffmann, K., M.M. Murshed, R.X. Fischer, H. Schneider, and T.M. Gesing (2014): *Synthesis and characterization of mullite-type* $(Al_{1-x}Ga_x)_4B_2O_9$. Zeitschrift für Kristallographie - Crystalline Materials, **229**(10): p. 699-708.

(MoKα) was observed in the X-ray pattern for G_2B samples with a small content of aluminum, which most probably belongs again to gallium oxide. For the G_2B end member it was observed that the impurity of gallium oxide decreased by quenching the samples in air. Pure G_2B crystallizes at 923 K. The higher reaction temperature results in decomposition into $GaBO_3$ and Ga_2O_3 [59]. In contrast, pure A_2B crystallizes at about 1223 K, and a reaction temperature below 1073 K produces amorphous products. For Ga-doped A_2B, which was finally heated at 1223 K, Ga_2O_3 can be observed as a second phase if the incorporated gallium content gets beyond a critical value of > 60 mol%. For an initial gallium content of 70 mol% in A_2B, a modification of the synthesis by lowering the reaction time (25 h) and the synthesis temperature (1013 K) shows a slight increase of the unit-cell volume indicating a higher gallium incorporation. For Al-doped G_2B, finally heated at 923 K, an amorphous product is formed if the incorporated aluminum content in G_2B gets beyond a critical value of > 70 mol%.

4.4.1 A_2B structure

Based on the structure model of Fischer et al. [25], Ga was assumed to partially replace Al on the M-sites. The corresponding site occupancies were constrained to full occupancies in the Rietveld refinements as found in the Al end member. These refinements were performed analogously up to an incorporation of 60 mol% Ga in A_2B structure. The crystallographic parameters of these refinements are deposited at FIZ Karlsruhe with the CSD numbers 428199, 428202 – 428207. The positions of the B atoms could not be refined except for the A_2B end member. Therefore, theoretical boron positions were calculated by „Distance Least Squares“ (DLS) modeling [58], and the corresponding values were fixed in the Rietveld refinements. The DLS-calculated B positions yield average B-O distances for a trigonal planar coordination in a range of 139 pm - 155 pm, significantly higher than 137 pm expected from the sum of the ionic radii [10]. It might be possible that B also resides in four fold coordination or the O atoms of the octahedra are locally displaced shifted closer to the B atoms, which is difficult to determine from X-ray powder diffraction data, but has been observed in B-doped mullite [30].
Throughout the Ga-doped A_2B series, most of the metal-oxygen distances (termed as M-O, M: Al, Ga) linearly increase as a function of the Ga incorporation, except the M11b-O and M4-O distances both of them decreasing with some scattering (Fig. 4.4). This might be due to an incorporation-induced deformation of the respective polyhedra. This is a clear indication for the incorporation of the bigger Ga atoms into the A_2B structure. The refined occupancy parameters on mixed Al/Ga positions confirm this trend. The resulting occupancies for the octahedral positions are comparable to that of the five-coordinated M2 position. The refined positions of the channel oxygen atom O4 moves closer to the M2 position upon increasing the Ga content. According to Fischer et al. [25], O4 is considered to be a representative of scattering matter that cannot be assigned to a well-defined position, and it represents

a terminal O in an unfavorable position with a rather long bond to B3. However, with increasing content of Ga, the channel atom O4 is refined to come in coordination with M2, whereas the O3 atom, being responsible for the formation of so called tri-clusters, shifts away from the M2 position.

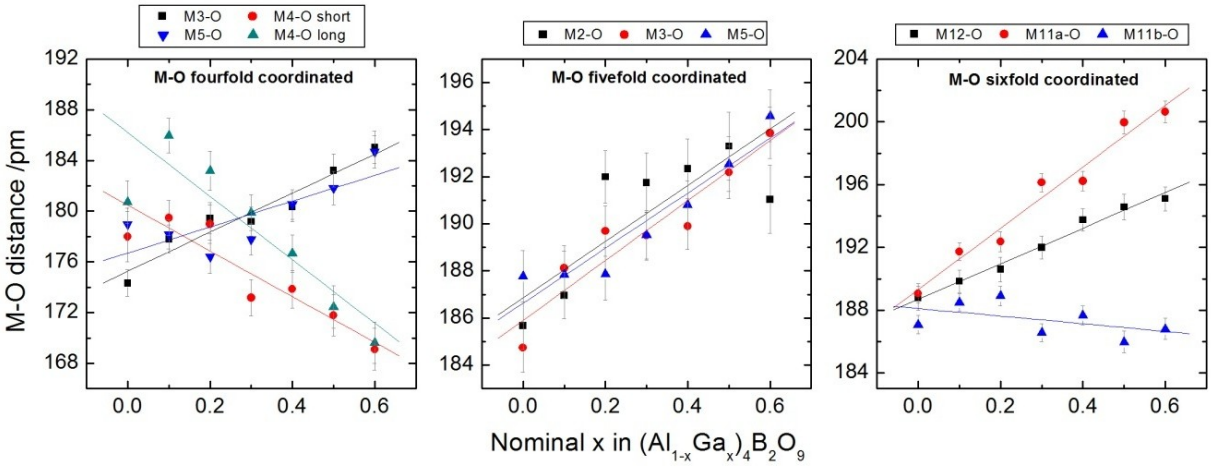

Figure 4.4. Variation of the average metal-oxygen distances for the fourfold (left), fivefold (middle) and sixfold (right) oxygen coordination of the metal atoms in the A_2B structure type solid solution.

The occupancies for the M3 and M5 positions were refined to low Al/Ga values representing a preferred occupancy of gallium in these positions. The refined occupancy for the M4 position yields Ga at this position as well, but the mean metal-oxygen distance in this MO_4 tetrahedron decreases upon Ga incorporation, however, independent from the gallium content, this MO_4 tetrahedron is highly distorted. The local environments of the metal atoms in $[(Al_{1-x}Ga_x)_4B_2O_9 – A]$ were evaluated by bond-valence sum (BVS) calculations, using the bond valance parameters (r_0), tabulated by Brese and O'Keeffe [63]. For the M3 and M5 positions, the BVS calculations indicate a preference for five-fold coordination for a high Ga content.

4.4.2 G_2B structure

All samples of the G_2B-series show a poor degree of crystallinity and a major amorphous content, accumulating with an increase of the aluminum content, aggravating successful structure refinements for samples with an initial composition containing more than 10 mol% aluminum. Based on the structure model of Cong et al. [59], Al was assumed to partially replace Ga on the M sites. The corresponding site occupancies were constrained to full occupancies in the Rietveld refinements. The refined crystallographic parameters are listed in the corresponding files deposited at FIZ Karlsruhe (CSD# 428200 and 428201).

4.4.3 Thermal expansion and stability

Pure A_2B decomposes to $Al_{18}B_4O_{33}$ (A_9B_2) + B_2O_3 above 1323 K. The incorporation of Ga atoms in the A_2B structure leads to a decrease of the decomposition temperature. Pure G_2B is reported to be stable up to 923 K [59] before it decomposes to the binary oxides. However, we found the stability of G_2B slightly at a higher temperature between 1073 K and 1123 K. In contrast to the findings in Ga-doped A_2B, Al-incorporation into the G_2B structures leads to an increasing stability with decomposition temperature (Table 4.4).

Table 4.4. Decomposition temperatures and average linear thermal expansion coefficients between 573 K and 1073 K of the phases. Thermal expansion for [29, 64, 65] is given between 573 K and 1273 K.

Sample/ Series	Foreign cation content /mol%	Decomposition Temp. /K	Thermal expansion coefficients /10^{-6} K^{-1}				Anisotropy factor A /10^{-6} K^{-1}
			α_{11}	α_{22}	α_{33}	α_{12}	
A_2B	0	1283(25)	10.0(4)	7.7(3)	4.5(3)	0.15(7)	10.9(8)
	10	1063(25)	8.6(3)	8.3(2)	4.3(3)	0.08(6)	8.6(6)
	20	1186(25)	9.0(3)	8.1(2)	5.0(3)	-0.01(6)	8.0(6)
	30	1156(25)	8.4(2)	7.8(2)	4.2(2)	-0.38(5)	8.2(5)
	40	1107(25)	9.7(3)	8.5(3)	3.4(3)	-0.68(8)	12.5(7)
	50	958(25)	8.8(3)	8.5(2)	3.7(3)	-0.82(6)	10.2(7)
	60	955(25)	9.6(2)	8.7(2)	4.1(2)	-1.00(5)	11.0(5)
	70	1032(25)	9.7(3)	8.8(3)	3.6(3)	-1.2(1)	12.3(7)
G_2B	0	1073-1123	8.0(3)	9.0(3)	1.5(3)	0.8(2)	15.0(7)
	10	1123-1173	9.1(5)	10.2(4)	3.7(5)	1.0(4)	12.9(11)
	20	1123-1173	7(2)	8.5(6)	3.3(7)	-0.2(8)	10.4(29)
Mullite [64][a]			4.1	6.0	5.7		
Mullite [65][a]			3.9	7.0	5.8		6.2
B-Mullite [29][a]	13.6[b]		4.6(1)	5.3(1)	5.0(1)		

In all cases the correlation coefficient of the corresponding fit parameter was large than 0.938 indicating the suitability of the selected fit function. A_2B decomposition temperatures are from AC analysis and by visual inspection of the diffraction data for G_2B.
[a]Instead of tensor components thermal expansion coefficients are reported, [b]Foreign cation boron.

Mullite in general shows a low thermal expansion, which is one of its most important properties for potential industrial interests. The thermal properties of mullite were well investigated [6], showing a

nonlinear expansion below 573 K followed by a linear expansion between 573 K and 1273 K. One can describe the linear thermal expansion of the unit-cell volume of pure A_2B and G_2B up to the beginning of decomposition. This expansion has been mainly caused by the expansion in the crystallographic **a**- and **b**-direction, while the *c*-lattice parameter parallel to the mullite-type octahedral chains remain nearly constant. Moreover, the monoclinic angle γ slightly decreased. Fisch and Armbruster [66] determined the thermal behavior for A_2B between 298 K and 1323 K, finding the largest expansion for the **a**-axis followed by the **c**- and **b**-axes accompanied by a slight decrease of the monoclinic angle. As they represent the A_2B structure in its *C*2/*m* setting, where the **b**-axis corresponds to the **c**-axis in the *B*2/*m* setting and vice versa, this is in good agreement to our approximation. They described the thermal expansion of the A_2B structure using a second order polynomial.

For Ga-doped A_2B, the thermal expansion of the crystallographic **c**-direction is low, while those parallel to the **b**- and **a**-direction, which are almost in the same range, are higher. The monoclinic angle increases up to the decomposition temperature for samples with Ga > 20 mol%. For Al-doped G_2B the expansion behavior is similar, whereas for an increasing Al content a better description of expansion could be given by a fourth order polynomial. The monoclinic angle γ remains almost constant. For a better comparison to mullite, the tensor components of the linear thermal expansion coefficients are given for all samples showing a more or less linear thermal expansion behavior between 573 K and their decomposition temperature (Table 4.4). Due to the unconventional setting of the space group (see introduction), the **c**-axis conforms to the unique axis, the angle γ is between the axes **a** and **b**. The associated tensor coefficients are thus given by:

$$\alpha_{11}(T) = \frac{1}{a_0 \sin\gamma_0}\left[\sin\gamma\ \frac{\Delta a}{\Delta T} + a\cos\gamma\ \frac{\Delta\gamma}{\Delta T}\right]$$

$$\alpha_{22}(T) = \frac{1}{b_0}\frac{\Delta b}{\Delta T}$$

$$\alpha_{33}(T) = \frac{1}{c_0}\frac{\Delta c}{\Delta T}$$

$$\alpha_{12}(T) = \frac{1}{a_0}\frac{\Delta a}{\Delta T}\left[\frac{1}{\sin 2\gamma_0} - \frac{\sin\gamma}{2\cos\gamma_0}\right] - \frac{a\cos\gamma}{2\,a_0 cos\,\gamma_0}\frac{\Delta\gamma}{\Delta T} - \frac{cot\,\gamma_0}{2b_0}\frac{\Delta b}{\Delta T}$$

$$\alpha_{13}(T) = 0$$

$$\alpha_{23}(T) = 0$$

(Δ denoted the respective difference between 573 K and 1073 K.)

One should note that this description offers the possibility to compare the current findings to the values technically used for the description of the thermal expansion. A physically meaningful model using Grüneisen first order approximation is additionally given for the gallium doped A_2B series.

4.4.4 Thermal expansion modelling

To get intrinsic energy information on the crystalline phases the thermal expansion of solids can be adequately modeled using Grüneisen first order equation of state for zero pressure, where the internal energy of the crystal is calculated using both Debye quasi-harmonic and Einstein harmonic models [67]. Whereas in the Einstein model the atoms in a solid are independent oscillators and free from other sources of dynamical entropy, the Debye quasi-harmonic model assumes independent oscillators, however, with altered frequencies. None of the thermal expansion coefficients (TEC) of the lattice parameters saturate (holding a constant value) at a temperature-independent region for the observed range (Fig. 4.5, inset), which is assumed to be associated with intrinsic anharmonicity leading to anisotropic and anomalous thermal expansion (Note, that in such cases a description of the thermal expansion using a linear thermal expansion coefficient for the whole temperature range is meaningless). During the modeling of the thermal expansion of the unit-cell volume neither a single Debye nor a single Einstein term (d = 1, e = 1, $k_A = 0$) led to reasonable fits of the observed data. An additional anharmonicity term along with a single Debye frequency (d = 1, e = 0, k_A) well fit the data in the following form:

$$M(T) = M_0 + \sum_{i=1}^{d} k_{Di}\, U_{Di}(T) + \sum_{i=1}^{e} k_{Ei} U_{Ei}(T) + k_A U_A(T) \qquad (1)$$

where *M(T)* refers to any of the temperature-dependent metric parameters (*V(T)*, *a*(*T*), *b*(*T*) and *c*(*T*)), k_{Di}, k_{Ei} and k_A are adjustable fitting parameters representing thermoelastic information, contributing to Debye (U_{Di}), Einstein (U_{Ei}) and anharmonic (U_A) internal energies, respectively. The fitting procedure suggests that the anharmonicity rapidly increases with increasing temperature, and its contribution started probably below room temperature. Clearly, the Debye phonon spectrum cannot adequately describe the expansion in the whole range (Fig. 4.5). The calculated Debye temperatures are linearly correlated to the amount of gallium incorporated into the A_2B structure as given in Figure 4.6. Assuming that the initial gallium content used for the synthesis of these compounds was fully incorporated into the structure the decomposition temperature of the samples is a linear function of the gallium content. In this regard, the decrease of the decomposition temperature agrees well with the direct observations from the high-temperature X-ray data.

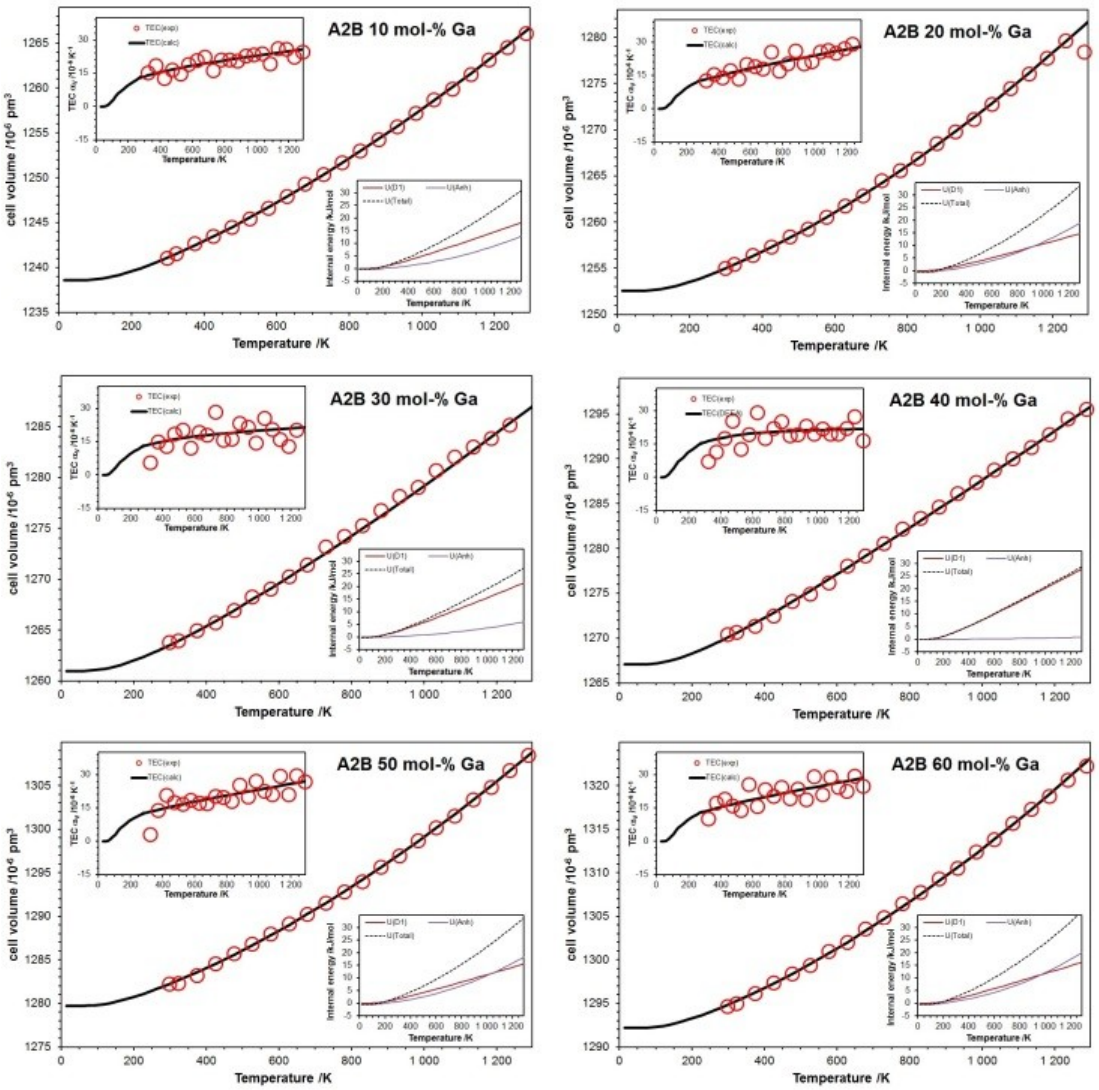

Figure 4.5. Debye-Anharmonicity model fittings of the A_2B structure type $[(Al_{1-x}Ga_x)_4B_2O_9$ - A] series of the temperature-dependent volume behavior. Estimated standard deviations of the observed data are within the symbol.

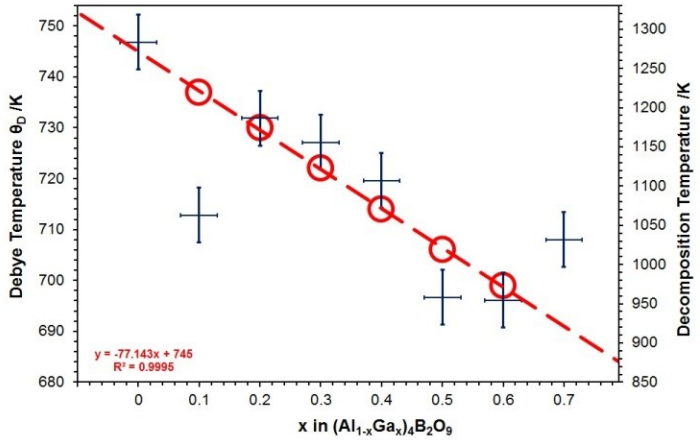

Figure 4.6. Calculated Debye temperature versus chemical composition of the $[(Al_{1-x}Ga_x)_4B_2O_9$ - A] series with A_2B structure type. The estimated standard deviations are within the symbol. Additionally the ranges of the respective decomposition temperatures are given.

4.5 Conclusion

The aim of this work was to synthesize and characterize mullite-type $(Al_{1-x}Ga_x)_4B_2O_9$ compounds. Despite the fact that a complete solid solution between two end members was not possible, we were able to successfully incorporate Ga into the A_2B structure with a limit of about 70 mol% Ga, resulting in an increase of metric parameters as well as the mean M-O distances. In mullite, the incorporation of Ga, a maximum of about 6 mol% Ga_2O_3 is determined [68]. Based on the incorporation-induced expansions of Ga-doped mullite, a preferred occupation of Ga in the octahedral positions is suggested [68]. In contrast, we observed a strong extension of this incorporation limit and a preferred occupancy of gallium in the M3 and M5 position of the A_2B structure. The preferred occupation of Ga in the non-octahedral positions in the A_2B structure might be a reason for the increase of the incorporation limit. Those of Al in the G_2B structure are approximately 70 mol% as well, though resulting in a loss of crystallinity, avoiding successful structure refinements. Nevertheless, a decrease of all the lattice parameters clearly indicates the incorporation of the smaller Al atoms in the G_2B structure.

The incorporation experiments do not show any significant change in the thermal behavior of Ga-doped aluminates and Al-doped gallates. The thermal expansion of all samples is quiet low parallel to the crystallographic **c**-direction, whereas, in comparison to mullite, especially those parallel to the **a**-direction is quiet high. The expansion anisotropy only slightly differs for pure and cation-doped samples, showing a slight increase accumulating with an increase of the gallium content in both series. However, the expansion anisotropy is quiet high making these aluminates and gallates less favorable for temperature dependent applications, as compared to mullite.

Acknowledgements

We gratefully thank L. Robben (Chemistry, University Bremen) for the evaluation of the decomposition temperatures using the autocorrelation analysis and the Deutsche Forschungsgemeinschaft (DFG) for the financial support of the projects **GE1981/3-1 and 3-2, GE1981/5-1 and FI442/19-1.**

5 Formation, stability and crystal structure of mullite-type $Al_{6-x}B_xO_9$

K. Hoffmann[a,b*], T. J. N. Hooper[c], M. M. Murshed[b,d], O. Dolotko[e]1, Z. Révay[e], A. Senyshyn[e], H. Schneider[a], J. V. Hanna[c], Th. M. Gesing[b, d], R. X. Fischer[a, d]

[a]Kristallographie, FB05, Klagenfurter Straße / GEO, Universität Bremen, D-28359 Bremen, Germany
[b]Institut für Anorganische Chemie und Kristallographie, FB02, Leobener Straße / NW2, Universität Bremen, D-28359 Bremen, Germany
[c]Department of Physics, University of Warwick, Coventry, CV4 7AL, UK
[d]MAPEX Center for Materials and Processes, Universität Bremen, Bibliothekstraße 1, D-28359 Bremen, Germany
[e]Heinz Maier-Leibnitz Zentrum (MLZ), Technische Universität München, Lichtenbergstr. 1, D-85748 Garching, Germany

[1]239 Spedding, Ames Laboratory, Iowa State University, Ames, IA 50011-3020,USA

Published in: Journal of Solid State Chemistry, 2016; 243: 124-135
DOI: 10.1016/j.jssc.2016.08.018

Submitted: 04.05.2016; accepted: 15.08.2016; online: 16.08.2016

*Corresponding author; email address: Kristin.Hoffmann@uni-bremen.de; phone: +49 (0)421 218 65172; fax: +49 (0)421 218 65189

Abstract

Mullite-type $Al_{6-x}B_xO_9$ compounds were studied by means of powder diffraction and spectroscopic methods. The backbones of this structure are chains of edge-connected AlO_6 octahedra crosslinked by AlO- and BO-polyhedra. Rietveld refinements show that the *a* and *b* lattice parameters can be well resolved, thus representing an orthorhombic metric. A continuous decrease of the lattice parameters most pronounced in **c**-direction indicates a solid solution for $Al_{6-x}B_xO_9$ with $1.09 \leq x \leq 2$. A preference of boron in 3-fold coordination is confirmed by ^{11}B MAS NMR spectroscopy and Fourier calculations based on neutron diffraction data collected at 4 K. Distance Least Squares modeling was performed to simulate a local geometry avoiding long B-O distances linking two octahedral chains by planar BO_3 groups yielding split positions for the oxygen atoms and a strong distortion in the octahedral chains. The lattice thermal expansion was calculated using the Grüneisen first-order equation of state Debye-Einstein-Anharmonicity model.

Keywords: Aluminum borate, chemical synthesis; mullite-type structure; X-ray diffraction, NMR spectroscopy, thermal expansion.

5.1 Introduction

Many of the described ternary aluminum borates belong to the family of mullite-type materials [1, 2]. Exceptions are, e.g., zeolite PKU-5, $Al_4B_6O_{15}$ reported by Ju et al. [69] to be synthesized under hydrothermal conditions at 623 K, and the high-pressure phase $AlBO_3$ described by Vegas et al. [70] to be isotypic to $CaCO_3$. Mullite-type aluminum borates are characterized by chains of edge-sharing AlO_6 octahedra. Depending on the individual phases these AlO_4 chains are linked by different arrangements of AlO_4- AlO_5-, BO_3- and eventually BO_4-polyhedra. However, little is known about the exact conditions of formation, stability ranges and details of the crystal structures. According to the phase diagram given by Gielisse and Foster [43] two thermodynamically stable phases $Al_{18}B_4O_{33}$ (A_9B_2) and $Al_4B_2O_9$ (A_2B) with mullite-type structures (Fig.5.1) are described to exist in the binary system Al_2O_3-B_2O_3. The exact chemical composition of A_9B_2 is an ongoing discussion (see, e.g., Fisch et al. [48]). Based on an ordered distribution of Al and B, $Al_{20}B_4O_{36}$ (A_5B) is the idealized model, representing $Al_{18}B_4O_{33}$ (A_9B_2) composition [26] if about 2% of the Al is replaced by B ($Al_{20}B_4O_{36}$ vs. $Al_{19.6}B_{4.4}O_{36}$). In this work we use the designation A_9B_2 as commonly employed in the material science literature. Accordingly, the exact stoichiometric composition of $Al_{18}B_4O_{33}$ was used for the synthesis, slightly shifted to a lower Al content compared to $Al_{20}B_4O_{36}$ and $Al_{6-x}B_xO_9$ with $x = 1$.

Mazza et al. [24] synthesized a series of probably metastable compounds with chemical composition according to $Al_{6-x}B_xO_9$ ($1 \leq x \leq 3$) and disordered crystal structures different from A_9B_2 and A_2B. Further heat treatment yields the stable equilibrium phases. The compounds with $x = 1$ (Al_5BO_9) and $x = 2$ ($Al_4B_2O_9$) are described by Mazza et al. [24] to crystallize in the orthorhombic space group *Pbam* with lattice parameters $a = b$, representing a pseudo-tetragonal metric, and an average structure close to mullite (Fig.5.1). In order to distinguish between different phases with identical chemical compositions we refer to the metastable compounds as $Al_{6-x}B_xO_9$ with $x = 1$ and $x = 2$, respectively, in contrast to the stable compounds A_9B_2 and A_2B.

According to Mazza et al. [24], the Al-rich compound $Al_{6-x}B_xO_9$ ($x = 1$) consists of octahedrally and tetrahedrally coordinated aluminum and trigonal borate groups, whereas in the boron-rich compound $Al_{6-x}B_xO_9$ ($x = 2$) one B atom substitutes for one Al atom in the tetrahedral site, leading to the occurrence of an additional BO_4 tetrahedron and a slight distortion of the octahedral chains. In this fourfold coordination an additional longer bond to a non-octahedral oxygen atom occurs. As boron cannot be detected accurately from X-ray powder diffraction data due to its low scattering factor, the location of threefold coordinated boron was assumed by Mazza et al. [24] analogously to the corresponding configuration in A_9B_2. However, the range of B-O distances is 140 pm – 160 pm for threefold and 150 pm – 248 pm for fourfold coordination in both crystal structures being too large for a meaningful crystal-structure model. In contrast, the Al-O distances in the AlO_4 tetrahedron for $Al_{6-x}B_xO_9$ ($x = 1$) are too short.

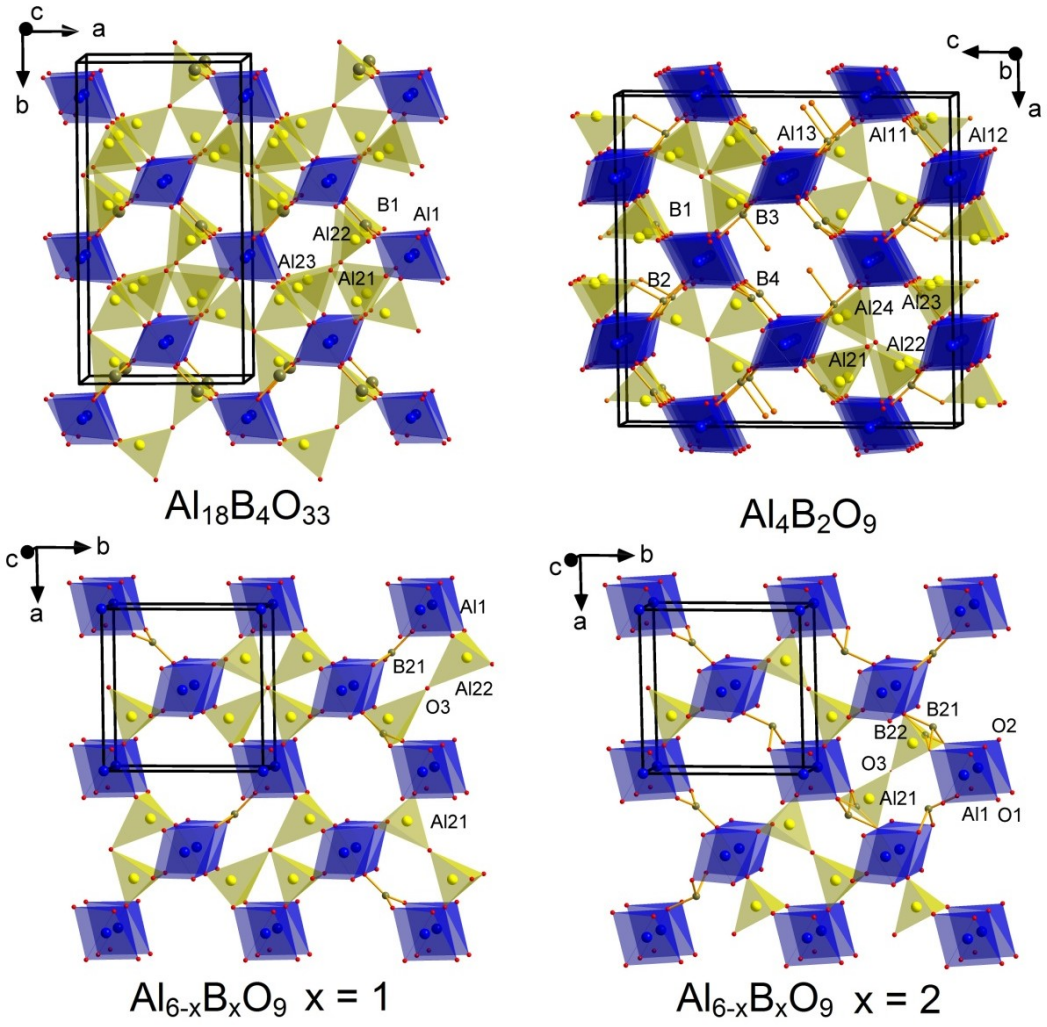

Figure 5.1. Crystal structures of mullite-type aluminum borates. Blue polyhedra: AlO_6-octahedra, yellow spheres: Al (in AlO_4- or AlO_5-polyhedra), green spheres: B (in BO_3- or BO_4-polyhedra)

The focus in this paper is (i) the investigation of the phase formation of the mullite-type phases in a compositional range between the two technically relevant compounds A_9B_2 and A_2B and (ii) the crystal-chemical characterization of $Al_{6-x}B_xO_9$ phases together with the changes of these crystal structures as a function of the boron content in the precursor phases.

5.2 Materials and methods

5.2.1 Synthesis

Series of powder samples were synthesized using the nitrate decomposition method described in [24, 60, 61] as a function of the boron content in the precursor phase. $Al(NO_3)_3 \cdot 9H_2O$ and $B(OH)_3$ were mixed in the corresponding ratios and dissolved in 10 wt% glycerol (1,2,3-propanetriol). At room temperature the reaction of glycerol and boric acid leads to the formation of ester complexes, thus

preventing a volatilization of considerable amounts of the boric acid above 373 K [24, 71]. Using covered platinum crucibles, the final heating procedure differs concerning time and temperature (Table 5.1, series A: 1223 K, 72h; series B: 1173 K, 6h). After the heat treatment all samples were quenched to room temperature. By washing the powder with hot deionized H_2O possible impurities of boron oxide were removed. For neutron diffraction studies one sample was prepared using $^{11}B(OH)_3$ with 99% ^{11}B. The experimental conditions for all samples are given in Table 5.1. Chemical compositions given in this work always refer to the initial synthesis composition given in wt% Al_2O_3 and B_2O_3.

Table 5.1. Analytical methods used for sample characterization.

Exp.	Al_2O_3 /wt%	B_2O_3 /wt%	Temp. /K	Time /h	RT-XRD	HT-XRD	FTIR	MAS NMR	MQ MAS NMR	TA	PGAA / NPD	LT-NPD
						Series A						
A1	95	5	1223	72	X		X					
A2	90	10	1223	72	X		X					
A3	86.83	13.17	1223	72	X		X					
A4	83	17	1223	72	X		X					
A5	80	20	1223	72	X		X					
A6	77.5	22.5	1223	72	X		X					
A7	74.55	25.45	1223	72	X		X					
A8	70	30	1223	72	X		X					
A9	65	35	1223	72	X		X					
A10	60	40	1223	72	X		X					
A11	50	50	1223	72	X		X					
A12	35	65	1223	72	X		X					
A13	10	90	1223	72	X		X					
						Series B						
B14	86.83	13.17	1173	6	X			X	X	PM		
B15	83	17	1173	6	X	LM	X	X		X,PM		
B16	80	20	1173	6	X	LM	X	X	X	X,PM		
B17	77.5	22.5	1173	6	X	LM,PM	X	X		X,PM		
B18	74.55	25.45	1173	6	X			X	X	PM		
B19	70	30	1173	6		LM,PM				PM		
B20	80	(^{11}B)20	1173	6	X	X					X	X

RT-XRD = room-temperature X-ray diffraction; HT-XRD = high-temperature X-ray diffraction; LT-NPD = low-temperature neutron powder diffraction; TA = thermal analysis; MQ MAS NMR = multiple-quantum magic angle spinning NMR; PGAA = prompt gamma activation analysis; PM = analysis of precursor material, LM = long-term experiment of precursor material.

5.2.2 Diffraction

X-ray powder diffraction

Room-temperature powder X-ray diffraction data were collected on a Philips X'Pert diffractometer, using Ni-filtered CuK$\alpha_{1,2}$ radiation in Bragg-Brentano geometry and a X'Celerator detector system. Data were collected from 5 - 90° 2θ, with a step size of 0.0167° 2θ/step and a measuring time of 80 s per step (series A) and from 3 - 130° 2θ with 50 s per step (series B), using tube settings of 45 kV and 40 mA.

Selected samples were studied by means of high-temperature X-ray diffraction on a Philips X'Pert diffractometer. The instrument is equipped with a high-temperature chamber HTK 1200N (Anton Paar GmbH, Graz, Austria), using the configuration described above. The samples were pre-heated (923 K) in order to reduce the release of organic compounds and nitrates. Dispersed in alcohol, they were transferred into a sample holder of corundum. Data were collected from 3 - 96° 2θ, with a step size of 0.0167° 2θ/step and a measuring time of 40 s per step. The temperature was first increased to 873 K, followed by 973 K and then stepwise in 50 K steps up to 1423 K, repeating the measurement at 1173 K and 1223 K once. Long-term experiments were performed at 1223 K for 3 days with repeating measurements every 30 minutes. For all samples the first and last measurement was carried out at room temperature. Additionally the thermal stability and expansion was studied for one sample, labeled with ^{11}B, heated stepwise in 20 K-steps from 300 K up to 1340 K. Data were collected from 3 - 100° 2θ, with a step size of 0.0167° 2θ/step and a measuring time of 50 s per step.

Neutron powder diffraction

Neutron powder diffraction (NPD) data were collected at room temperature in high-resolution mode on the powder diffractometer SPODI@FRM-II. A collimated beam of neutrons (λ = 155.01(1) pm) was generated by a Ge (551) monochromator, with a take-off angle of 155°. Data were collected in the range from 0.3 - 152° 2θ, with a step size of 0.05° 2θ/step. More details are available in [72]. Low-temperature NPD data were collected on SPODI@FRM-II [72] using a closed cycle cryostat between 4 K and 320 K in 20 K steps. Data were collected in the range from 1 - 152° 2θ, with a step size of 0.1° 2θ/step, using a collimated beam of neutrons (λ = 154.81(1) pm).

Rietveld analysis

Rietveld refinements of all crystalline samples were carried out using the "DiffracPlus Topas 4.2" (Bruker AXS GmbH, Karlsruhe, Germany) or BRASS [50] software. For Rietveld refinements combining the data of X-ray and neutron diffraction experiments (sample B20), the crystal structure of $Al_{6-x}B_xO_9$ structure [24] with $x = 2$ was used as initial model. Mixed occupancy of Al and B was assumed on the B1 position. The neutron wavelength was optimized to λ = 155.01(1) pm using the fixed X-ray wavelength while simultaneously refining the lattice parameters constrained for both data

sets. For the structure refinements the neutron wavelength was then fixed and all parameters were optimized using both X-ray and neutron data.

5.2.3 Distance Least Squares modeling

Distance Least Squares (DLS) [58] modeling was performed to refine the local environment of boron in the crystal structure with geometric restraints for the interatomic distances. Calculations were performed to determine probable split positions for oxygen representing O in undistorted AlO_6 octahedra and O atoms shifted towards neighboring 3-fold coordinated boron. These calculations were carried out using the refined lattice parameters and atomic positions from a combined X-ray and neutron diffraction data refinements. The original structure model of $Al_{6-x}B_xO_9$, $x = 2$ was used [24]. The ideal Al-O distance in AlO_6 is 188.5 pm estimated from the sum of the ionic radii [10], the resulting O-O distance in a regular octahedron is 267 pm. The ideal B-O distance in a planar BO_3 triangle is 137 pm [10, 47], as also determined in mullite-type structures by neutron diffraction experiments [73], resulting in an O-O distance of 237 pm. The calculation is restricted to two octahedral chains linked by BO_3. Symmetrically equivalent atoms were decoupled for an independent refinement by using the triclinic space-group *P*1 and a doubled *c* lattice parameter. Lattice parameters and atomic coordinates of B and octahedrally coordinated Al were fixed as well as the *x* and *y* coordinates of O1 and the *z* coordinate of O2 because theses coordinates correspond to the respective boron coordination. Prescribed atomic distances and weights are listed in Table 5.2.

Table 5.2. Prescribed atomic distances and weights used for DLS-refinements.

Polyhedral bond distance		*Distance /pm	Weighting factors
AlO_6	Al-O	188.5	0.5
	O-O	267	0.2
BO_3	B-O	137	2.5
	O-O	237	0.2

*Inter-atomic distance calculated from the sum of the ionic radii [10]

5.2.4 Spectroscopy

Infrared Spectroscopy

Fourier-transform infrared (FTIR) spectra were collected in the mid-infrared (MIR) range on a Bruker Vertex 80v FTIR spectrometer. Using the standard KBr method, 1 mg of the sample was homogenized with 200 mg KBr, pressed into a pellet and measured relative to a KBr reference pellet. Data were

obtained in a spectral range of 370 cm^{-1} – 4000 cm^{-1} with a spectral resolution of 2 cm^{-1} and 32 scans per spectrum.

MAS NMR Spectroscopy

The ^{11}B MAS NMR measurements were undertaken at 14.1 T using a Varian-600 spectrometer operating at the ^{11}B Larmor frequency of 192.50 MHz. All ^{11}B MAS NMR data were acquired using a Varian 4mm HX MAS probe which enabled a MAS frequency of 12 kHz throughout. Each reported measurement employed a 'selective' $\pi/2$ pulse time of 5 μs, inferred from a 'non-selective' $\pi/2$ pulse time of 10 μs measured on $NaBH_4$(s), with a recycle delay of 20 s. The quantitative nature of these measurements was tested on selected samples against experiments utilizing smaller flip angles (with the same radio frequency power levels) that satisfied the uniform excitation condition for quadrupolar nuclei [74, 75] where $(I + ½)\ \omega_{rf} t_p \leq \pi/6$. In this case, a 'selective' (solid) $\pi/9$ pulse time of 1.1 μs with a recycle delay of 20 s was used to ensure that the relative ratio between the BO_3 and BO_4 species remained unchanged, although a much longer acquisition time of >24 h for each measurement was necessary to achieve sufficient signal/noise for this purpose. All ^{11}B chemical shifts were referenced to $BF_3.Et_2O$ (δ_{iso} 0.0 ppm) via a secondary solid $NaBH_4$ reference (δ_{iso} –42.06 ppm), and each ^{11}B MAS NMR spectrum was simulated using the DMFit program to elucidate the relative proportions of the BO_3 and BO_4 species [51].

The ^{27}Al MAS NMR measurements were undertaken at 14.1 T and 9.40 T using a Bruker Avance II+-600 spectrometer operating at the ^{27}Al Larmor frequency of 156.34 MHz and a Bruker Avance 400 spectrometer operating at the ^{27}Al Larmor frequency of 104.23 MHz, respectively. All ^{27}Al MAS NMR data were acquired using a Bruker 3.2mm HX MAS probe which enabled a MAS frequency of 20 kHz throughout. The 14.1 T ^{27}Al MAS data were acquired using a single pulse experiment which employed a 'selective' 0.80 μs excitation pulse corresponding to a $\pi/6$ flip angle, inferred from the 'non-selective' $\pi/2$ pulse time of 7.5 μs measured on the AlO_6 resonance of YAG(s), and a recycle delay of 2 s. The corresponding 9.40 T ^{27}Al MAS data were acquired using the same pulse time calibration on the AlO_6 $YAG_{(s)}$ resonance, with the single pulse experiments employing a slightly longer 1 μs 'selective' excitation pulse and a recycle delay of 10 s. These pulse conditions at both B_0 fields ensured a 1:1 intensity ratio in the AlO_4 and AlO_6 species of the YAG spectrum. The 14.1 T 2D ^{27}Al MQMAS NMR data were acquired using a Z-filtered 3QMAS pulse sequence with a 3.5 μs excitation pulse, a 1.5 μs conversion pulse and a 17.0 μs selective final pulse. These MQMAS data were processed using TOPSPIN and then sheared using the TOPSPIN AU program *xfshear*. All ^{27}Al chemical shifts were referenced to 1 M $Al(NO_3)_3$(aq) (δ_{iso} 0.0 ppm) via a secondary solid YAG reference (δ = 0.7 ppm for the AlO_6 site).

5.2.5 Thermal analyses

Powder samples were studied by differential thermal analysis (DTA) on a Netzsch 449 F3 Jupiter STA (Netsch GmbH, Selb, Germany), to investigate the formation conditions of the mullite-like phases as function of the boron content in the precursor phase. Homogenized powder of the dried foam, pre-heated at 673 K in order to reduce the release of organic compounds and nitrates, was heated from ambient conditions to 1473 K in covered corundum crucibles (heating rate: 5 K/min; cooling rate: 20 K/min). All experiments were performed under dry synthetic air atmosphere with a controlled gas flow (50 mL/min). Proteus Netzsch software (Netsch GmbH, Selb, Germany) was used for data evaluation.

5.2.6 Prompt gamma activation analysis

Since boron is known to be volatile prompt gamma activation analysis (PGAA) was performed to determine the Al/B ratio of sample B20 with an initial composition of 80 wt% Al_2O_3 and 20 wt% B_2O_3 (99% ^{11}B), also used for the neutron powder diffraction experiments. The measurement was performed using a 15 mm lead attenuator. Details of the PGAA system are described in [76, 77]. The Al_2O_3/B_2O_3 ratio was calculated from the given molar composition of 30 mol% (+/- 0.9%) boron and 70 mol% (+/- 0.4%) aluminum, representing a ratio of 22.6% (+/- 1%) B_2O_3 and 77.4% (+/- 0.3%) Al_2O_3, thus resulting in a chemical composition of $Al_{4.20(2)}B_{1.80(5)}O_9$.

5.3 Results and discussion

5.3.1 Phase formation

The phase formation of compounds in the sample series A is shown in Figure 5.2, where the lattice parameters are plotted versus the weight fractions of B_2O_3 in the initial composition. Between the dot-dashed lines the formation of $Al_{6-x}B_xO_9$ is observed. Towards higher and lower amounts of B_2O_3 monoclinic A_2B and orthorhombic A_9B_2 are formed, respectively. In the low B_2O_3 region additional diffraction peaks occur which can be assigned to at least three different alumina phases (α, γ, θ). Diffraction peaks found in sample A1 around 34.5° 2θ could not be assigned to any phase. H_3BO_3 occurs in the high B_2O_3 region but is removed by washing yielding pure A_2B. Nevertheless, in the compositional range between 5 - 30 wt% B_2O_3 the refinement of A_2B or A_9B_2 yield a better fit by using one of the structure models published by Mazza et al. [24] as additional phase. Diffraction patterns of series A are shown in Figure 5.3. Extension of the heating period up to 14 days leads to a

shift in the phase formation towards more aluminum-rich phases, probably caused by a loss of the highly volatile boron oxide during the synthesis.

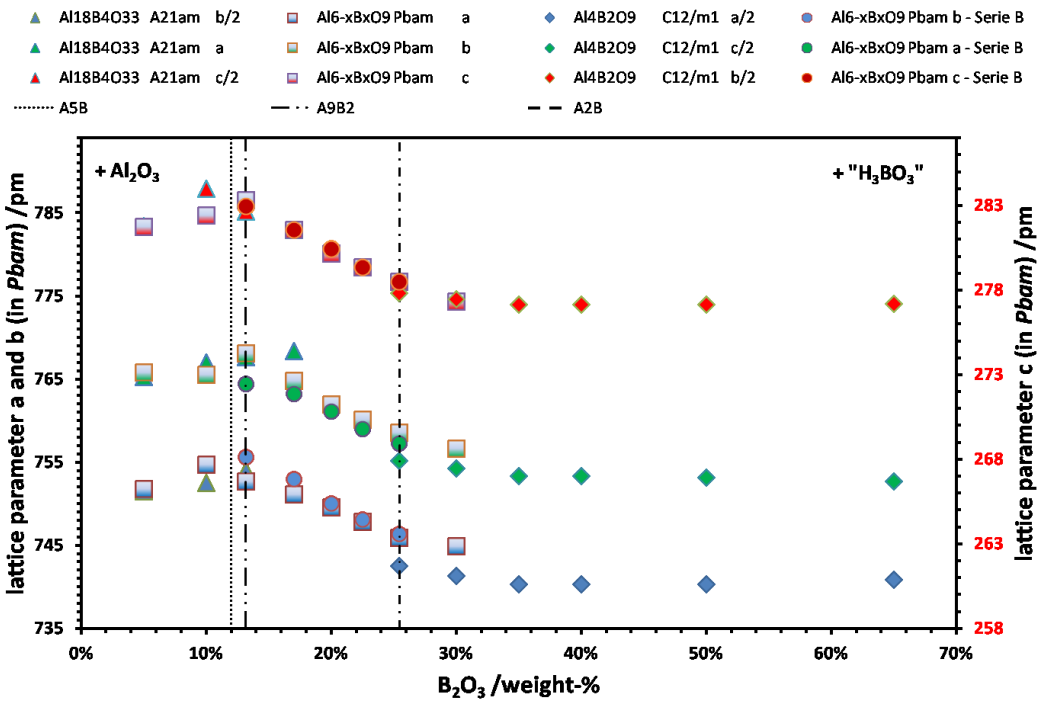

Figure 5.2. Lattice parameter development of the mullite-type Al-borates plotted versus increasing initial B_2O_3-content. For comparison of the lattice parameters of $Al_{6-x}B_xO_9$ with those of the thermodynamically more stable polymorphs, the lattice parameters were halved in all three directions for A_2B and in **b**- and **c**-direction for A_9B_2.

The X-ray diffraction pattern obtained here for samples with an initial content of 80 wt% (sample A5) and 77.5 wt% (sample A6) B_2O_3 are similar to the pattern published by Mazza et al. [24], however with broad humps around 20° 2θ or 18° 2θ indicating poorly crystalline A_9B_2 or A_2B phases, respectively. As we found the $Al_{6-x}B_xO_9$-compounds to appear restricted in the range of $B_2O_3 \leq 30$ wt%, while Al_2O_3 is observed to occur as additional phase in case of $x < 1$, further investigations are focused to compositions of $1 \leq x \leq 2$. At 1173 K and 6h the broad humps around 20° 2θ or 18° 2θ could be reduced and phase purity was optimized (series B). Although all samples were washed to remove amorphous B_2O_3 [25], an amorphous content of about 15 - 27 wt% was determined using SiO_2 as an internal standard for three selected samples (B15 - B17). The lowest amorphous content was observed for sample B16 with an initial composition of 80 wt% Al_2O_3 and 20 wt% B_2O_3. The lattice parameters of all samples were refined using a Pawley fit. Due to a small crystallite size of 25 – 44 nm the diffraction peaks are distinctly broadened. The *a* and *b* lattice parameters can be well resolved in contrast to the pseudo-tetragonal metric described by Mazza et al. [24], as shown in Figure 5.2. A continuous change of all three lattice parameters, systematically decreasing by 1.58% in **c**-, 1.22% in

b-, and 0.93% in **a**-direction indicates a complete $Al_{6-x}B_xO_9$ solid solution between $x = 1.09$ and $x = 2$. A similar trend of decreasing lattice parameters in **b**- and **c**-direction with increasing boron content was also observed for B-doped mullite [29, 30].

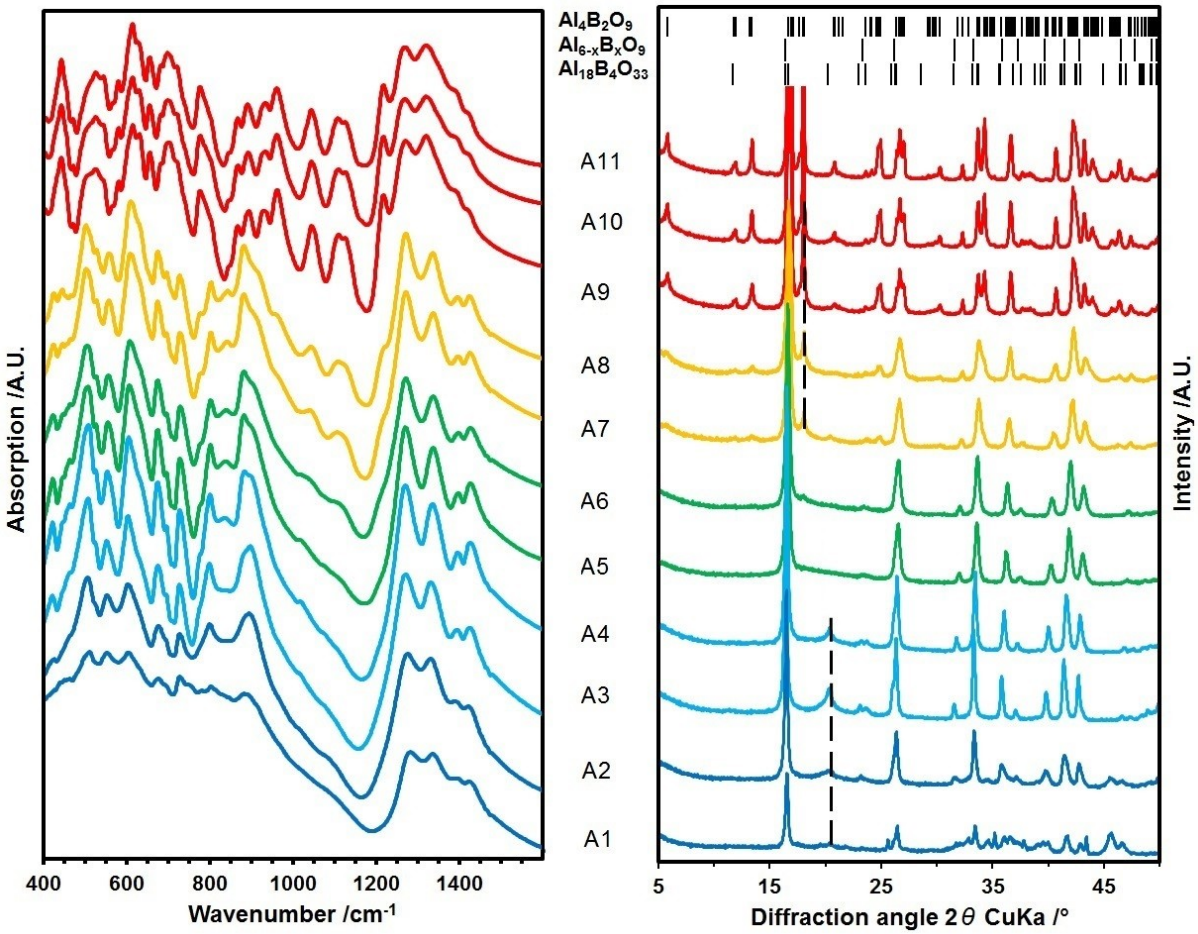

Figure 5.3. X-ray diffraction patterns (right) of the samples A1 to A11 (Table 5.1) and the corresponding FTIR spectra (left) of the samples with different boron content. Dotted lines around 18° 2θ and 20° 2θ correspond to the characteristic diffraction peaks of A_2B and A_9B_2. The possible reflection positions of these two phases and $Al_{6-x}B_xO_9$ are given in the upper part.

The conditions of phase formation were investigated by high-temperature XRD and DTA methods in a compositional range of 13.17 – 30 wt% boron oxide. DSC measurements of the precursor phases show first an exothermic signal in the range of 1163 K - 1103 K linearly decreasing with an increase of the initial boron content as shown in Figure 5.4. This agrees well with the results of Mazza et al. [24], observing crystallization temperatures decreasing between 1190 K - 1128 K for $1 \leq x \leq 3$ ($Al_{6-x}B_xO_9$), and Douy [71] observing a regular decrease more rapidly. A decreasing crystallization temperature with increasing boron amount is also reported for boron containing mullite [29, 78]. Zhang et al. [78] explained the reduction of the formation temperature for boron-doped single phase mullite precursors

by enhanced atomic diffusion, caused by a reduction of glass phase viscosity. A second DTA signal is observed above about 1273 K. The first signal represents the crystallizing process in the phase field A_2B – A_9B_2, whereas the second signal belongs to a phase transformation, most probably of $Al_{6-x}B_xO_9$ into A_9B_2. As the sample with an initial amount of 13.17 wt% boron oxide represents the exact initial composition of A_9B_2, this sample does not show a signal above 1273 K. Further signals in the temperature range below 873 K represent dehydration processes. B_2O_3 in the precursor phases may hydrolyze to $B(OH)_3$ in atmospheric conditions, whereas boric acid dehydrates by heating the sample above 673 K.

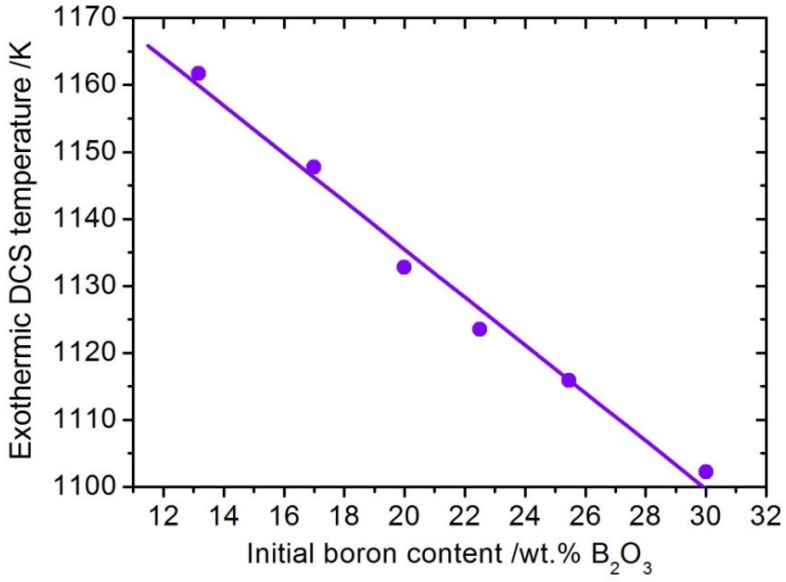

Figure 5.4. Linear decrease of the phase formation temperature (onset temperature, determined from the exothermic DSC signal) dependent on the initial boron content.

High-temperature XRD measurements were performed up to 1373 K using two samples exemplarily with $x < 2$ (B17) and $x > 2$ (B19), respectively (see Tab. 5.1). At 873 K broad diffraction peaks could be observed for both samples, while $Al_{6-x}B_xO_9$ is well crystallized at about 1123 K with orthorhombic lattice parameters in space group *Pbam*. This agrees well with the results from DTA experiments. For the sample with an initial composition in the range of $x > 2$, poorly crystalline A_2B could be observed in the HT-experiment as a second phase starting from 1173 K, transforming into A_9B_2 with increasing temperature. With decreasing initial boron content ($x < 2$) no formation of A_2B is observed before transforming into A_9B_2. Pure, well crystalline A_9B_2 is observed at temperatures higher than 1423 K.

Long-term high-temperature XRD experiments were performed at 1223 K for 72h for 4 samples (B15-17 and B19). After heating the samples B15 - B17 to 1223 K, the crystallized compounds can be described in space group *Pbam* gradually transforming into A_9B_2, or into A_2B and A_9B_2 for the

samples with an initial composition near $x = 2$ (B17). Experiments performed on the sample with $x > 2$ (B19) directly show characteristic reflections of A_2B in the X-ray pattern representing both phases, A_2B and $Al_{6-x}B_xO_9$, to be present. Continuing heat treatment at 1223 K leads to the crystallization of A_9B_2 again indicating a loss of the boron component upon heating.

5.3.2 Structural changes - IR- and NMR-Spectroscopy

The FTIR spectra of the samples (series A) are shown in Figure 5.3. The IR-active asymmetric stretching vibrations for B-O are expected to occur at 950 cm^{-1} – 1200 cm^{-1} for BO_4 and at 1200 cm^{-1} - 1450 cm^{-1} for BO_3 [48]. In the low B_2O_3 region where $Al_{6-x}B_xO_9$ is accompanied by poorly crystalline A_9B_2, boron is observed exclusively in 3-fold coordination. With increasing initial boron content spectral modes of BO_4 are observed, starting with a broad hump for an initial composition of 17 wt% B_2O_3, obviously for samples with A_2B observed as an additional phase. The spectra show broad peaks caused by the amorphous content and small crystallite size. Therefore not all peaks could be resolved.

Solid state ^{11}B and ^{27}Al MAS NMR data were acquired for all samples comprising series B (Fig. 5.5). The ^{11}B MAS NMR spectra clearly show that the B geometry is represented by both 3-fold (BO_3) and 4-fold (BO_4) coordination environments. The trigonal planar BO_3 positions exhibited a second order broadened quadrupolar resonance that were simulated using values of C_Q ~2.6 MHz and δ_{iso} ~16.7 ppm (see Tab. 5.3), which are highly characteristic of that B environment [30]. In contrast, the ^{11}B resonances representing the tetrahedral BO_4 positions were simulated with single (or multiple) Gaussian line-shapes positioned further up-field at δ_{iso} ~0.0 ppm, with estimates of the values of C_Q <1.0 MHz indicating a much smaller quadrupolar interaction in comparison to the BO_3 species by virtue of the comparatively higher point symmetry of the BO_4 unit. The parameters describing each fit are shown in Table 5.3 and these detail an increase in the site occupancy of 4-coordinated BO_4 with increasing initial B content. This confirms the assumption of a possible solid state solution being established between tetrahedral AlO_4 and BO_4; moreover, multiple BO_4 resonances were observed for most samples in this suite suggesting that some genuine disorder in the tetrahedral units within these structures may be intrinsic to these systems. Conversely, the presence of poorly crystalline A_2B and/or A_9B_2 impurities may also exist in these systems. The latter occurrence would only be manifest as a minor impurity as evidenced by the smaller relative BO_4 intensities shown in Table 5.3 and the monotonic trends established in the B speciation.

Table 5.3. ^{11}B solid state NMR parameters from simulated fits for $Al_{6-x}B_xO_9$ samples (series B).

Exp.	Initial x $Al_{6-x}B_xO_9$	Species	fit	δ_{iso} /ppm (± 0.2)	Δ(width) /KHz (± 0.05)	C_Q /MHz (± 0.1)	η_Q (± 0.01)	integr. Int. /% (± 1)	Species Int. /% (± 1)
B14	x = 1.09	BO_3	½ QMAS	16.7	-	2.6	0.16	99	99
		BO_4	Gauss	0.3	0.29	-	-	1	1
B15	x = 1.38	BO_3	½ QMAS	16.8	-	2.6	0.16	96	96
		BO_4	Gauss	-0.1	0.22	-	-	2	4
			Gauss	1.1	0.29	-	-	2	
B16	x = 1.61	BO_3	½ QMAS	16.8	-	2.6	0.15	92	92
		BO_4	Gauss	-0.7	0.34	-	-	8	8
B17	x = 1.79	BO_3	½ QMAS	16.8	-	2.6	0.15	85	85
		BO_4	Gauss	-0.7	0.14	-	-	3	15
			Gauss	1.6	0.69	-	-	6	
			Gauss	-0.2	0.24	-	-	6	
B18	x = 2	BO_3	½ QMAS	16.7	-	2.6	0.15	80	80
		BO_4	Gauss	-1.1	0.11	-	-	4	20
			Gauss	0.8	0.53	-	-	11	
			Gauss	-0.6	0.23	-	-	5	

δ_{iso} = chemical shift, C_Q = quadrupole coupling constants, η_Q = asymmetry parameter

Sample B16 ($Al_{6-x}B_xO_9$) with an initial composition of 80 wt% Al_2O_3 and 20 wt% B_2O_3 was observed to have a site occupancy ratio of 92:8 for BO_3:BO_4. This represents a much lower percentage of BO_4 than expected. Corresponding to the PGAA data of sample B20 with the same initial composition as sample B16, about 44% BO_4 would be expected on the B1 position, if the B2 (BO_3) position is fully occupied, based on the structure model published by Mazza et al. [24] for $Al_{6-x}B_xO_9$ with x = 2. For a sample with the exact initial composition corresponding to x = 2, 50% BO_4 would be expected, but a maximum of 20% is observed for sample B18 (Tab. 5.3). This represents a clear preference of boron in 3-fold coordination and therefore the ^{11}B MAS NMR data suggests that the proposed structural model may need to be reevaluated, and this is corroborated by the solid state NMR investigation on a similar series of aluminum borates ($Al_{6-x}B_xO_9$ with x = 1 - 4) performed by MacKenzie et al. [79].

The ^{27}Al MAS NMR data for the samples of series B is shown in Figure 5.5. To assist the modelling and deconvolution of the unresolved ^{27}Al MAS NMR resonances, additional ^{27}Al MQMAS measurements were acquired for selected samples (B14, B16 and B18). For each of these systems the ^{27}Al MQMAS data (see Fig. 5.6) contains resonances pertaining to Al in 3 different coordination environments, namely $Al^{(IV)}$ (or AlO_4), $Al^{(V)}$ (or AlO_5) and $Al^{(VI)}$ (or AlO_6). The presence of 5-coordinated AlO_5 is contrary to the structural models proposed by Mazza et al. [24], but this observation is not entirely surprising as the stable A_9B_2 phase has been shown to exhibit an ordered network containing one $Al^{(IV)}$ site, two $Al^{(V)}$ sites and one $Al^{(VI)}$ site [80, 81]. Additionally the stable A_2B phase has been shown to contain AlO_5 sites [25]. The presence of at least one $Al^{(V)}$ site was also detected in the ^{27}Al MAS NMR data reported by MacKenzie et al. [79]. Nevertheless, these authors

did not provide X-ray pattern for their samples synthesized at 1223 K with $1 \leq x \leq 4$. Therefore we assume that they might have a mixture of $Al_{6-x}B_xO_9$ phases with the more stable polymorph of A_2B. For well-crystallized mullite two closely overlapping peaks are observed in the AlO_4 region, one at 64 ppm assigned to the regular AlO_4 site and a second one at 46 ppm associated with tri-cluster units [82, 83]. For pure and Sr-doped mullite-type $Bi_2Al_4O_9$ a signal was found at 46.8(5) ppm also assigned to tri-clusters [84]. Therefore, the determined AlO_5 units in the range of 34 - 50 ppm should be assigned to tri-cluster units.

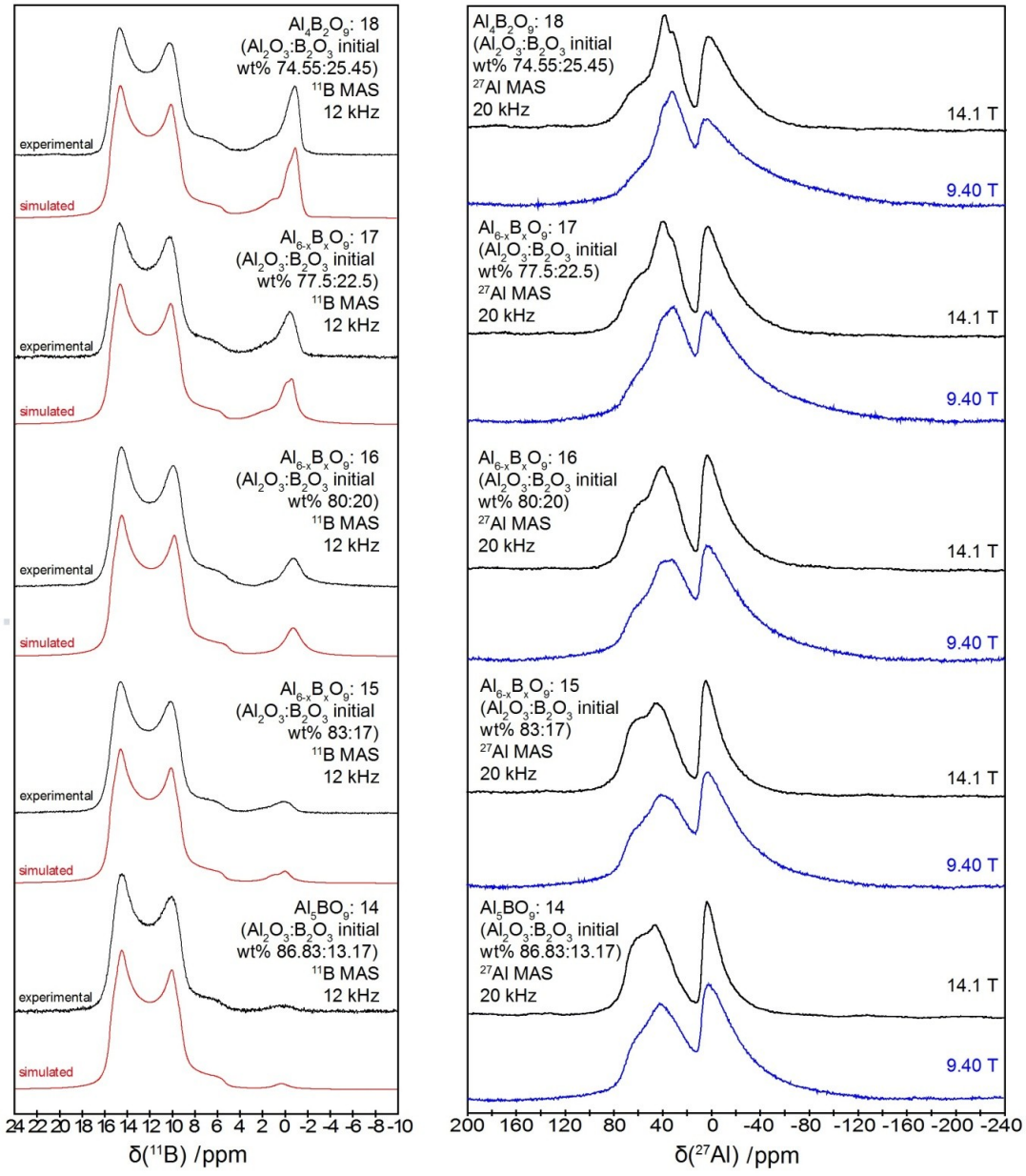

Figure 5.5. Experimental ^{11}B MAS NMR (left) data for $Al_{6-x}B_xO_9$ series (black lines) displayed with the corresponding simulations (red spectra) obtained by using the DMFit program [51], and ^{27}Al MAS NMR (right) data for $Al_{6-x}B_xO_9$ series acquired at 14.1 T and 9.40 T (black and blue lines respectively).

The highly resolved ^{27}Al MQMAS measurements, presented in Figure 5.6, permit a more accurate identification of *all* of Al speciation than achieved in previously reported work [79]. The contours present in the 2D ^{27}Al MQMAS data and the long asymmetric tails (to higher field) of all of 1D ^{27}Al MAS NMR resonances indicate that significant distributions of quadrupolar and chemical shift parameters exist, thus implying that significant short range disorder characterizes these systems even though longer range periodicity does give rise to the measured diffraction data. The QuadFit program was used to simulate the NMR spectra as it allows for sites with a distribution in their quadrupolar parameters [52]. The deconvolutions of the 1D ^{27}Al MAS NMR data at two fields (9.40 T and 14.1 T) were simulated using Gaussian distributions of the quadrupolar coupling constant (C_Q) to accurately represent the disordered quadrupolar lineshapes observed. The deconvolutions were additionally constrained by simulating the MQMAS projections of each site and therefore invoke an accurate simulation of each spectrum for the samples analyzed with this methodology.

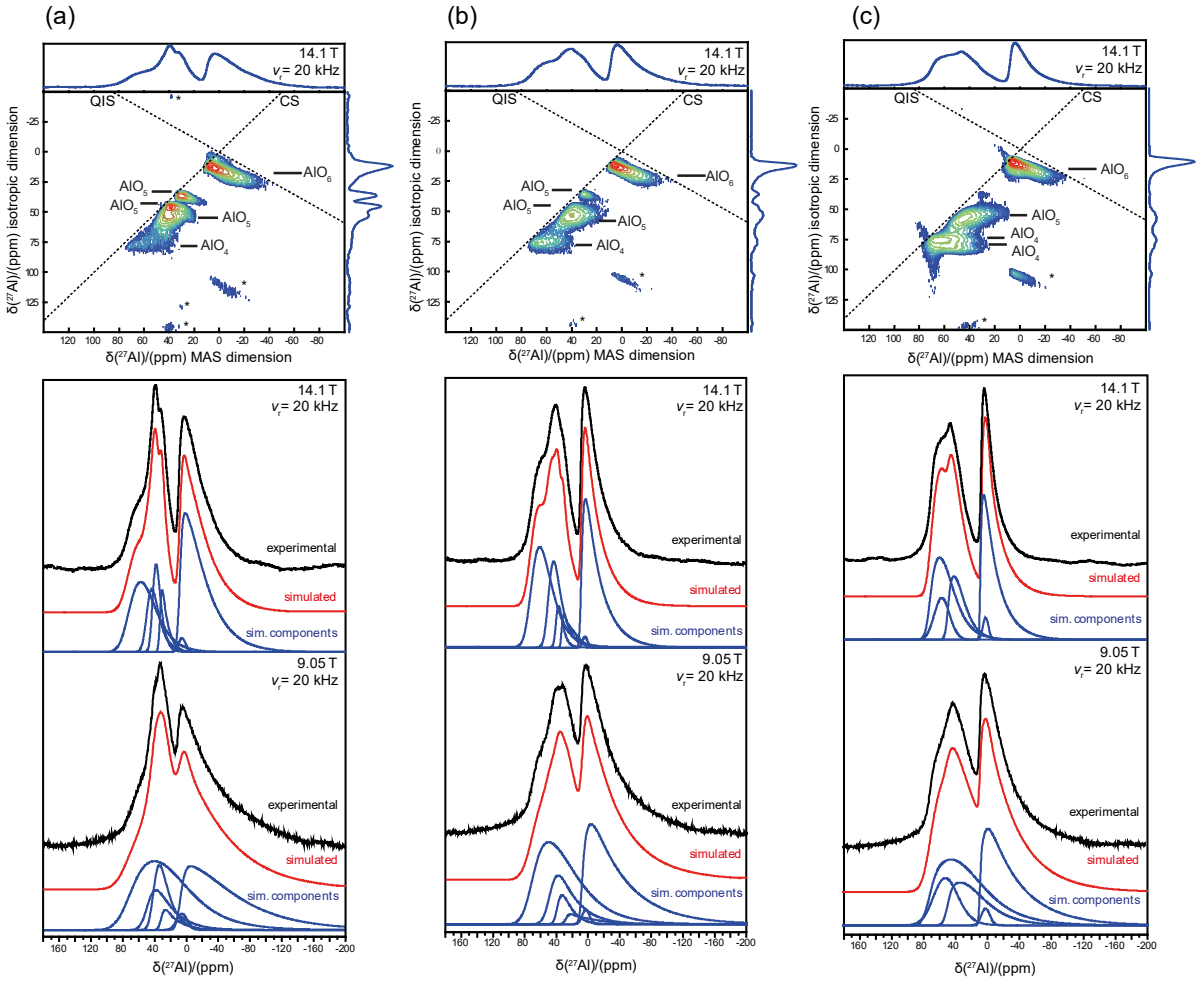

Figure 5.6. ^{27}Al MQMAS NMR data (top) and ^{27}Al MAS NMR spectra and deconvolutions at 14.1 T and 9.40 T (bottom) using the QuadFit program [52] for selected samples with an initial Al content of (a) B18, (b) B16 and (c) B14.

From Tables 5.3 and 5.4, and the ^{27}Al MAS and MQMAS NMR data of Figure 5.6, it can be observed that as the initial B content is increased the AlO_5/tri-clusters site occupancy increases, evolving from one AlO_5/tri-clusters site in sample B14 ($Al_{6-x}B_xO_9$ (x = 1.09)) to three more ordered AlO_5/tri-clusters sites in sample B18 ($Al_{6-x}B_xO_9$ (x = 2)). This behavior mirrors the concomitant increase of the relative BO_4 content from ~1% to ~ 18% within this suite of samples. The absence of particular AlO_5/tri-clusters sites in sample B14 ($Al_{6-x}B_xO_9$ (x = 1.09)) (in comparison to samples B16 and B18) is accompanied by the emergence of an additional AlO_4 site. Furthermore, the observed disorder in the more populated AlO_6 site increases with increasing B content. These trends are compatible with the assumption that increasing initial B content substitutes AlO_4 tetrahedral positions with BO_4 counterparts. An introduction of smaller BO_4 units will induce distortion to the adjacent AlO_6 octahedral chains and the increased disorder rearranges some of the AlO_4 tetrahedra to form AlO_5 moieties.

Table 5.4. ^{27}Al solid state NMR parameters obtained from the simulated fits for selected samples of series B.

Exp.	Initial x $Al_{6-x}B_xO_9$	Species	δ_{iso} /ppm (± 1)	broad /KHz (± 0.1)	C_Q pos. /MHz (± 0.1)	C_Q width /MHz (± 0.1)	η_Q (± 0.1)	integr. Int /%	Species Int. /%
B14	x = 1.09	AlO_6	2	1.3	0.0	0.0	0.0	2 ± 1	38 ± 2
		AlO_6	9	0.4	8.1	7.8	0.3	36 ± 1	
		AlO_5	50	1.1	6.8	4.7	1.0	17 ± 1	17 ± 1
		AlO_4	62	3.2	4.3	3.3	0.5	12 ± 1	45 ± 2
		AlO_4	73	1.8	8.0	5.0	1.0	33 ± 2	
B16	x = 1.61	AlO_6	4	1.1	0.0	0.0	0.0	1 ± 1	41 ± 1
		AlO_6	9	0.7	8.6	8.0	0.3	41 ± 1	
		AlO_5	37	0.3	7.6	3.4	0.1	4 ± 1	24 ± 4
		AlO_5	41	0.9	4.7	3.3	0.5	5 ± 1	
		AlO_5	49	1.8	6.0	5.6	0.5	16 ± 2	
		AlO_4	72	2.5	7.3	5.2	1.0	35 ± 3	35 ± 3
B18	x = 2	AlO_6	6	1.6	0.0	0.0	0.0	2 ± 1	43 ± 5
		AlO_6	9	1.0	9.9	8.2	0.5	41 ± 5	
		AlO_5	34	0.6	5.6	3.9	0.1	4 ± 1	25 ± 2
		AlO_5	42	1.2	4.7	3.4	0.5	10 ± 1	
		AlO_5	50	1.7	6.0	5.0	0.5	11 ± 1	
		AlO_4	74	3.3	8.4	5.0	1.0	32 ± 7	32 ± 7

δ_{iso} = chemical shift, C_Q = quadrupole coupling constants, η_Q = asymmetry parameter

5.3.3 Structural details – X-ray and Neutron Diffraction

For further structural investigation sample B20 with an initial composition of 80 wt% Al_2O_3 and 20 wt% B_2O_3 (99% ^{11}B) was used, representing the compound with the best phase purity in the $Al_{6-x}B_xO_9$ series.

Difference Fourier calculations

Difference Fourier calculations were performed using neutron diffraction data collected at 4 K after the refinement of the atomic parameters. In a repetitive process the highest maximum is found for B2 in BO_3 groups at $x = 0.22$, $y = 0.28$, $z = 0.5$, corresponding to the position given in the published model [24], and with lower scattering density B1 (corresponding to BO_4 groups) and Al2 (corresponding to AlO_4 groups) at $x = 0.27$, $y = 0.20$, $z = 0.5$ and $x = 0.15$, $y = 0.33$, $z = 0.5$, respectively. Both positions are close to the positions determined by Mazza et al. [24]. The B1 position is assumed to be simultaneously occupied by aluminum and boron. Lower occupancy of the B1 position relative to B2 is in agreement with the results from NMR spectroscopy indicating a higher number of BO_3 groups in relation to BO_4 groups. Difference Fourier map for $Al_{6-x}B_xO_9$ ($x = 2$) for the x-y plane with z = 0.5 is given in Appendix A.

Rietveld refinements and DLS optimization

Rietveld refinements were performed combining the data of X-ray and neutron diffraction experiments, shown in Figure 5.7. Assuming mixed occupancy of Al and B on the B1 position, a fixed ratio was calculated from PGAA experiments, resulting in values of 0.20(1) for boron and 0.050(5) for aluminum on the 4h position. Nevertheless, as ^{11}B has a very low cross-section, it is difficult to quantify even by PGAA. Therefore the calculated composition should be considered as estimation. The refinement resulted in B-O distances of 166.8(11) pm, 176.32(74) pm and 221.5(11) pm in case of B1-O (BO_4) and 149.45(83) pm and 157.93(42) pm in case of B2-O (BO_3). Similar to Mazza et al. [24] these distances are significantly larger than the expected values of 137 pm for BO_3 [10] and 153 pm in case of Al/B mixed position, based on PGAA results. Refined Al-O (AlO_4) distances are still too short. The refined atomic parameters are given in Table 5.5.

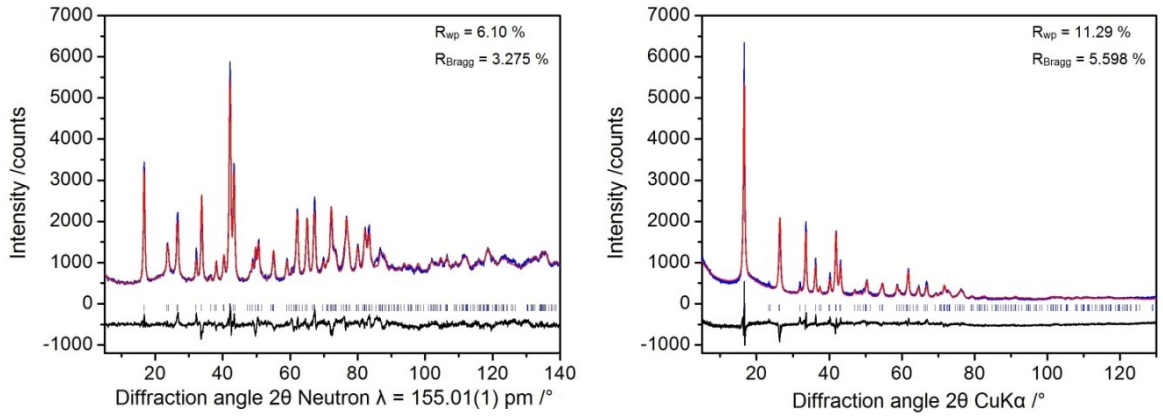

Figure 5.7. Rietveld plots of neutron powder diffraction data (left) and X-ray powder diffraction data (right) refinement results at room temperature. Observed intensities (blue line), calculated intensities (red line), positions of reflections (tick marks) and the difference curve between observed and calculated data (lower black line) are shown.

Table 5.5. Crystallographic data obtained from combined refinements of X-ray and neutron diffraction experiments at room temperature in *Pbam*, assuming mixed occupancy of Al and B on the B1 position (sample B20, enriched with ^{11}B).

Atom	multiplicity	Wyckoff	*x*	*y*	*z*	Occu.	B_{iso} /10^4 pm^2
Al1	2	*a*	0	0	0	1	0.59(7)
*B1	4	*h*	0.289(1)	0.203(1)	½	0.2	1.7(2)
*Al11	4	*h*	0.289(1)	0.203(1)	½	0.05	1.7(2)
Al2	4	*h*	0.1499(7)	0.3298(6)	½	0.5	2.8(1)
O1	4	*g*	0.1468(3)	0.20995(31)	0	1	2.34(6)
O2	4	*h*	0.3615(3)	0.4102(3)	½	1	1.55(5)
O3	2	*d*	0	½	½	0.5	5.6(2)
B2	4	*h*	0.221(1)	0.271(1)	½	0.25	0.1(1)

*Atomic coordinates refined using constraints with fixed occupancy (occu.) obtained from PGAA.

Lattice parameter: *a*: 7.5103(5)pm, *b*: 7.6155(5)pm, *c*: 2.8041(1)pm °

Probable split positions for oxygen were calculated by DLS modeling, using the lattice parameters and the atomic positions from a combined X-ray and neutron diffraction refinement. Linking two octahedral chains by a BO_3 group induces a local distortion in the octahedra. Optimizing the octahedral oxygen atom distances bonded to boron atoms resulted in a tilting of the octahedral chain as shown in Figure 5.8. This tilting is very similar to the chain tilting observed for $PbMBO_4$ phases [32, 33, 73, 85]. The B-O distances approach the ideal distance of 137 pm in a nearly planar 3-fold coordination.

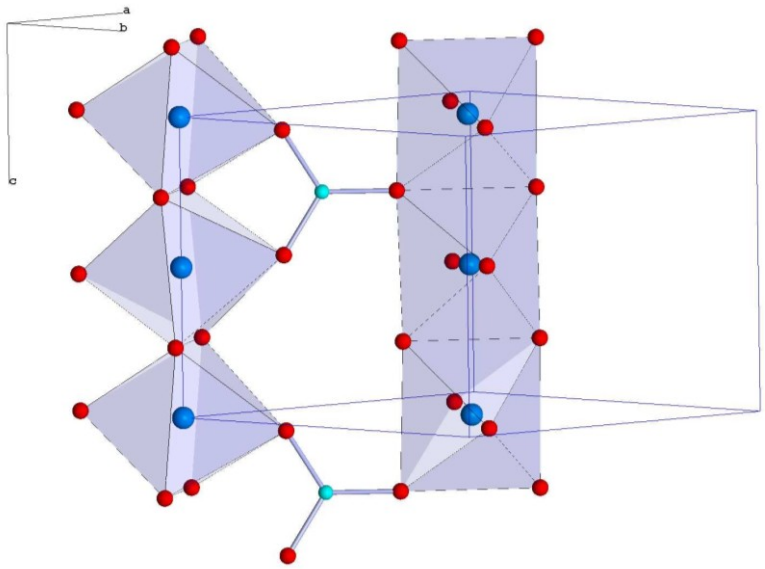

Figure 5.8. Part of the simulated $Al_{6-x}B_xO_9$ crystal structure, showing the tilting within the octahedral chain, most pronounced in **c**-direction; positions of all oxygen atoms were optimized by DLS modeling.

Transforming the calculated split positions for the oxygen atoms in the local environment of boron to a theoretical average model in *Pbam*, the resulting atomic parameters are listed in Table 5.6. The occupancies of these split positions should be related to the BO_3 content in the unit cell. DLS optimization linking two octahedral chains by a BO_4 group resulted in an increase of the local octahedral distortion leading to intra-tetrahedral O-O distances being too short.

Table 5.6. Theoretical average structure model obtained from the DLS optimization with triclinic symmetry transformed into *Pbam*.

Atom	*Pbam*	*x*	*y*	*z*
Al1	2*a*	0	0	0
O1	4*g*	0.14679	0.20968	0
O11	8*i*	0.14679	0.20968	0.0841
O2	4*h*	0.3618	0.4108	½
O21	4*h*	0.3595	0.39094	½
B2	4*h*	0.2214	0.2695	½

Structure refinements with split positions in a lower symmetry are not possible or meaningless because of the low data quality due to a crystallite size of about 16 nm leading to significantly broadened and therefore strong overlapping of the diffraction peaks. However, the DLS results describe possible local configurations which cannot be inferred from the refinement of the average structure.

5.3.4 Thermal behavior

Sample B20, enriched with ^{11}B, was used for the temperature-dependent investigations. We found $Al_{6-x}B_xO_9$ to be stable up to 1280 K. In all three directions the average linear expansion coefficient between 500 K and 1000 K is quite small: $\alpha_a = 6.2(7)\cdot10^{-6}$ K^{-1}, $\alpha_b = 6.1(11)\cdot10^{-6}$ K^{-1}, $\alpha_c = 4.8(7)\cdot10^{-6}$ K^{-1}. Note that the thermal expansion coefficient (TEC) is not linear at any temperature but close to above about 500 K till the beginning decomposition. This could be seen from the results of the DEA calculations shown in Figure 5.9. The modeling of the lattice thermal expansion was carried out from the composite data obtained from the HT-XRD and LT-NPD. Plots of the Rietveld-refinements for selected temperatures of high- and low temperature experiments are given in Appendix B.

Details of the thermal expansion microscopic modeling using the Debye-Einstein-Anharmonicity (DEA) equation was reported elsewhere [67, 73, 86-88]. For all metric parameters a single Debye term ($d = 1$, $e = 0$, $k_A = 0$) was required, resulting in the thermo-elastic constant $k = \gamma/K_0$ (γ = Grüneisen

parameter, K_0 = bulk modulus) for the Grüneisen first-order equation of state as given in Table 5.7. Taking the thermodynamic Grüneisen parameter as unity K_0 was extracted to be 190(1) GPa and a Debye temperature of 1197(71) K. The axial linear incompressibility's are in the order K_{0c} (343(1) GPa) > K_{0b} (130(1) GPa) > K_{0a} (107(1) GPa) similar to the order observed for mullites [1] and mullite-type materials [89-91]. Unlike mullite, the thermal expansion behavior does not violate the empirical rule (the lowest thermal expansion occurs to the elastically stiffest crystal direction) as the axial thermal expansion coefficient (α_a, α_b and α_c, respectively for *a*-, *b*- and *c*-cell parameter) follows as $\alpha_a > \alpha_b > \alpha_c$ at ambient condition.

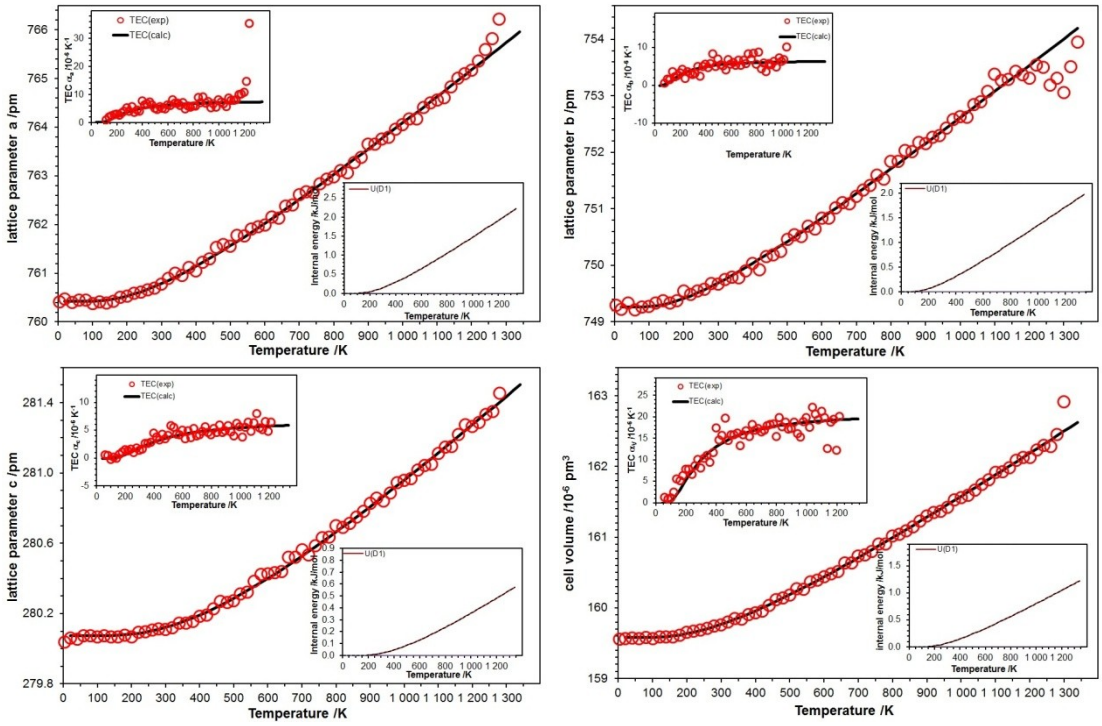

Figure 5.9. Temperature-dependent evolution of the lattice parameters, thermal expansion coefficients (inset, top-left) along with the model fit (solid line), and internal energy (inset bottom-right).[5]

The thermal expansion coefficients at 300 K are given as $\alpha_a = 3.9(9) \cdot 10^{-6}$ K^{-1}, $\alpha_b = 2.7(9) \cdot 10^{-6}$ K^{-1} and $\alpha_c = 1.4(9) \cdot 10^{-6}$ K^{-1}. However, to validate these results experimental and/or theoretical values of either the linear incompressibility's or the axial Grüneisen parameters are required. The mean Debye temperature (1246(45) K) calculated from the corresponding axial values (Table 5.7) is in good agreement within one estimated standard deviation. For the thermodynamically stable polymorph of A_2B a linear expansion of $\alpha_a > \alpha_b > \alpha_c$ was observed, in which the *c*-lattice parameter remain nearly constant [60].

[5] Figure 5.9: modified reproduction from 92. Hoffmann, K., T.J.N. Hooper, M.M. Murshed, O. Dolotko, Z. Révay, A. Senyshyn, H. Schneider, J.V. Hanna, T.M. Gesing, and R.X. Fischer (2016): *Formation, stability and crystal structure of mullite-type $Al_{6-x}B_xO_9$* Journal of Solid State Chemistry, **243**: p. 124-135.

Table 5.7. DEA parameters obtained for $Al_{6-x}B_xO_9$ for the unit cell volume *V* and the orthorhombic lattice parameters *a*, *b*, and *c*.

	V	*a*	*b*	*c*
M_0*	159.6(1)	760.4(1)	749.3(1)	280.1(1)
k_{D1} /10^{-12} GPa^{-1}	5.2(3)	9.3(4)	7.7(3)	2.9(1)
θ_{D1} /K	1197(79)	1125(46)	871(38)	1741(50)

*cell parameters *a*, *b*, *c* and cell volume *V* at 0 K given in pm and$10^6$$pm^3$, respectively.

5.4 Conclusions

The synthesis of mullite-type aluminum borate compounds is a complicated process. Small differences in temperature, heating period, humidity or homogeneity have an influence on the resulting products. Although the add-on of glycerin should avoid appreciable volatilization of boric acid above 373 K during synthesis [24, 71], a loss of boron is likely, as a shift of the phase formation towards more aluminum rich phases can be observed for increasing heating periods.

We found $Al_{6-x}B_xO_9$ phases to crystallize in the compositional range between 13.17 – 25.45 wt% B_2O_3 (corresponding to $1.09 \leq x \leq 2$) in the precursor phase. The lattice parameters of the resulting products are clearly orthorhombic with $a \neq b$ and thus do not represent a pseudo-tetragonal metric as observed in [24]. The successive decrease of the lattice parameters upon increasing boron content and the results of NMR spectroscopy indicate a complete solid solution series. Aluminum is expected to be partially replaced by boron on the 4-fold coordinated position confirmed by spectroscopic data. A preference of boron in 3-fold coordination is supported by the ^{11}B NMR spectra and the Fourier calculations.

The strong B-O bonds of the trigonal planar coordinated boron (BO_3) leads to distortion of neighboring octahedra, most probably causing a decrease of the cell dimension most pronounced in the **c**-direction, relative to the **a**- and **b**-direction, as also observed for B-doped mullite [30]. A strong disorder in the inter-chain groups (BO_3, BO_4 and AlO_4) leads to a varying degree of octahedral distortion. This might explain the observed disorder in the AlO_6 site increasing with increasing B content, as the smaller BO_x units will induce distortion of the AlO_6. Structure refinements could not confirm AlO_5 groups taking the ^{27}Al MAS NMR data in the range of 34 - 50 ppm. They are mainly assigned to tri-cluster units (corresponding to earlier observations [73]) or could be a result from a rearrangement of AlO_4 units with an additional longer bond to an octahedral oxygen atom as a result of strongly distorted octahedra. Based on results obtained here an optimized structural model for $Al_{6-x}B_xO_9$ is given.

Acknowledgements

We gratefully thank the Deutsche Forschungsgemeinschaft (DFG) for the financial support of the projects **GE1981/5-1** and **FI442/19-1**, as well as the financial support provided by FRM II to perform the neutron scattering measurements at the Heinz Maier-Leibnitz Zentrum (MLZ), Garching, Germany. TMG thanks the DFG for support in the Heisenberg program GE1981/3-1 and GE1981/3-2. JVH thanks the EPSRC, the University of Warwick and the Birmingham Science City Program for partial funding of the solid state NMR infrastructure at Warwick. The latter program accessed the Birmingham Science City Advanced Materials Project 1: Creating and Characterizing Next Generation Advanced Materials, which derived support from Advantage West Midlands (AWM) and the European Regional Development Fund (ERDF). This work is based upon experiments performed at the SPODI instrument operated by O. Dolotko und A. Senyshyn, and experiments performed at the PGAA instrument operated by Zs. Révay at the Heinz Maier-Leibnitz Zentrum (MLZ), Garching, Germany.

Supplementary information

Appendix A

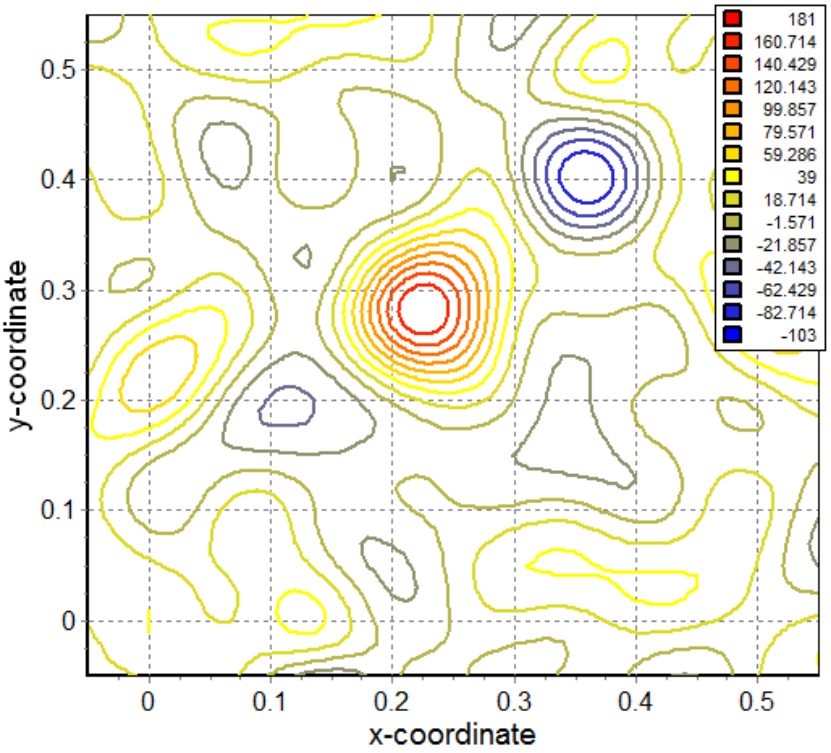

Figure S.5.1. Difference Fourier map for $Al_{6-x}B_xO_9$ (x = 2) for the x-y plane with z = 0.5 showing a distinct maximum at x = 0.22, y = 0.28, z = 0.5 representing the B2 position.

Appendix B

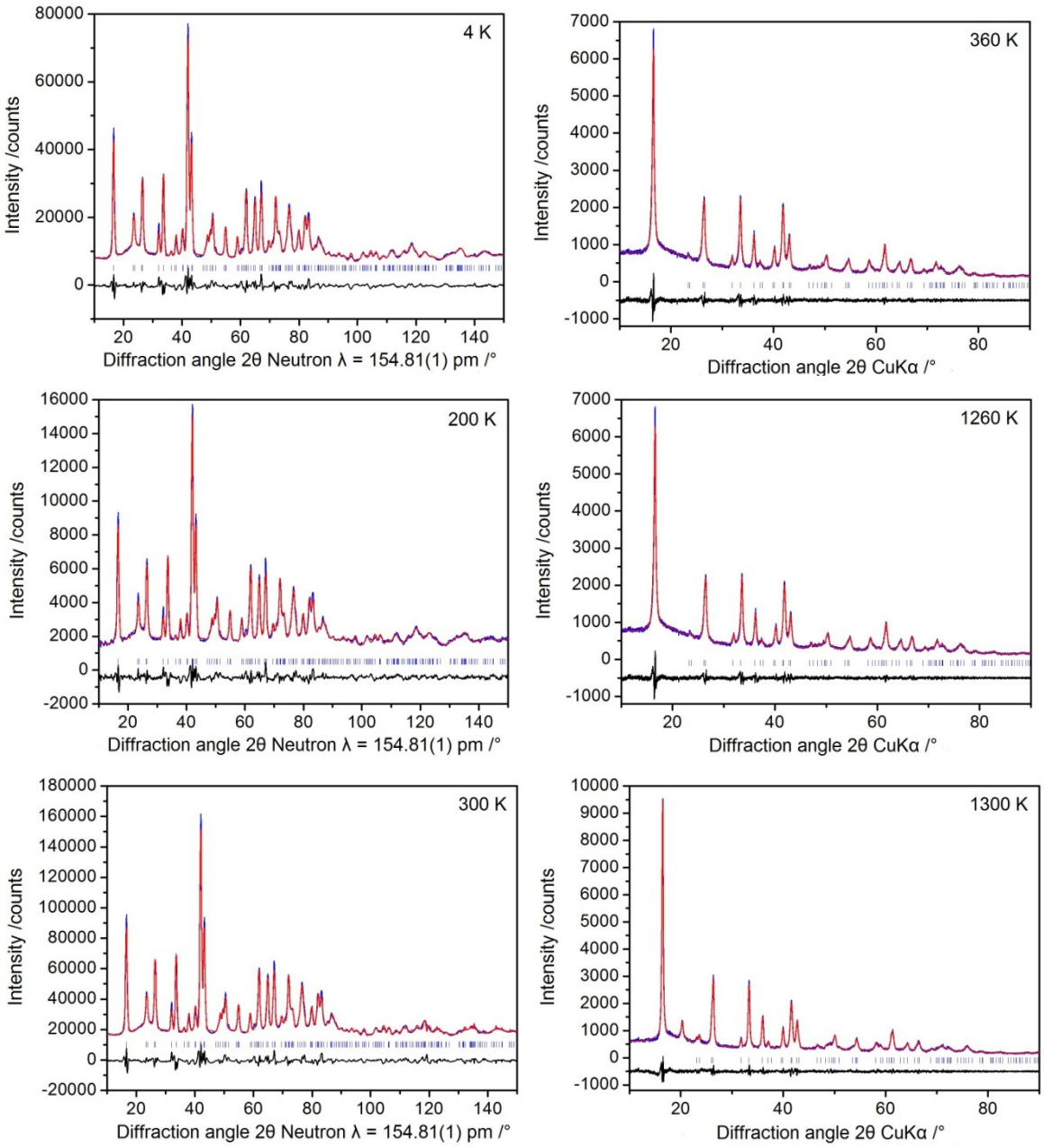

Figure S.5.2. Rietveld plots of LT-neutron powder diffraction data (left) and HT-X-ray powder diffraction data (right) refinement results for selected temperatures. At 1300 K an additional diffraction peak at about 20° 2θ is observed, which can be assigned to the thermodynamically more stable polymorph of A_9B_2, indicating a decomposition of $Al_{6-x}B_xO_9$. Observed intensities (blue line), calculated intensities (red line), positions of reflections (tick marks) and the difference curve between observed and calculated data (lower black line) are shown. The R_{wp} for the displayed refinements of the high-temperature X-ray diffraction data varies in the range of R_{wp} = 5.73% - 6.0%, the corresponding values for the displayed low temperature neutron diffraction data vary in the range of R_{wp} = 4.45% - 5.3%.

6 Crystal chemical characterization of mullite-type aluminum borate compounds

K. Hoffmann[a,b*], T. J. N. Hooper[c], H. Zhao[d], U. Kolb[d], M. M. Murshed[b,e], M. Fischer[a], H. Lührs[a,e], G. Nénert[f]1, P. Kudějová[g], A. Senyshyn[g], H. Schneider[a], J. V. Hanna[c], Th. M. Gesing[b,e], R. X. Fischer[a,e]

[a]Kristallographie, FB05, Klagenfurter Straße / GEO, Universität Bremen, D-28359 Bremen, Germany
[b]Institut für Anorganische Chemie und Kristallographie, FB02, Leobener Straße / NW2, Universität Bremen, D-28359 Bremen, Germany
[c]Department of Physics, University of Warwick, Coventry, CV4 7AL, UK
[d]Institut für Anorganische Chemie und Analytische Chemie, Duesbergweg 10-14, Johannes Gutenberg-Universität Mainz, D- 55128 Mainz, Germany
[e]MAPEX Center for Materials and Processes, Universität Bremen, Bibliothekstraße 1, D-28359 Bremen, Germany
[f]Institut Laue-Langevin, 6 Rue Jules Horowitz, 38042 Grenoble Cedex 9, France
[g]Heinz Maier-Leibnitz Zentrum (MLZ), Technische Universität München, Lichtenbergstr. 1, D-85748 Garching, Germany

[1]PANalytical B. V., Lelyweg 1, 7602 EA Almelo, The Netherlands

In preparation; will be submitted soon[6]

*Corresponding author; email address: Kristin.Hoffmann@uni-bremen.de; phone: +49 (0)421 218 65172; fax: +49 (0)421 218 65189

Abstract

Al-rich aluminum borate compounds were prepared along different synthesis routes and with various initial Al/B ratios, characterized by diffraction methods, spectroscopy and prompt gamma activation analysis. The ^{11}B NMR data show a small amount of BO_4 to be present in all samples. The chemical analysis indicates a trend in the Al/B ratio instead of a fixed composition. Both methods indicate a solid solution expressed as $Al_{5-x}B_{1+x}O_9$ with Al substituting B in the range of about 1 – 3 %.

The structure of the B-rich compound $Al_4B_2O_9$ was re-investigated by electron diffraction methods, showing that structural details vary inside a crystallite. Predominant are domains with an ordered distribution of atoms, showing no significant signal for the second postulated channel oxygen atom O5. Other domains show a probable disordered configuration of O5 and O10, indicated by diffuse scattering along the **b** direction.

Keywords: Aluminum borate, mullite-type sturcture, X-ray diffraction, electron diffraction, NMR spectroscopy, PGA analysis.

[6] Based on this chapter a manuscript will be submitted to the Journal of Solid State Chemistry

6.1 Introduction

The aluminum borates $Al_{18}B_4O_{33}$ (A_9B_2) and $Al_4B_2O_9$ (A_2B) belong to the family of mullite-type materials [1, 2], with the characteristic chains of edge-sharing octahedra, interconnected by AlO_5-, AlO_4-, BO_3- and/or BO_4-groups. Because of their outstanding properties, such as low thermal expansion, high elastic modules and high tensile strength, A_9B_2 and A_2B are of considerable research interest [44]. A_9B_2 is commercially available under the trade names Alborex and Alborite (Shikoku Chemical Corporation, Japan). The reinforcement of aluminum alloys by the incorporation of these Al-borate whiskers to obtain composite materials with high mechanical strength is one of their most important applications [44] (see, e.g., Tang et al. [93], Peng et al. [94] and Tao et al. [95] for further applications). However, the complex details of both crystal structures could not be solved yet. A_9B_2 and A_2B are described to be the thermodynamically stable phases in the Al_2O_3-B_2O_3 system [43]. A series of $Al_{6-x}B_xO_9$-compounds considered to be metastable has been described by Mazza et al. [24]. These compounds have an average structure close to mullite, crystallizing in the orthorhombic space group *Pbam*. A more detailed discussion about these $Al_{6-x}B_xO_9$-phases is available elsewhere [92].

For the thermodynamically stable polymorph of the Al-rich aluminum borate the exact chemical composition is an ongoing discussion. Two slightly different stoichiometries are reported: $Al_{18}B_4O_{33}$ (A_9B_2) and $Al_{20}B_4O_{36}$ (Al_5BO_9), crystallizing in the orthorhombic space group $A2_1am$ [26]. Crystal-structure refinements performed by Sokolova et al. [46] yielded a chemical composition of $Al_{19.4}B_{4.6}O_{36}$, being rounded to $Al_{20}B_4O_{36}$. Although the composition given by Sokolova et al. [46] is closer to $Al_{18}B_4O_{33}$, this compound was referenced further on as Al_5BO_9 (A_5B), as pointed out by Fischer and Schneider [2]. Based on an ordered distribution of Al and B, $Al_{20}B_4O_{36}$ (A_5B) represents the idealized model. Nevertheless, a replacement of less than 2% of the Al atoms by B would yield the $Al_{18}B_4O_{33}$ composition ($Al_{20}B_4O_{36}$ vs. $Al_{19.64}B_{4.36}O_{36}$) as described by Ihara et al. [35] and Garsche et al. [26]. Gatta et al. [47] and Fisch et al. [48] assumed a composition in a range close to Al_5BO_9. The Al-rich aluminum borate consists of AlO_6-, AlO_5- and AlO_4- polyhedra, B occurs in trigonal borate groups (BO_3) also found and confirmed in mullite-type $PbMBO_4$ phases (M = Al, Ga, Fe, Mn) [85, 96-98]. A solid-solution series might be possible replacing Al by B on the AlO_4 site. However, the difference of the ionic radii between B and Al would lead to a higher degree of tetrahedral distortion which might affect the thermal properties of these materials. The thermal stability of the Al-rich aluminum borate is described controversially in literature. Incongruent melting is observed at about 2223 K by Bauman and Moore [45] and Gielisse and Foster [43]. Scholze [13] determined an incongruent melting point at about 1713 K, and Rymon-Lipinski et al. [49] described a decomposition into Al_2O_3 and liquid B_2O_3 at 1473 K. For the commercial products Alborite and Alborex the Shikoku Chemical Corporation specified the decomposition temperature as 1713 K, describing the decomposition products as alumina and boron oxide [99].

The thermodynamically stable polymorph of the boron-rich aluminum borate A_2B is described by Fischer et al. [25] in the monoclinic space group *C*2/*m* in an enlarged unit cell, with all lattice parameters doubled with respect to the *Pbam* structure and a monoclinic angle *ß* close to 90°. Its crystal structure is closely related to the boralsilite structure with Si replaced by B [25]. However, details of this complex structure concerning disorder of the oxygen atoms in the channels (O5 and O10), and disorder of the interstitial cations could not be solved yet.

The aim of this work is a detailed crystal-chemical characterization of the compounds A_9B_2 and A_2B, using complementary diffraction and spectroscopic methods. Structural changes of the crystal structures will be investigated as a function of the B content in the precursor phases. A_9B_2 compounds are produced by different synthesis routes and compared to Alborite and Alborex. Moreover, the thermal stability of A_9B_2 is investigated.

6.2 Materials and methods

6.2.1 Synthesis

Sol-gel synthesis. Series of powder samples were synthesized with a varying Al_2O_3/B_2O_3 ratio in the precursor phase using the nitrate decomposition method (ND) described elsewhere [24, 60, 61]. Aluminum nitrate nonahydrate [$Al(NO_3)_3 \cdot 9H_2O$] and boric acid [$B(OH)_3$] were mixed and dissolved in 10 wt% glycerol [1,2,3-propanetriol]. The reaction of glycerol and boric acid at room temperature (RT) yields the formation of ester complexes, thus reducing the volatilization of boron [24]. A_9B_2/A_5B powder samples were prepared with an excess of 10 mol% boron, allowing the formation of $Al_{18}B_4O_{33}$ and/or $Al_{20}B_4O_{36}$ despite the possible loss of boron during the synthesis. Using covered platinum crucibles, A_2B and A_9B_2/A_5B powder samples were crystallized at 1223 K for 44 h and at 1373 K for 5 h, respectively. All samples were quenched from reaction conditions to room temperature. The neutron diffraction samples (A5 and B16) were synthesized using 99 atom% ^{11}B raw materials in order to account for the very high absorption cross section of the isotope ^{10}B. The sample A_2B (A5) was finally heated at 1023 K for one hour, followed by a three days heating period at 1223 K. The A_9B_2/A_5B sample (B16) was prepared from a single-phase gel consisting of aluminum nitrate nonahydrate and boric acid, following the procedure described by Griesser et al. [28] but using glycerol instead of ethanol, the final synthesis step was performed at 1473 K for 5h.

Solid-state reaction. Series of A_9B_2/A_5B powder samples were synthesized using a solid-state reaction (S) described in [48]. Aluminum oxide [α-Al_2O_3] and boron oxide [B_2O_3] were mixed in the corresponding ratios, again using an excess of 10 mol% boron. Carefully grained and pressed as a pellet they were crystallized at 1473 K for 10 h in covered corundum crucibles, and slowly cooled to room temperature.

Solid-state and sol-gel-samples were washed with hot deionized H_2O to remove possible impurities of boron oxide. The experimental conditions used for sample characterization are given in Tables 6.1 and 6.2. Chemical compositions and composition ratios given in this work always refer to the initial gel composition used in the synthesis. Due to a partial loss of B during the synthesis the actual composition of the AB phases can be different.

Table 6.1. Initial gel compositions of samples of the A_2B series.

Exp.	Al_2O_3 /wt%	B_2O_3 /wt%	Method	Temp. /K	Time /h
A1	70	30	ND	1223	44
A2	65	35	ND	1223	44
A3	60	40	ND	1223	44
A4	35	65	ND	1223	44
A5	31	69 (^{11}B)	ND	1223	72

ND: nitrate decomposition method

Table 6.2. Initial gel compositions of samples of the A_9B_2/A_5B series.

Exp.	Al_2O_3/B_2O_3	Method	Temp. /K	Time /h
B6	5.0:1.1	ND	1373	5
B7	4.5:1.1	ND	1373	5
B8	3.0:1.1	ND	1373	5
B9	1.5:1.1	ND	1373	5
B10	1.0:1.1	ND	1373	5
B11	5.0:1.1	S	1473	10
B12	4.5:1.1	S	1473	10
B13	3.0:1.1	S	1473	10
B14	1.5:1.1	S	1473	10
B15	1.0:1.1	S	1473	10
B16	4.5:1.0 (^{11}B)	ND	1473	5

ND: nitrate decomposition method; S: solid-state reaction

6.2.2 Diffraction

X-ray powder diffraction

X-ray powder-diffraction data were collected on a Philips X'Pert diffractometer using $CuK\alpha_{1,2}$ radiation and Bragg-Brentano geometry. The instrument is equipped with a ¼° divergence slit, a ½° anti-scatter slit, a soller slit (0,04 rad) and a mask (10 mm) in the primary beam, as well as a soller slit (0,04 rad), a Ni-filter and a X'Celerator detector system in the secondary beam. Data were collected from 3° - 120° 2θ (or 5° - 130° 2θ) with a stepsize of 0.0167° 2θ/step and a measuring time of 50 s per step, using tube settings of 45 kV and 40 mA.

Powder X-ray diffraction data for small amounts of samples (samples of A_9B_2/A_5B series, investigated by thermal analysis) were collected using glass capillaries of 0.3 mm in diameter on a Bruker D8 diffractometer with Debye-Scherrer geometry. Monochromatic $CuK\alpha_1$ radiation (λ = 154.0598 pm) is provided by a Ge-monochromator of Johansson type (Vario 1). The instrument is equipped with an antiscatter slit (0.1 mm) and a soller slit (4°) in the primary beam, as well as a soller slit (2.5°), an iris aperture (6.42 mm) and a position sensitive detector (LynxEye) in the secondary beam. Data were collected in the range from 4° - 120° 2θ, with a stepsize of 0.01976° 2θ/step and a measuring time per step of 1s with tube settings of 40kV and 40mA.

Neutron powder diffraction

Neutron powder-diffraction (NPD) data were collected for the A_9B_2/A_5B sample at room temperature on powder diffractometer SPODI@FRM-II [72] in the high-resolution mode. A collimated beam of neutrons (λ = 154.838(2) pm) was provided by a Ge(551)-monochromator with a take-off angle of 155°. Data were refined in the range from 5° – 150° 2θ, with a stepsize of 0.05° 2θ/step.

Neutron powder-diffraction data for the A_2B sample were collected at room temperature at the Institut Laue Langevin. The measurements were carried out with a wavelength of 159.4 pm corresponding to the (335) Bragg reflexion of a germanium monochromator. The neutron detection is performed with ^{3}He counting tubes spaced at 1.25° intervals. The data were refined in the range from 10° – 140° 2θ. A complete diffraction pattern is obtained after about 25 steps of 0.05° in 2θ.

Rietveld refinements

Rietveld refinements based on the X-ray and neutron powder-diffraction data were carried out for all crystalline samples using the "DiffracPlus Topas 4.2" (Bruker AXS GmbH, Karlsruhe, Germany) software. Impurities of Al_2O_3 were quantified if present. The lattice parameters of all samples were refined by a Pawley fit. The fundamental parameters were obtained from the refinement of a LaB_6 standard sample and fixed for all subsequent structure refinements. For Rietveld refinements of combined neutron and X-ray diffraction data the neutron wavelength was refined while the X-ray wavelength was fixed and the lattice parameters were refined simultaneously but constrained to be equal for both data sets. Difference Fourier calculations are based on refinements using the BRASS [50] software.

Electron Diffraction

Scanning transmission electron microscopy (STEM) and electron-diffraction measurements were carried out using a TECNAI F30 S-TWIN transmission electron microscope equipped with a field emission gun and operating at 300 kV. STEM images were collected by a FISCHIONE high angular-annular dark field (HDAAF) detector. Nano electron-diffraction data were acquired with a 4k Gatan CCD camera (Gatan, Pleasanton, USA) using automated diffraction tomography (ADT) module [100]

at room temperature. ADT data from single crystals were collected with a FISCHIONE tomography holder.

6.2.3 Spectroscopy

MAS NMR Spectroscopy

The ^{11}B MAS NMR measurements were undertaken at 14.1 T using a Varian-600 spectrometer operating at the ^{11}B Larmor frequency of 192.50 MHz. All ^{11}B MAS NMR data were acquired using a Varian 4mm HX MAS probe which enabled a MAS frequency of 12 kHz throughout. Each reported measurement employed a 'selective' $\pi/2$ pulse time of 5 μs, inferred from a 'non-selective' $\pi/2$ pulse time of 10 μs measured on $NaBH_4$(s), with a recycle delay of 20 s. The quantitative nature of these measurements was tested on selected samples against experiments utilizing smaller flip angles (with the same radio frequency power levels) that satisfied the uniform excitation condition for quadrupolar nuclei [74, 75] where $(I + ½)\ \omega_{rf} t_p \leq \pi/6$. In this case, a 'selective' (solid) $\pi/9$ pulse time of 1.1 μs with a recycle delay of 20 s was used to ensure that the relative ratio between the BO_3 and BO_4 species remained unchanged, although a much longer acquisition time of >24 h for each measurement was necessary to achieve sufficient signal/noise for this purpose. All ^{11}B chemical shifts were referenced to $BF_3.Et_2O$ (δ_{iso} 0.0 ppm) via a secondary solid $NaBH_4$ reference (δ_{iso} –42.06 ppm), and each ^{11}B MAS NMR spectrum was simulated using the DMFit program to elucidate the relative proportions of the BO_3 and BO_4 species [51].

The ^{27}Al MAS NMR measurements were undertaken at 14.1 T and 9.40 T using a Bruker Avance II+-600 spectrometer operating at the ^{27}Al Larmor frequency of 156.34 MHz and a Bruker Avance 400 spectrometer operating at the ^{27}Al Larmor frequency of 104.23 MHz, respectively. All ^{27}Al MAS NMR data were acquired using a Bruker 3.2mm HX MAS probe which enabled a MAS frequency of 20 kHz throughout. The 14.1 T ^{27}Al MAS data were acquired using a single pulse experiment which employed a 'selective' 0.80 μs excitation pulse corresponding to a $\pi/6$ flip angle, inferred from the 'non-selective' $\pi/2$ pulse time of 7.5 μs measured on the AlO_6 resonance of YAG(s), and a recycle delay of 2 s. The corresponding 9.40 T ^{27}Al MAS data were acquired using the same pulse time calibration on the AlO_6 $YAG_{(s)}$ resonance, with the single pulse experiments employing a slightly longer 1 μs 'selective' excitation pulse and a recycle delay of 10 s. These pulse conditions at both B_0 fields ensured a 1:1 intensity ratio in the AlO_4 and AlO_6 species of the YAG spectrum. The 14.1 T 2D ^{27}Al MQMAS NMR data were acquired using a Z-filtered 3QMAS pulse sequence with a 3.5 μs excitation pulse, a 1.5 μs conversion pulse and a 17.0 μs selective final pulse. These MQMAS data were processed using TOPSPIN and then sheared using the TOPSPIN AU program *xfshear*. All ^{27}Al chemical shifts were referenced to 1 M $Al(NO_3)_3$(aq) (δ_{iso} 0.0 ppm) via a secondary solid YAG reference (δ = 0.7 ppm for the AlO_6 site).

Infrared Spectroscopy

Fourier transform infrared (FTIR) spectra were collected on a Bruker Vertex 80v FTIR spectrometer. Using the standard KBr method for the mid-infrared (MIR) region, 1 mg sample was homogenized with 200 mg KBr, pressed into a pellet and measured relative to a KBr reference pellet. Data were obtained in a spectral range of 370 cm^{-1} – 4000 cm^{-1} with a spectral resolution of 2 cm^{-1} and 32 scans per spectrum.

Raman Spectroscopy

Powder Raman spectra were collected on a Horiba LabRam Aramis using a laser of 532.04 nm wavelength. The spectra were recorded on pellets from 50 cm^{-1} to 1600 cm^{-1} with a spectral resolution of approx. 3.22 cm^{-1} and a grating of 1800 groves/mm. Pellets were pressed from the powder samples. The spectra were baseline corrected using the LabSpec Software, vers.5.

6.2.4 Density-functional theory calculations

In order to obtain more insights into the energetic stability of the positions of oxygen atoms O5 and O10, density-functional theory (DFT) calculations were performed for two different models of A_2B. In the first model, the oxygen atom O5 was removed from the structure whereas the occupancy of O10 was increased to 1 to arrive at the correct stoichiometry (this model retains *C2/m* symmetry). In the second model, the symmetry was reduced to *Cm*, and half of the O5 and O10 atoms were removed.
The DFT calculations used the CASTEP code, which employs a combination of plane waves and pseudopotentials [101]. On-the-fly generated ultrasoft pseudopotentials were used to represent the core electrons, and the energy cutoff was set to 700 eV. The calculations employed the PBEsol functional, which was optimized for the treatment of solids [102]. A 1×2×1 mesh of *k*-points was used to sample the first Brillouin zone. While all atomic coordinates were relaxed in the DFT calculations, the lattice parameters were fixed to the experimental values [25].

6.2.5 Thermal analyses

Powder samples of A_9B_2/A_5B series were investigated by differential thermal analysis (DTA), on a Netzsch 449 F3 Jupiter STA, combining the signals of differential scanning-calorimetry (DSC) and thermal gravimetric analysis (TG). Different types of measurements were performed to investigate the stability range of selected samples and of the commercial products Alborite and Alborex. In the first case, samples were studied up to 1773 K (heating rate: 5 K/min; cooling rate: 30 K/min), in the second case, samples where heated up to 1673 K, holding this temperature for 5 h (heating rate: 20 K/min; cooling rate: 30 K/min). All experiments were performed using uncovered crucibles and dry synthetic

air atmosphere with a controlled gas flow (50 ml/min). Proteus Netzsch software [53] was used for data evaluation.

6.2.6 Prompt gamma activation analysis

Prompt gamma activation analysis (PGAA) was performed on selected samples of A_9B_2/A_5B series and of the commercial products Alborite and Alborex to determine the exact Al/B ratio. Since boron is known to be volatile, volatilization of an unknown amount of boron during the synthesis is likely. A 15 mm lead attenuator and a special instrument configuration were used. Additional efficiency measurements were performed for these boron containing samples as discussed in [55]. Details of the PGAA system are described in [76, 103].

6.3 Results and discussion

6.3.1 Crystal-chemical characterization of $Al_{20-x}B_{4+x}O_{36}$

6.3.1.1 X-ray and Neutron Powder diffraction

Based on X-ray diffraction patterns the products of the different synthesis routes and different initial Al/B ratios are compared. Pure and well crystallized A_9B_2/A_5B phases are observed in solid state derived samples B13-B15 which belong to the high B_2O_3 region (Tab. 6.2). In the high Al_2O_3 region (B11, B12) close to the A_9B_2 phase boundary [43] additional diffraction peaks occur, which can be assigned to α-alumina most probably resulting from a loss of boron. For comparable samples with the same initial composition synthesized using the nitrate decomposition method (B6, B7) formation of alumina was not observed. This supports the argument of Mazza et al. [24] and our finding pointing out that the volatilization of boron is reduced due to the reaction of glycerine and boric acid at RT. Even for the sample B6 (Al/B > 4.5) the formation of Al_2O_3 is not observed. Therefore, the diffraction data suggest that the phase boundary might not be defined to the stoichiometric composition of $Al_{18}B_4O_{33}$ as published by Gielisse and Foster [43]. In the high B_2O_3 region, small amounts of the stable A_2B polymorph are observed as additional phase for samples B8 and B9 synthesized by the nitrate decomposition method. The reason might be that the synthesis temperature of the samples B5 - 9 (1373 K) is very close to the decomposition temperature of A_2B [13, 60]. Already in our previous work [92] it turned out that even small differences in temperature or homogeneity could have an influence in the synthesis products of aluminum borate compounds. The presence of boric acid derived from the hydration of previously amorphous B-O compounds was excluded by repeated collection of diffraction patterns for selected samples after two years.

The lattice parameters and the average crystallite size were refined using a Pawley fit. The samples B6 and B7 show various observed diffraction peaks are broadened or narrowed compared to the calculated profiles. This behavior varies within hkl series of different order and is obvious for the (111) reflection which is observed much more broadened than calculated and, in comparison, the (222) reflection is observed narrower than calculated. It is likely that theses effects are caused by disorder effects in the crystal structure supported by the results of ^{27}MAS NMR data (see part spectroscopy). A trend of an increasing crystallite size is observed for increasing initial boron content. Using the solid-state reaction, the crystallite size increases compared to samples synthesized by the nitrate decomposition method. A possible explanation is the higher synthesis temperature and longer heating period. No such trend is observed for lattice parameters and cell volume (Tab. 6.3).

Table 6.3. Refined lattice parameters and crystallite sizes for the A_9B_2/A_5B series.

Exp.	Initial Al_2O_3/B_2O_3	Method	Lattice parameter			Cell volume	Average crystallite size	Phase content Al_2O_3
			a /pm	*b* /pm	*c* /pm	V /10^6 pm^3	L_{Vol}(IB) /nm	/wt%
B6	5.0:1.1	ND	768.7(1)	1504.2(3)	566.94(6)	655.52(15)	25.4(3)	0
B7	4.5:1.1	ND	768.94(8)	1503.7(2)	566.94(5)	655.51(12)	26.3(3)	0
B8	3.0:1.1	ND	769.13(7)	1500.1(1)	565.74(3)	652.75(9)	38.2(3)	0
B9	1.5:1.1	ND	768.85(3)	1500.76(6)	566.45(2)	653.60(4)	88(1)	0
B10	1.0:1.1	ND	768.87(2)	1500.68(5)	566.57(1)	653.72(3)	130(2)	0
B11	5.0:1.1	S	769.34(2)	1501.35(4)	566.54(1)	654.39(3)	152(2)	6
B12	4.5:1.1	S	769.32(2)	1501.55(4)	566.518(9)	654.43(2)	169(2)	3
B13	3.0:1.1	S	769.23(2)	1501.23(4)	566.62(1)	654.33(2)	168(2)	0
B14	1.5:1.1	S	769.20(1)	1501.03(3)	566.773(9)	654.39(2)	184(2)	0
B15	1.0:1.1	S	769.21(1)	1501.04(3)	566.768(9)	654.40(2)	211(3)	0
B16*	4.5:1.0	ND	769.42(1)	1501.87(3)	566.429(8)	654.55(2)	128(1)	0
Alborite	unknown		769.41(3)	1501.95(7)	567.06(2)	655.30(5)	54.5(4)	0
Alborex	unknown		769.08(2)	1500.60(4)	567.34(2)	654.76(4)	209(3)	0

*result from combined X-ray and neutron powder diffraction data refinement
ND: nitrate decomposition method; S: solid-state reaction

Alborex is described having needle-like crystals, thus causing texture effects in (001)-direction. SEM images of Alborite and Alborex are shown in Figure 6.1 confirming Alborex to crystallize as whiskers, whereas Alborite occurs in small needles arranged in the form of spherical aggregates.

Rietveld refinements were performed on sample B16 enriched with ^{11}B, combining the data of X-ray and neutron-diffraction experiments. The refined atomic parameters using the original model of Garsche et al. [26] with all positions fully occupied are listed in Table 6.4. No preferred orientation effect in (001) is observed for the samples synthesized by us. A restriction of a minimum value of 0.2 * 10^4 pm^2 had to be used for the isotropic displacement parameter U_{eq} for boron in order to prevent

the refinement to a negative value. The Rietveld plots of both X-ray and neutron diffraction data are shown in Figure 6.2.

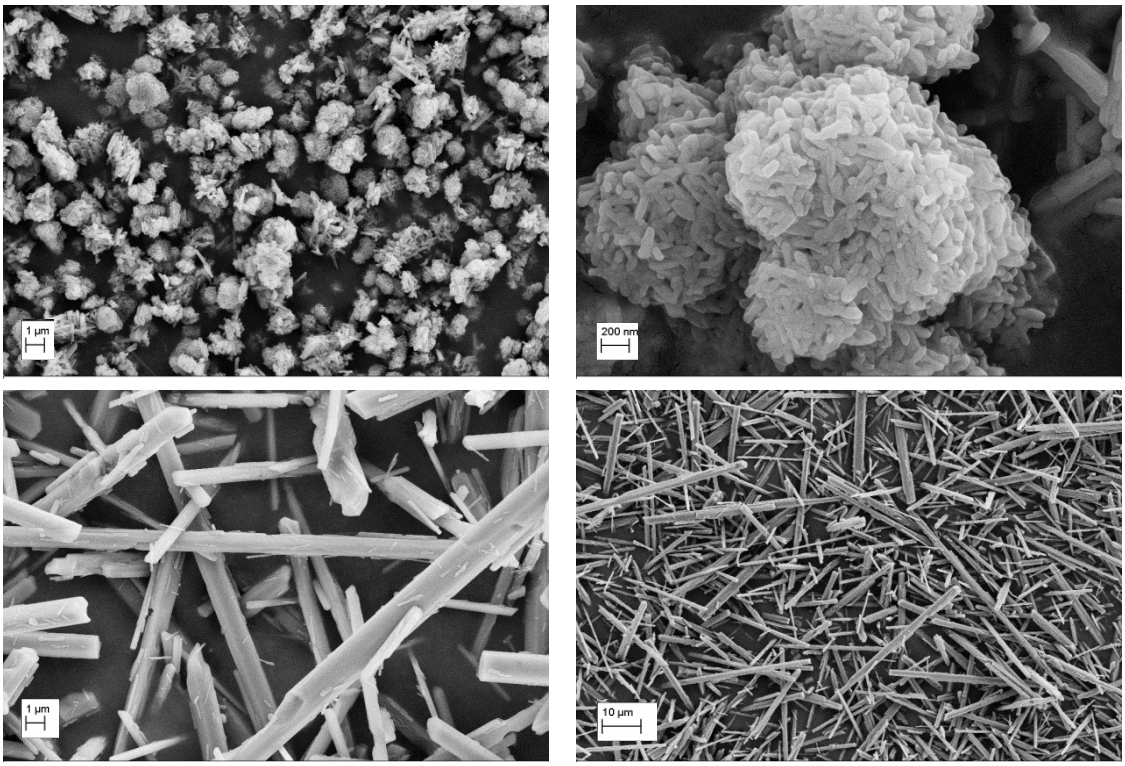

Figure 6.1. SEM images obtained for Alborite (top) and Alborex (bottom), carried out on a Jeol JSM-6510 scanning electron microscope [Jeol (Germany) GmbH, Echingen, Germany] using an excitation voltage of 10 kV.

Table 6.4. Crystallographic data obtained from combined refinements of X-ray and neutron diffraction data using the model of Garsche et al. [26].

Atom	multiplicity	Wyckoff	*x*	*y*	*z*	Occu.	B_{iso} /10^4 pm^2
B1	4	*a*	0.7194(5)	0.0155(2)	0	1	0.2*
Al1	8	*b*	1/2	0.3832(1)	0.2479(4)	1	0.14(3)
Al2	4	*a*	0.6881(4)	0.2445(2)	1/2	1	0.23(5)
Al3	4	*a*	0.6810(5)	0.0549(2)	1/2	1	0.42(5)
Al4	4	*a*	0.8323(5)	0.2974(2)	0	1	0.15(5)
O1	8	*b*	0.7846(4)	0.0479(1)	0.2117(3)	1	0.33(3)
O2	8	*b*	0.7012(4)	0.3103(1)	0.2426(3)	1	0.22(3)
O3	4	*a*	0.5369(4)	0.1480(2)	1/2	1	0.31(4)
O4	4	*a*	0.9351(5)	0.1923(2)	0	1	0.21(4)
O5	4	*a*	0.8704(4)	0.1703(2)	1/2	1	0.21(4)
O6	4	*a*	0.5729(4)	0.4548(2)	0	1	0.12(4)
O7	4	*a*	0.5916(4)	0.4529(2)	1/2	1	0.43(4)

* B_{iso} for B1 restricted to a minimum of 0.2

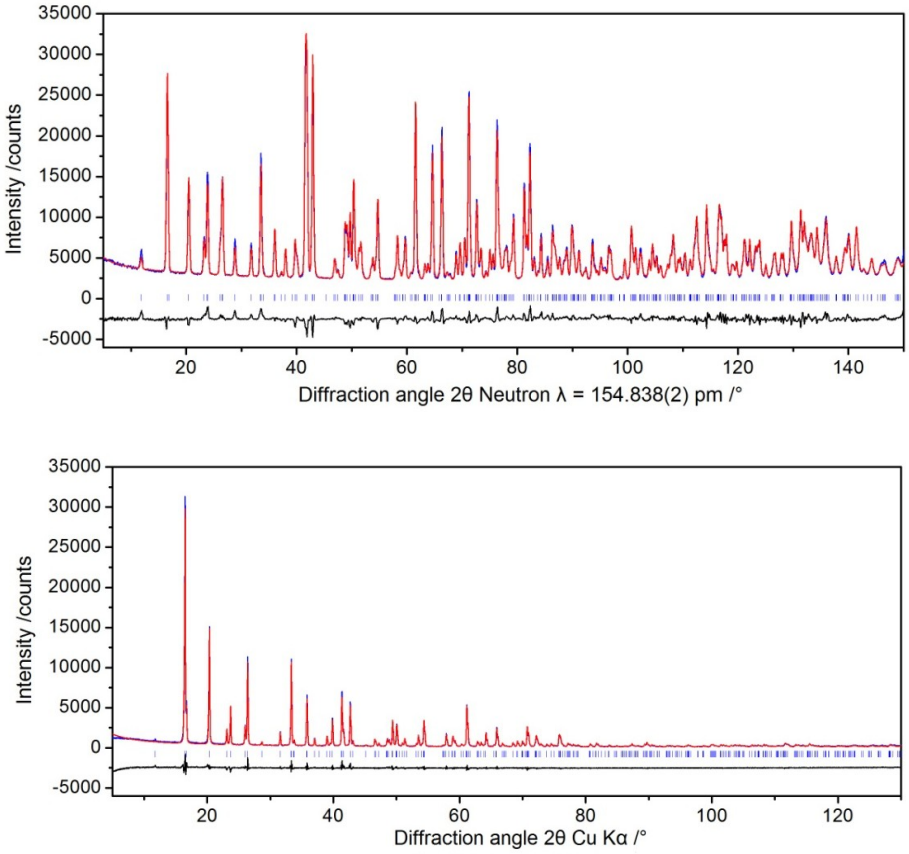

Figure 6.2. Rietveld plots of neutron powder-diffraction data (top) and X-ray powder-diffraction room-temperature data (bottom) refinement results (sample B16) using the original crystal-structure model of Garsche et al. [26]. Observed intensities (blue curve), calculated intensities (red curve), positions of reflections (tick marks) and the difference curve between observed and calculated data (lower black curve) are shown.

Using the crystal-structure model of Garsche et al. [26] plausible modifications of the model were tested: In separate refinements the occupancy of each Al site was optimized. This results in full occupancy for the Al1, Al3 and Al4 site. For the Al2 site a vacancy of 3.3(6) % was observed, while fixing the displacement factor during the refinement due to the correlation of these two values. A mixed occupancy of aluminum and boron on the Al2 site might be possible. However, a significant result cannot be obtained from the diffraction experiments. Fisch et al. [48] found vacancies of 2.1(4) % and 3.2(4) % on the Al2 site, using single crystals with an initial Al_2O_3:B_2O_3 ratio of 9:2 or 1:2, respectively. They determined a small amount of B on the Al2 position, coherent with their refined vacancy on the Al2 site [48].

Difference-Fourier neutron diffraction data calculations were performed. The highest maximum was found for B at $x = 0.71$, $y = 0.02$, $z = 0$, corresponding to the position given in the published model [26]. No new boron position could be found.

6.3.1.2 Chemical analysis

The Al/B ratio was calculated from the measured at% of the PGAA data (Tab. 6.5). None of the samples show the exact chemical composition of $Al_{20}B_4O_{36}$ or $Al_{19.64}B_{4.36}O_{36}$ (corresponding to $Al_{18}B_4O_{33}$). A decreasing Al/B ratio is determined for all synthesized samples upon increasing initial boron content. For sample B8 an impurity of a small amount of A_2B leads to a smaller Al/B ratio. A comparison of sample B10 and B15, both synthesized with an initial ratio of 1:1.1 (Al/B), show the determined Al/B ratio to be smaller for the samples synthesized by the solid-state reaction as this route combined with a higher and longer heating period causes a higher loss of boron.

Table 6.5. Calculated Al/B ratio from PGA analysis for the commercial products and synthesized samples differing in synthesis routes and initial boron content; the determined chemical formula is standardized to a unit-cell content of $Al_{20}B_4O_{36}$ and, for a better comparison to literature data, to Al_5BO_9.

Exp.	Initial	Method	PGAA mol%		calculated	calculated chem. formula	
	Al_2O_3/B_2O_3		Al	B	Al/B	$Al_{20-x}B_{4+x}O_{36}$	$Al_{5-x}B_{1+x}O_9$
B6	5.0:1.1	ND	82.2(3)	17.8(1.6)	4.63(42)	$Al_{19.73(07)}B_{4.27(38)}O_{36}$	$Al_{4.93(2)}B_{1.07(10)}O_9$
B7	4.5:1.1	ND	82.2(3)	17.9(1.6)	4.60(41)	$Al_{19.72(07)}B_{4.28(38)}O_{36}$	$Al_{4.93(2)}B_{1.07(10)}O_9$
B8	3.0:1.1	ND	79.1(4)	20.9(1.5)	3.79(43)	$Al_{19.00(10)}B_{5.00(36)}O_{36}$	$Al_{4.75(2)}B_{1.25(10)}O_9$
B10	1.0:1.1	ND	81.1(4)	18.9(1.8)	4.28(41)	$Al_{19.46(10)}B_{4.54(43)}O_{36}$	$Al_{4.86(2)}B_{1.14(11)}O_9$
B13	3.0:1.1	S	81.8(4)	18.2(1.6)	4.48(39)	$Al_{19.62(10)}B_{4.37(38)}O_{36}$	$Al_{4.91(2)}B_{1.09(10)}O_9$
B14	1.5:1.1	S	81.7(4)	18.3(1.6)	4.47(39)	$Al_{19.61(10)}B_{4.39(38)}O_{36}$	$Al_{4.90(2)}B_{1.10(10)}O_9$
B15	1.0:1.1	S	81.6(4)	18.4(1.6)	4.43(39)	$Al_{19.58(10)}B_{4.42(38)}O_{36}$	$Al_{4.89(2)}B_{1.11(10)}O_9$
Alborite	unknown		82.7(3)	17.3(1.6)	4.78(44)	$Al_{19.85(7)}B_{4.15(38)}O_{36}$	$Al_{4.96(2)}B_{1.04(10)}O_9$
Alborex	unknown		82.2(4)	17.8(1.6)	4.60(41)	$Al_{19.7(1)}B_{4.28(38)}O_{36}$	$Al_{4.93(2)}B_{1.07(10)}O_9$

ND: nitrate decomposition method; S: solid-state reaction

However, although the calculated values for the samples in both series are equal within the estimated errors the differences in the chemical compositions indicate a solid-solution series within narrow limits. Standardized to a unit-cell content of $Al_{5-x}B_{1+x}O_9$, x is determined as $0.07(11) < x < 0.14(11)$ for the synthesized samples compared with the narrow range of $0.021(6) < x < 0.038(6)$ for the composition of $Al_{5-x}B_{1+x}O_9$ reported by Fisch et al. [48].

6.3.1.3 Spectroscopy

Solid state ^{11}B and ^{27}Al MAS NMR data were acquired for samples of both synthesized series and for the commercial products (Fig. 6.3). Additional ^{27}Al MQMAS measurements were acquired for selected samples (see Fig. 6.4). The summarized measured NMR parameters are shown in Tables 6.6 and 6.7. The ^{11}B MAS NMR spectra show boron to be mainly represented by 3-fold (BO_3) coordination environments. A small amount of 1% - 3% 4-fold coordinated boron is present in all samples

independent from the synthesis route. The trigonal planar BO_3 positions were fitted by a second order broadened quadrupolar resonance representing quadrupole coupling constants (C_Q) of ~2.6 MHz with a chemical shift (δ_{iso}) of ~16.5 ppm and an asymmetry parameter (η_Q) of ~ 0.07 - 0.12. The single or multiple BO_4 positions were simulated with Gaussian line-shapes. As multiple BO_4 resonances were observed for nearly all samples the NMR data may suggest that boron does not replace aluminum on a single Al site but could be placed as BO_4 group at an interstitial position. A trend of an increasing site occupancy of 4-coordinated BO_4 is observed with increasing initial B content confirming the assumption of a solid solution within a narrow limit.

Table 6.6. ^{11}B solid state NMR parameters obtained from simulated fits for selected samples of A_9B_2/A_5B series.

#	initial composition /wt%		Fit	δ_{iso} /ppm	C_Q /MHz	η_Q	Δ (width) /KHz	species	integr. Int	Species Int.
	Al_2O_3	B_2O_3		(± 1)	(± 0.1)	(± 0.01)	(± 0.05)		/%	/%
	Alborite		1/2 QMAS	16.5	2.6	0.09	-	BO_3	98 ± 1	98 ± 1
			Gaussian	2.4	-	-	0.12	BO_4	1 ± 1	2 ± 1
			Gaussian	0.2	-	-	0.46	BO_4	1 ± 1	
	Alborex		1/2 QMAS	16.7	2.7	0.07	-	BO_3	98 ± 1	98 ± 1
			Gaussian	2.6	-	-	0.14	BO_4	2 ± 1	2 ± 1
			1/2 QMAS	16.5	2.6	0.12	-	BO_3	99 ± 1	99 ± 1
B6	82	18	Gaussian	0.2	-	-	0.19	BO_4	1 ± 1	1 ± 1
			1/2 QMAS	16.5	2.6	0.11	-	BO_3	98 ± 1	98 ± 1
B7	80.4	19.6	Gaussian	0.7	-	-	0.39	BO_4	2 ± 1	2 ± 1
			1/2 QMAS	16.6	2.6	0.09	-	BO_3	97 ± 1	97 ± 1
B10	47.6	52.4	Gaussian	2.5	-	-	0.16	BO_4	2 ± 1	3 ± 1
			Gaussian	-0.7	-	-	0.29	BO_4	1 ± 1	
			1/2 QMAS	16.3	2.6	0.09	-	BO_3	98 ± 1	98 ± 1
B11	82	18	Gaussian	2.3	-	-	0.20	BO_4	1 ± 1	2 ± 1
			Gaussian	0.3	-	-	0.20	BO_4	1 ± 1	
			1/2 QMAS	16.3	2.6	0.09	-	BO_3	98 ± 1	98 ± 1
B12	80.4	19.6	Gaussian	2.3	-	-	0.22	BO_4	1 ± 1	2 ± 1
			Gaussian	0.0	-	-	0.25	BO_4	1 ± 1	
			1/2 QMAS	16.4	2.6	0.09	-	BO_3	97 ± 1	97 ± 1
B14	57.7	42.3	Gaussian	2.3	-	-	0.19	BO_4	2 ± 1	3 ± 1
			Gaussian	-0.3	-	-	0.21	BO_4	1 ± 1	

δ_{iso} = chemical shift, C_Q = quadrupole coupling constants, η_Q = asymmetry parameter

Table 6.7. ^{27}Al solid state NMR parameters obtained from simulated fits for selected samples of A_9B_2/A_5B series.

#	initial composition /wt%		fit	δ_{iso} /ppm	C_Q /MHz	η_Q	Δ (width) /KHz	species	integrated intensity /%	
	Al_2O_3	B_2O_3		(± 1)	(± 0.1)	(± 0.01)	(± 0.05)			(without Al_2O_3)
	Alborite		1/2 QMAS	72	9.2	0.45	-	AlO_4	24 ± 1	24 ± 1
			1/2 QMAS	52	6.8	0.04	-	AlO_5	18 ± 1	18 ± 1
			1/2 QMAS	45	8.0	0.75	-	AlO_5	16 ± 1	16 ± 1
			Gaussian	10	-	-	0.46	AlO_6	1 ± 1	1 ± 1
			1/2 QMAS	9	5.8	0.30	-	AlO_6	42 ± 1	42 ± 1
	Alborex		1/2 QMAS	72	9.3	0.38	-	AlO_4	18 ± 1	18 ± 1
			1/2 QMAS	52	6.8	0.05	-	AlO_5	20 ± 1	20 ± 1
			1/2 QMAS	44	7.9	0.63	-	AlO_5	20 ± 1	20 ± 1
			Gaussian	10	-	-	0.40	AlO_6	2 ± 1	2 ± 1
			1/2 QMAS	9	5.8	0.37	-	AlO_6	42 ± 1	42 ± 1
B6	82	18	1/2 QMAS	73	9.5	0.45	-	AlO_4	30 ± 1	30 ± 1
			1/2 QMAS	52	6.9	0.06	-	AlO_5	14 ± 1	14 ± 1
			1/2 QMAS	47	8.3	0.80	-	AlO_5	12 ± 1	12 ± 1
			1/2 QMAS	9	5.8	0.06	-	AlO_6	44 ± 1	44 ± 1
B7	80.4	19.6	1/2 QMAS	72	9.3	0.43	-	AlO_4	28 ± 1	28 ± 1
			1/2 QMAS	52	6.8	0.06	-	AlO_5	14 ± 1	14 ± 1
			1/2 QMAS	52	9.0	0.81	-	AlO_5	18 ± 1	18 ± 1
			1/2 QMAS	9	5.9	0.30	-	AlO_6	40 ± 1	40 ± 1
B10	47.6	52.4	1/2 QMAS	72	9.2	0.44	-	AlO_4	23 ± 1	23 ± 1
			1/2 QMAS	52	6.8	0.08	-	AlO_5	20 ± 1	20 ± 1
			1/2 QMAS	45	8.0	0.77	-	AlO_5	18 ± 1	18 ± 1
			Gaussian	10	-	-	0.20	AlO_6	1 ± 1	1 ± 1
			1/2 QMAS	9	5.8	0.36	-	AlO_6	39 ± 1	39 ± 1
B11	82	18	1/2 QMAS	71	9.1	0.45	-	AlO_4	20 ± 1	23 ± 1
			1/2 QMAS	52	6.8	0.00	-	AlO_5	19 ± 1	22 ± 1
			1/2 QMAS	44	7.8	0.75	-	AlO_5	14 ± 1	16 ± 1
			1/2 QMAS	9	5.8	0.38	-	AlO_6	33 ± 1	39 ± 1
			Gaussian	14	-	-	6.13	Al_2O_3	14 ± 1	-
B12	80.4	19.6	1/2 QMAS	72	9.1	0.44	-	AlO_4	21 ± 1	23 ± 1
			1/2 QMAS	52	6.8	0.04	-	AlO_5	20 ± 1	21 ± 1
			1/2 QMAS	45	8.0	0.76	-	AlO_5	16 ± 1	17 ± 1
			Gaussian	10	-	-	0.32	AlO_6	1 ± 1	1 ± 1
			1/2 QMAS	9	5.9	0.38	-	AlO_6	36 ± 1	39 ± 1
			Gaussian	13	-	-	1.16	Al_2O_3	7 ± 1	-
B14	57.7	42.3	1/2 QMAS	71	9.1	0.44	-	AlO_4	22 ± 1	22 ± 1
			1/2 QMAS	52	6.8	0.04	-	AlO_5	20 ± 1	20 ± 1
			1/2 QMAS	45	8.0	0.76	-	AlO_5	18 ± 1	18 ± 1
			Gaussian	10	-	-	0.20	AlO_6	1 ± 1	1 ± 1
			1/2 QMAS	9	5.9	0.37	-	AlO_6	40 ± 1	40 ± 1

δ_{iso} = chemical shift, C_Q = quadrupole coupling constants, η_Q = asymmetry parameter

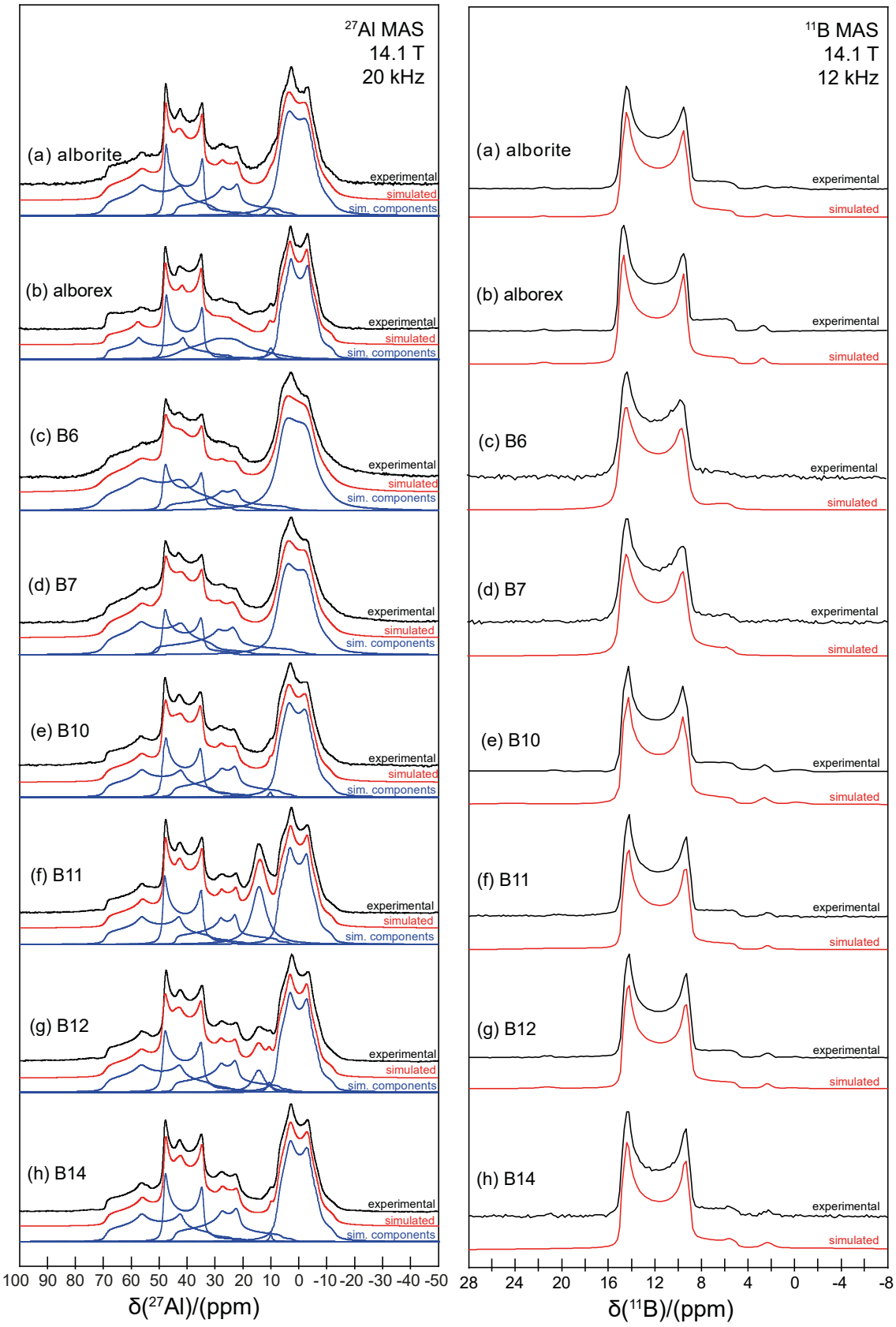

Figure 6.3. Experimental ^{27}Al MAS NMR (left) spectra and ^{11}B MAS NMR (right) spectra for A_9B_2/A_5B series, displayed with the simulations of the corresponding spectra and the simulated components.

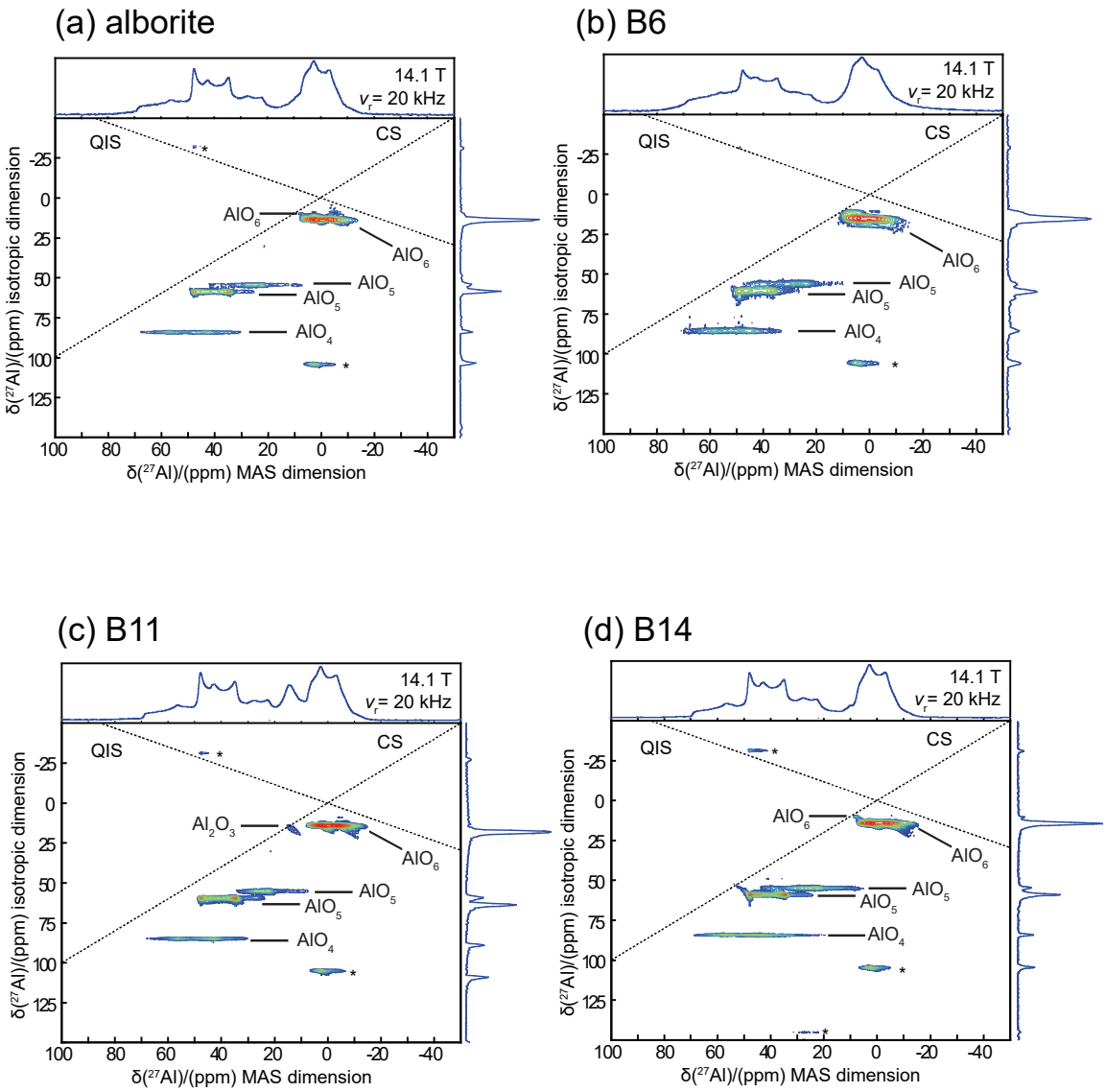

Figure 6.4. Experimental ^{27}Al MQMAS NMR data for the commercial product Alborite and for synthesized samples, using the nitrate decomposition method or the solid state reaction, respectively.

The ^{27}Al MAS NMR spectra show Al to be present in three different coordination environments, AlO_4, AlO_5 and AlO_6, in which AlO_5 resides on two different sites. The same resonances were also observed by Fisch et al. [48]. An additional weak extra peak is observed representing a second AlO_6 site correlating with the formation of 4-fold coordinated boron. Sample B6 and B7 show a broadening of the line shapes in the ^{27}Al MAS NMR spectra and a varying ratio of AlO_4/AlO_5 compared to the remaining samples. This might be explained by disorder effects in the crystal structure, as also expected from the X-ray diffraction pattern of these two samples (see part X-ray powder diffraction).

FTIR and Raman spectra are collected for samples of the A_9B_2/A_5B series. The spectra are almost identical within the A_9B_2/A_5B series, therefore IR and Raman spectra of one selected sample of the A_9B_2/A_5B (B10) series are shown in comparison to those of a sample from the A_2B series (A4) containing both BO_3- and BO_4 – groups (Fig. 6.5). According to Fisch et al. [48] the characteristic asymmetric stretching vibrations of a BO_3 group occur predominantly in IR spectra (1200 – 1450 cm^{-1}) whereas the symmetric stretching vibrations occur predominantly in Raman spectra (950 – 1050 cm^{-1}). These modes are observed in the spectra for the samples of both series, A_2B and A_9B_2/A_5B (Fig. 6.5).

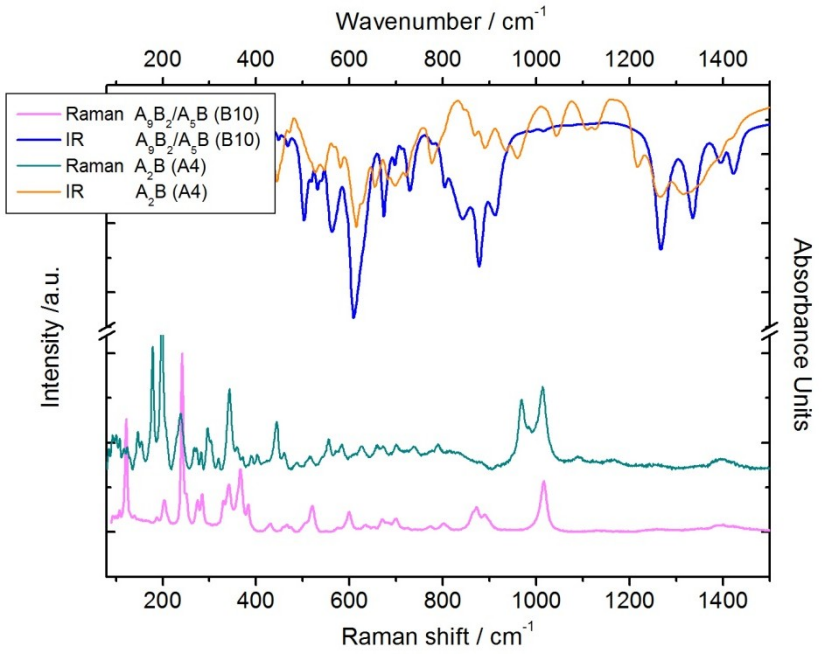

Figure 6.5. IR (top) and Raman (bottom) spectra of representative samples of the A_9B_2/A_5B and A_2B series, respectively. IR spectrum of A_2B is double raised pictured.

A second strong mode in the Raman spectra of sample A4 (A_2B) to the left of the BO_3 band can be assigned to BO_4 [48]. Alike the finding of Fisch et al. [48] for an aluminum borate sample with A_9B_2/A_5B structure this band does not occur in the spectra for the sample B10 (A_9B_2/A_5B). However, the asymmetric Raman peak shape of the absorption band at 1016 cm^{-1} (sample B10) might indicate both, BO_3 and BO_4 (Fig. 6.6). As observed by Fisch et al. [48], the IR-active asymmetric stretching vibrations of BO_4 expected at 950 – 1200 cm^{-1} [48] are only verified for the A_2B sample A4.

The bending symmetric vibrations of BO_3 was determined by Griesser et al. [28] for boron-doped mullites and $Al_{18}B_4O_{33}$ to occur in the spectral region of 674 – 689 cm^{-1} and the bending asymmetric vibration of BO_3 in the spectral region of 555 – 562 cm^{-1}. Distinction between B-O and Al-O

stretching in this region is difficult as the frequency of the AlO_x polyhedral features are also expected in the region < 900 cm^{-1} [48].

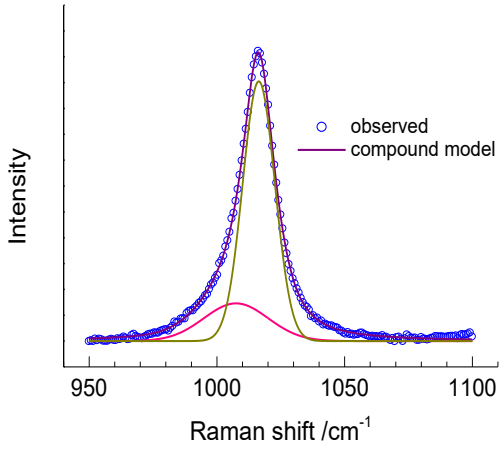

Figure 6.6. Selective region of Raman spectra of a representative sample of the A_9B_2/A_5B series (B10), showing the characteristic peak of the BO_3 group at about 1016 cm^{-1}; the asymmetric peak shape indicates the presence of a BO_4 group fitted at about 1007 cm^{-1}.

6.3.2 Thermal stability of $Al_{20-x}B_{4+x}O_{36}$

The thermal stability was investigated by DTA for selected samples. The TG indicates a minor weight loss between room temperature and 1773 K, more pronounced in the HT-region above 1473 K. In additional experiments a continuous weight loss is observed within a 5 h isothermal segment at 1673 K (Tab. 6.8). In the resulting products significant amounts of α-Al_2O_3 were additionally found indicating the weight loss to be caused by loss of boron. For samples synthesized using the nitrate decomposition method, an almost identical weight loss is observed upon heating in the isothermal segment. This, together with an increasing amount of Al_2O_3 in the products with decreasing initial boron content, indicates differences in the chemical composition.

Assuming a composition of Al/B = 5:1.1, the expected amount of α-Al_2O_3 would be about 17 wt% for a weight loss of 3.6 wt%. The determined amount of 24 wt% α-Al_2O_3 for a sample with this initial composition (B11) is clearly higher than the calculated one. This might be explained by boron which volatized during the heating to 1673 K. The DSC measurements do not show any signal, since a continuous weight loss over a period of time as observed here. An extended heating experiment was performed on a selected sample (B10) at 1673 K using a covered corundum crucible (heating/cooling rate: 5 K/min), yielding pure α-Al_2O_3 [104] as decomposition product after a heating period of 48h. The experiments confirm the decomposition temperature observed by Scholze [13]. A decomposition of the alumina borate phase at 1473 K might be expected for an extended heating period (about 16.73 wt% α-Al_2O_3 after 44h) supporting the study of Rymon-Lipinski et al. [49] describing a

decomposition of A_9B_2 at 1473 K to Al_2O_3 and liquid B_2O_3. The thermal analysis clearly suggests that the phase diagram [43] may need to be re-evaluated.

Table 6.8. Weight loss within the 5h isothermal segment at 1673 K and the amount of α-Al_2O_3 in the resulting products; small variations of the weight (± 0.3 wt%) in the heating segment up to 1473 K are caused by the instrument and /or surface water.

Exp.	Initial Al_2O_3/B_2O_3	Method	Weight loss /wt% Isothermal segment	Content of α-Al_2O_3 /wt%
B6	5.0:1.1	ND	3.5	24
B7	4.5:1.1	ND	3.8	22
B10	1.0:1.1	ND	3.5	17
B12	4.5:1.1	S	2.6	
B14	1.5:1.1	S	2.0	14
B15	1.0:1.1	S	2.0	14
Alborite	unknown		3.5	29
Alborex	unknown		2.8	18

ND: nitrate decomposition method; S: solid-state reaction

6.3.3 Crystal-chemical characterization of $Al_4B_2O_9$

6.3.3.1 Diffraction

X-ray diffraction patterns are collected for all samples synthesized with different initial Al/B ratios confirming pure phases. The lattice parameters and the average crystallite size were refined using a Pawley fit. A slight trend of a decreasing cell volume is observed for increasing initial boron content (Tab. 6.9). These minor variations might be caused by small structural differences (see part spectroscopy). As observed for the A_9B_2/A_5B series the crystallite size increases with increasing initial boron content. No amorphous boron oxide compounds are expected to be in any sample, as repeated measurements after two years, keeping the sample in open conditions, do not show impurities of boric acid.

Table 6.9. Refined lattice parameters and crystallite sizes for the samples of the A_2B series.

Exp.	Al_2O_3 /wt%	B_2O_3 /wt%	Lattice parameter a / pm	Lattice parameter b / pm	Lattice parameter c / pm	Lattice parameter β /°	Cell volume V / 10^6 pm^3	Crystallite size / nm
A1	70	30	1481.8(2)	554.44(6)	1509.5(2)	90.752(4)	1240.1(3)	37.3(4)
A2	65	35	1481.8(4)	554.6(1)	1508.3(3)	90.775(6)	1239.4(5)	36.9(4)
A3	60	40	1481.8(2)	554.54(4)	1507.1(1)	90.831(3)	1238.2(2)	74.7(9)
A4	35	65	1481.3(1)	554.18(3)	1505.93(9)	90.930(2)	1236.1(1)	135(2)

Rietveld refinements on neutron diffraction data were performed on sample A5 (Figure 6.7). Using the crystal-structure model of Fischer et al. [25], the lattice parameters and all structural parameters were refined. The isotropic displacement parameters were constrained to be equal within a group of elements, respectively. The refinement confirms the basic structure determined from X-ray powder diffraction [25]. A very short distance of 212(5) pm is refined for the O10 - O10 distance. However, the disorder of the oxygen atoms has a stronger impact on neutron diffraction data compared to X-ray powder diffraction data due to the difference in the scattering length more pronounced in neutron data.

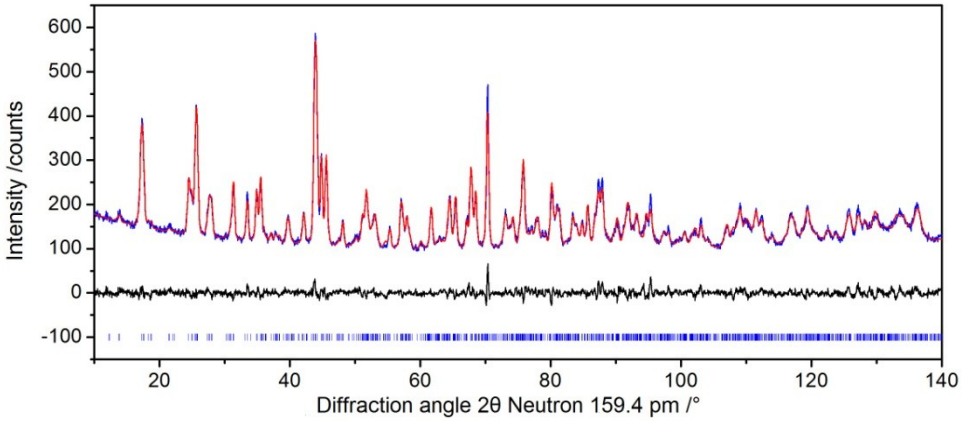

Figure 6.7. Rietveld plot of the refined neutron powder diffraction data at RT, using the original crystal-structure model of [25]. Observed intensities (blue curve), calculated intensities (red curve), positions of reflections (tick marks) and the difference curve between observed and calculated data (lower black curve) are shown.

To investigate the oxygen disorder different models were tested: (i) the occupancies of the channel oxygen atoms O10 and O5 were refined constrained to be 1, showing a preference for the O10 site (Occ(O10) = 0.61(3); Occ(O5) = 0.39(3)); (ii) vacancies were refined on the O10 site removing the O5 site, resulting in a decreased occupancy of 0.78(2) for the O10 site. Both models indicate the existence of both atoms O5 and O10. Difference-Fourier calculations were performed using the neutron-diffraction refinement. The isotropic displacement parameters were kept from the model [25], as no reasonable refinement of these values could be achieved. Highest maximum corresponds to the B2 position ($x = 0.37$, $y = 0.00$, $z = 0.13$) followed by maxima which could be assigned to the remaining three boron atoms and a 5th maximum ($x = 0.37$, $y = 0.50$, $z = 0.13$) shifted by 0.5 in **b** direction compared to the B2 position. The following maximum ($x = 0.28$, $y = 0.50$, $z = 0.26$) is close to the O1 site determined by Fischer et al. [25].

As additional approach, transmission electron microscope (TEM) was applied to investigate the crystal structure of sample A4. Three-dimensional electron diffraction data were collected from single crystals by automated diffraction tomography (ADT) [105]. The 3D data reconstruction confirm the

monoclinic unit cell in space group *C2/m* with a = 1488 pm, b = 553 pm, c =1502 pm and β = 90.6° (Fig. 6.8). The structure solution for ordered crystals clearly shows one fully occupied position of O10 but no significant signal for the second postulated oxygen O5 in the channel. The diffraction data showed diffuse scattering along **b** direction in some crystals, which was assigned to a superstructure with a threefold **b**-axis and additional disorder within the **ac** plane. Theses domains might have a disordered distribution of O5 and O10. It is likely that domains with a disordered superstructure occur independent from the initial composition. This explains why a satisfactory refinement with an average structure model from powder diffraction refinements cannot be obtained.

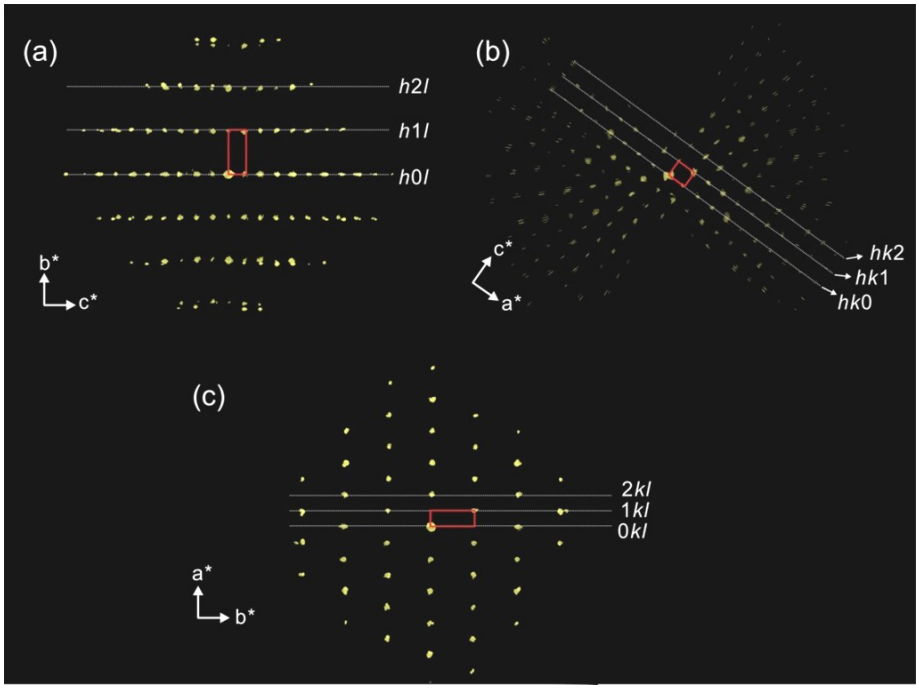

Figure 6.8. Projections of 3D reciprocal space of $Al_4B_2O_9$ along the mains directions.

The determined atomic parameters of sample A4 are listed in Table 6.10; a projection of the crystal structure is shown in Figure 6.9. The mean distances of the B-O groups in the range of 131 pm - 141 pm confirm the B1, B3 and B4 atoms to occur in a nearly planar trigonal coordination. Full occupancy of the O10 site causes the B2 to be exclusively 4-fold coordinated (B2 - O13: 141 pm, B2 - O10: 141 pm, 2x B2 - O7: 143 pm). Fischer et al. [25] discussed their model with a short O10 - O7 distance (212 pm) in the $Al3O_4$ tetrahedron. The electron-diffraction data yield an interatomic distance of 234 pm for O10 - O7 in the $Al3O_5$ polyhedron along with a short distance of 225 pm for O10 - O10 and 223 pm for O10 - O13. In a regular tetrahedron an O - O distance of 241 pm would be expected for a B-O distance of 148 pm. However, for borasilite [37], being closely related to the $Al_4B_2O_9$ structure, a similar interatomic distance (225 pm) is observed for O10 - O10 in the $Al3O_5$ group. The Al3 will be exclusively 5-fold coordinated in case of a fully occupied O10 site.

Table 6.10. Crystallographic data of A_2B obtained from electron diffraction data, representing the domains with an ordered distribution of atoms, without the channel oxygen atom O5.

Atom	multiplicity	Wyckoff	*x*	*y*	*z*	Occu.	B_{iso} /10^4 pm^2
Al1	4	*i*	0.86269	0	0.33514	1	1.38411
Al2	4	*i*	0.80938	0	0.15559	1	2.27869
Al3	4	*i*	0.57318	0	0.07289	1	2.63874
Al4	4	*i*	0.66990	0	0.34258	1	2.39318
Al5	8	*j*	0.00069	0.74111	0.24249	1	0.81089
Al6	4	*e*	0.25	0.25	0	1	1.85628
Al7	4	*f*	0.25	0.25	0.5	1	2.32765
B1	4	*i*	0.10293	0	0.10782	1	0.79983
B2	4	*i*	0.37622	0	0.11439	1	3.32961
B3	4	*i*	0.12523	0	0.37076	1	2.85666
B4	4	*i*	0.38743	0	0.38802	1	1.69678
O1	4	*i*	0.76180	0	0.26698	1	2.59689
O2	4	*i*	0.78732	0	0.43378	1	2.91272
O3	4	*i*	0.91799	0	0.22331	1	2.41924
O4	8	*j*	0.92190	0.7121	0.35597	1	1.67467
O6	4	*i*	0.31902	0	0.45069	1	0.80536
O7	8	*j*	0.81834	0.70493	0.10413	1	1.83733
O8	4	*i*	0.69647	0	0.05781	1	1.70942
O9	8	*j*	0.06788	0.77736	0.13666	1	1.72679
O10	4	*i*	0.44314	0	0.04850	1	2.73743
O11	8	*j*	0.66112	0.28222	0.40465	1	2.47135
O12	4	*i*	0.57464	0	0.27627	1	1.53966
O13	4	*i*	0.42554	0	0.19502	1	1.15198
O14	4	*i*	0.06913	0	0.30225	1	1.42201
O15	4	*i*	0.83409	0	0.96146	1	1.78758

Peacor et al. [37] described the O10 position in boralsilite to be disordered introducing a ‘split’ atom pair consisting of O10A (x = 0.444, y = 0, z = 0.049) and O10B (x = 1/2, y = 0, z = 0); the latter one residing in an inversion center. Both oxygen atoms (O10A and O10B) are in the coordination sphere of the Al3 ($Al3O_5$ polyhedron), but too close for a simultaneous occupancy. A shift of the O10B by 0.5 in **b** direction causes a shortened Al-O distance of 146.4(4) pm in the $Al3O_5$ [37], thus leading to the assumption that a substitution of B^{3+} for Al^{3+} on the Al3 site might be possible. The fifth maximum found in the Fourier calculations ($x = 0.37$, $y = 0.50$, $z = 0.13$) might be a result from a disordered configuration. However, structural details discussing different models of disorder configurations are given in Zhao et al. [106].

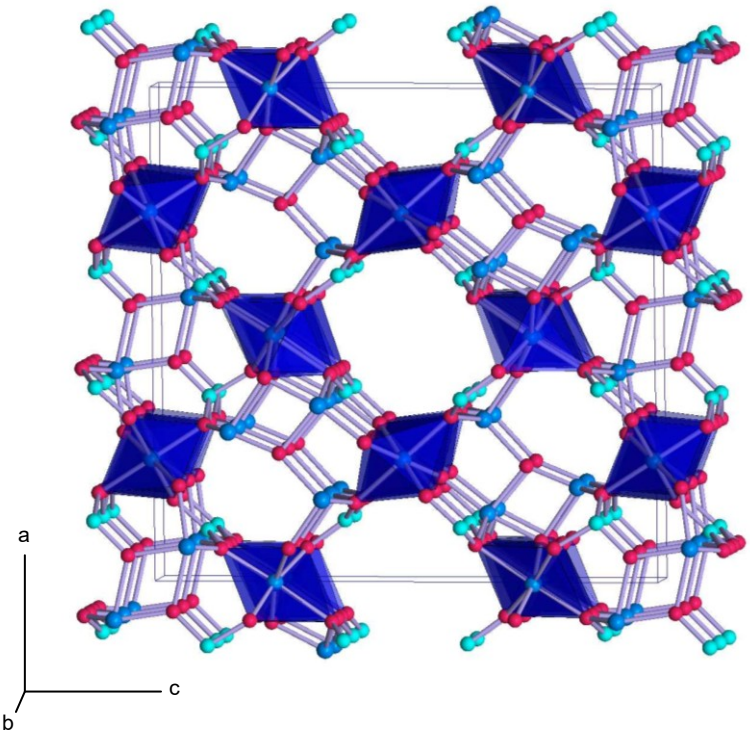

Figure 6.9. Crystal structure of mullite-type aluminoborates. Blue polyhdedra: AlO_6-octahedra, light blue dots: Al (in AlO_4- or AlO_5-polyhedra), green dots: B (in BO_3- or BO_4-polyhedra).

6.3.3.2 Spectroscopy

The ^{11}B MAS NMR data (Fig. 6.10, left) confirm boron to be present in trigonal (site B1, B3, B4) and different tetrahedral sites (site B2 and possibly B3). The trigonal planar BO_3 position was fitted by a second order broadened quadrupolar resonance with C_Q of ~ 2.6 MHz, δ_{iso} of ~ 16.8 ppm and η_Q of ~ 0.11. However, the different BO_3 sites might be too similar to be distinguished in the NMR spectra. The BO_4 positions were simulated with Gaussian line-shapes. Similar to the A_9B_2/A_5B series a trend of slightly increasing relative ratios of the site occupancy of 4-coordinated BO_4 (26 - 30 % BO_4) compared to the BO_3 site is estimated with an increasing boron content in the precursor phase (see Tab. 6.11). Fischer et al. [25] determined about 20 % of boron in the A_2B structure to be tetrahedrally coordinated. However, in the published model of the A_2B structure the statistical distribution of the O10 atoms leads to a statistical distribution of the B2 atom on either trigonal or tetrahedral sites [25]. A full occupancy of the O10 position would cause the B2 atom to be exclusively 4-fold coordinated and therefore would yield an increased ratio of BO_4 up to 25 %. An additional slightly increased BO_4 content and small changes in the BO_3/BO_4 ratio might be explained by the slight structural changes rather than by differences in the chemical composition. Multiple BO_4 peaks can be explained due to the disorder in these systems, which may also cause the B3 atom to occur in 4-fold coordination in the case of a disordered configuration of O5 and O10.

Table 6.11. ^{11}B solid state NMR parameters obtained from simulated fits samples of A_2B series.

#	initial composition /wt%		fit	δ_{iso} /ppm	C_Q /MHz	η_Q	Δ (width) /KHz	species	integrated intensity /%	species total intensity /%
	Al_2O_3	B_2O_3		(± 1)	(± 0.1)	(± 0.01)	(± 0.1)			
A1	70	30	1/2 QMAS	16.8	2.6	0.11	-	BO_3	74 ± 1	74 ± 1
			Gaussian	0.5	-	-	0.72	BO_4	3 ± 1	
			Gaussian	-0.9	-	-	0.16	BO_4	13 ± 1	26 ± 1
			Gaussian	-1.3	-	-	0.09	BO_4	10 ± 1	
A2	65	35	1/2 QMAS	16.8	2.6	0.11	-	BO_3	72 ± 1	72 ± 1
			Gaussian	1.0	-	-	0.70	BO_4	3 ± 1	
			Gaussian	-0.9	-	-	0.17	BO_4	14 ± 1	28 ± 1
			Gaussian	-1.3	-	-	0.10	BO_4	11 ± 1	
A3	60	40	1/2 QMAS	16.8	2.6	0.11	-	BO_3	71 ± 1	71 ± 1
			Gaussian	-0.7	-	-	0.55	BO_4	4 ± 1	
			Gaussian	-1.1	-	-	0.15	BO_4	9 ± 1	29 ± 1
			Gaussian	-1.3	-	-	0.10	BO_4	16 ± 1	
A4	35	65	1/2 QMAS	16.8	2.6	0.11	-	BO_3	70 ± 1	70 ± 1
			Gaussian	-0.1	-	-	0.23	BO_4	2 ± 1	
			Gaussian	-1.0	-	-	0.12	BO_4	8 ± 1	30 ± 1
			Gaussian	-1.2	-	-	0.09	BO_4	20 ± 1	

δ_{iso} = chemical shift, C_Q = quadrupole coupling constants, η_Q = asymmetry parameter

The ^{27}Al MAS NMR and ^{27}Al MQMAS NMR spectra for sample A1 and A4 are shown in Figure 6.10, right. The simulation of the ^{27}Al MAS NMR data was performed analogously to [92]: the contours present in the 2D ^{27}Al MQMAS data and the long asymmetric tails (to higher field) of all of 1D ^{27}Al MAS NMR resonances indicate that significant distributions of quadrupolar and chemical shift parameters exist, thus implying that significant short range disorder characterizes these systems. The QuadFit program was used as it permits a distribution of quadrupolar parameters to be introduced to the modelling of the ^{27}Al MAS NMR resonances [52]. The deconvolutions of the 1D ^{27}Al MAS NMR data at two fields (9.40 T and 14.1 T) were simulated using Gaussian distributions of the quadrupolar coupling constant (C_Q) to accurately represent the disordered quadrupolar lineshapes observed. The deconvolutions were additionally constrained by simulating the MQMAS projections of each site and therefore invoke an accurate simulation of each spectrum for the samples analyzed with this methodology. The corresponding fit parameters are given in Table 6.12.

An increasing disorder is observed as compared to the A_9B_2/A_5B related samples. Six independent Al sites can be distinguished in different coordination environments: one 4-fold coordinated site (AlO_4), three 5-fold coordinated sites (AlO_5) and two 6-fold coordinated sites (AlO_6). The latter one can be better described with three separate species as determined from the diffraction experiments; however, this could not be resolved exactly from the NMR spectra. The determined intensity ratio of tetrahedra / octahedra is about 50:50, similar to our previous determination for a sample of A_2B

structure [25]. However, these data give an improvement on the previously published material [25] as we can clearly distinguish the four non-octahedral resonances. The determined ratio of the different Al sites is nearly independent from the initial composition.

Table 6.12. ^{27}Al solid state NMR parameters obtained from simulated fits for samples of A_2B series.

#	δ_{iso} /ppm (± 1)	C_Q centre /MHz (± 0.1)	C_Q width /MHz (± 0.1)	η_Q (± 0.01)	broadening /KHz (± 0.1)	species	integrated intensity /%	species total intensity /%
	7	10.1	2.0	0.4	1.6	AlO_6	34 ± 1	48 ± 3
	11	5.6	4.5	1.0	0.9	AlO_6	14 ± 2	
A1	34	4.9	3.3	1.0	0.7	AlO_5	15 ± 1	
	42	4.0	1.4	0.5	0.7	AlO_5	11 ± 1	42 ± 3
	49	6.9	1.1	0.0	1.5	AlO_5	16 ± 1	
	71	8.0	4.9	1.0	2.8	AlO_4	10 ± 1	10 ± 1
	6	10.1	2.0	0.4	1.6	AlO_6	36 ± 1	47 ± 3
	11	5.6	4.5	1.0	0.9	AlO_6	11 ± 2	
A4	34	4.9	3.3	1.0	0.6	AlO_5	16 ± 2	
	42	4.0	1.4	0.5	0.8	AlO_5	16 ± 1	45 ± 5
	49	7.1	0.8	0.0	1.0	AlO_5	13 ± 3	
	77	8.0	4.9	1.0	2.8	AlO_4	9 ± 2	9 ± 2

δ_{iso} = chemical shift, C_Q = quadrupole coupling constants, η_Q = asymmetry parameter

As seen in the diffraction experiments the Al1 position is refined to be 5-fold coordinated, as well as the Al3 site in case of a fully occupied O10 site. Both are associated to AlO_5 species in the NMR data. The third AlO_5 species and the AlO_4 species show a larger quadrupole interaction compared to the other non octahedral sites (see Tab. 6.12). Therefore it is likely that they are associated to the Al2 and Al4 sites both refined to be 4-fold coordinated with an additional longer bond to the atoms O8 (Al2) or O2 (Al4). As they show a similar geometry, they may not be clearly distinguishable in the NMR. Two octahedrally coordinated sites are determined with a site occupancy of about 35 % and 12 %, which agrees well with our previous studies [25]. Fischer et al. [25] assigned the more populated Al site to a combination of Al5 and Al7 as these two sites show a larger distortion index (DI) correlating with a larger quadrupole interaction in the NMR data. This is confirmed by the model obtained from the electron-diffraction experiment showing the distortion of the octahedra Al6 (DI(OMO) = 0.039) to be slightly smaller than those of the octahedra Al5 and Al7, representing a distortion of DI(OMO) = 0.054 for the $Al5O_6$ and of 0.066 for the $Al7O_6$ (the DI:(OMO) is calculated after [107]), correlating well with the quadrupole interaction in the NMR as shown in Table 6.12.

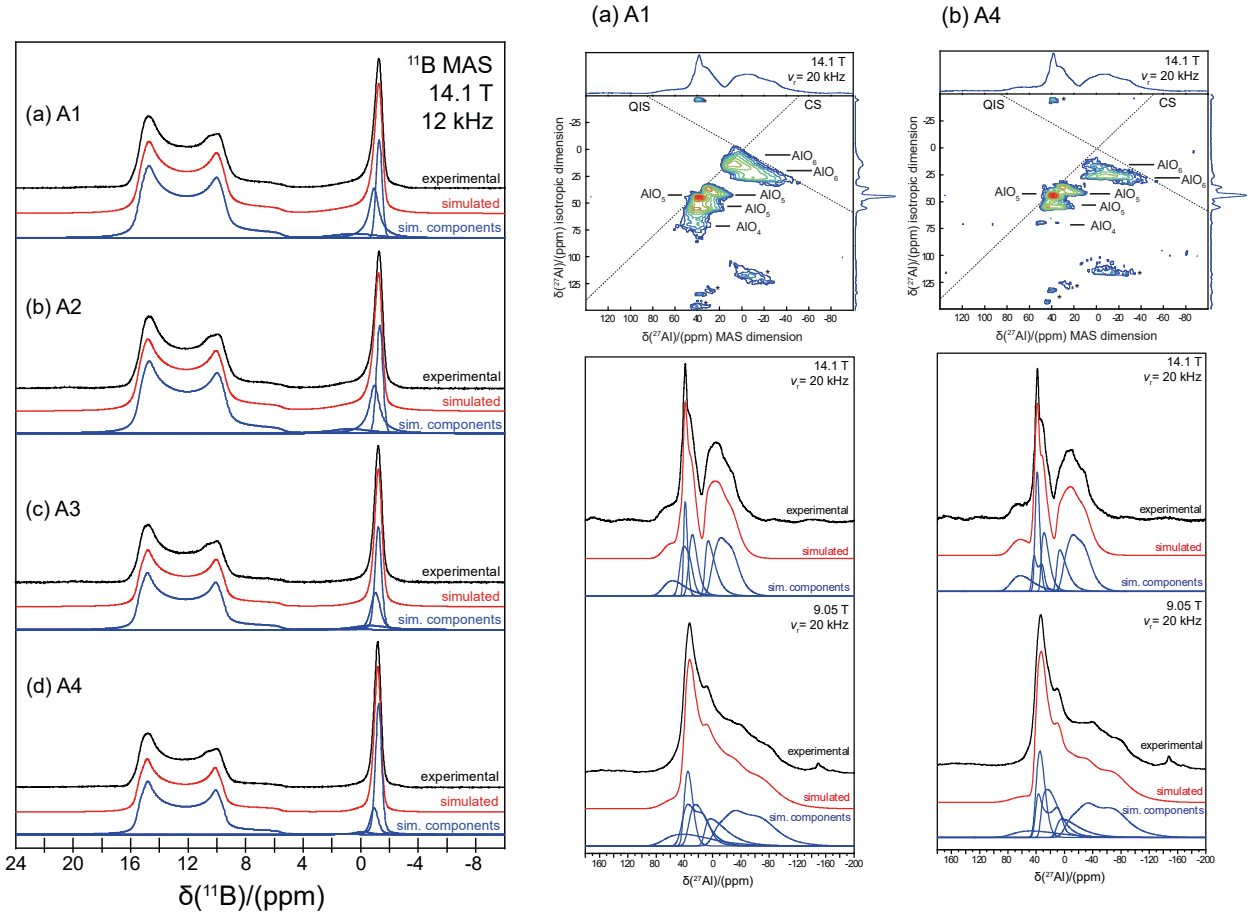

Figure 6.10. left: Experimental ^{11}B MAS NMR spectra for A_2B series at 14.1 T (black lines) displayed with the simulations of the corresponding spectra (red lines) and the simulated components (blue lines); right: ^{27}Al MQMAS NMR data (top) and ^{27}Al MAS NMR spectra and deconvolutions at 14.1 T and 9.40 T (bottom) for selected samples with an initial Al content of (a) 70 wt% Al_2O_3 and (b) 35 wt% Al_2O_3.

FTIR and Raman spectra are collected for all samples of the A_2B series. The spectra of one representative sample (A4) are shown in Figure 6.5, the corresponding spectra of the samples A1 - A3 look almost identical without significant changes. Broad absorption modes are observed at about 3400 cm^{-1} in the samples A1 and A2 which can be assigned to OH groups at the surface. A further discussion of the B-O and Al-O modes is given in chapter 3.1 (part spectroscopy).

6.3.3.3 Density-functional theory calculations

A comparison of the DFT energies reveals that the model in which O10 is fully occupied is energetically more favorable compared with the model with a 50 % occupation of both O5 and O10, with a difference in total energy of 42 kJ/mol (per $Al_4B_2O_9$ formula unit). In the structure without O5 atoms the atoms B3 and Al1 remain close to their initial positions in the DFT optimization. In contrast, the presence of O5 in the channels leads to a shift of these atoms towards the channel interior leading

to a change in coordination to a tetrahedral environment. Therefore, the amount of tetrahedrally coordinated boron/aluminum would be increased at the expense of trigonally coordinated boron and fivefold-coordinated aluminum if O5 is occupied.

6.4 Conclusions

The Al-rich aluminum borate compounds were synthesized using two different synthesis routes and different initial Al/B ratios. All samples show the aluminum borate phase together with different amounts of impurity phase (Al_2O_3 or A_2B) if present. Chemical analysis clearly shows a trend in the Al/B ratio instead of a fixed chemical composition, thus, indicating the solid solution occurs within a narrow limit. Based on the results of PGAA and NMR spectroscopy, the substitution of Al by B is assumed to be in the range of about 1 – 3 %. This is supported by the powder diffraction data, confirming 3.3(6)% vacancies on the Al2 site. The NMR data show a small amount of boron to be present in fourfold coordination; this content of BO_4 is below the detection limit of the IR spectra. A correlation of BO_4 and a second AlO_6 site is observed in the NMR data. Therefore, it might be likely that BO_4 units are located in the surrounding of AlO_6 octahedra. This would induce a distortion of the octahedra, what in turn might be assigned to the additional AlO_6 site as observed in the ^{27}Al MAS NMR data. Such distortion of the octahedra caused by small BO_x units was also observed for the $Al_{6-x}B_xO_9$ phases [92]. However, a new boron position cannot be found, as this is certainly prevented by the small amount of substitution. Disorder effects are assumed for samples synthesized from sol-gel precursors with a high amount of initial alumina, confirmed by the ^{27}Al NMR data, representing a significant difference in the AlO_4/AlO_5 ratio for these samples. Thermal analysis indicates an incongruent melting for the Al-rich aluminum borate phase. Decomposition is observed to start between 1473-1673 K. Continuing thermal treatment at 1673 K leads to a complete decomposition.

The crystal structure of $Al_4B_2O_9$ was re-investigated. It was shown by electron diffraction that structural details vary among different crystals and even inside a crystallite. Predominant are domains with an ordered distribution of atoms, clearly showing that there is no significant signal for the second postulated oxygen O5 in the channel, and other domains with a probable disordered configuration of O5 and O10 as indicated by diffuse scattering. This explains that the X-ray and neutron diffraction experiments yielded disordered oxygen positions representing an average structure over all unit cells and domains. A comparison of the DFT energies reveals that the model in which O10 is fully occupied is energetically more favored over the model with a 50% occupation of both O5 and O10. The ^{11}B NMR data show about ¼ of the boron atoms to be tetrahedrally coordinated, thus correlating well with a fully occupied O10 position. A trend of a slightly increasing BO_4 content is observed for increasing initial boron content.

Acknowledgements

We gratefully thank the Deutsche Forschungsgemeinschaft (DFG) for the financial support of the projects **GE1981/5-1** and **FI442/19-1**, as well as the financial support provided by FRM II to perform neutron scattering experiments at the Forschungsneutronenquelle Heinz Maier-Leibnitz Zentrum (MLZ), Garching, Germany. TMG thanks the DFG for support in the Heisenberg program GE1981/3-1 and GE1981/3-2. JVH thanks the EPSRC, the University of Warwick and the Birmingham Science City Program for partial funding of the solid state NMR infrastructure at Warwick. The latter program accessed the Birmingham Science City Advanced Materials Project 1: Creating and Characterizing Next Generation Advanced Materials, which derived support from Advantage West Midlands (AWM) and the European Regional Development Fund (ERDF). This work is based upon experiments performed at the SPODI instrument operated by A. Senyshyn, and experiments performed at the PGAA instrument operated by P. Kudějová at the Heinz Maier-Leibnitz Zentrum (MLZ), Garching, Germany. The authors thank the Institut Laue-Langevin, Grenoble, France, for the allocation of neutron beam time. MFI would like to thank Prof Dr Andreas Lüttge and Dr Rolf Arvidson (Marum, Bremen) for generous access to the Asgard cluster, and the Central Research Development Fund (CRDF) of the University of Bremen for funding (Funding line 04 – Independent Projects for Post-Docs). We gratefully thank the Shikoku Chemical Corporation (Japan) for providing the Alborite and Alborex samples.

Supplementary information

Following the complete series of the measured IR and Raman spectra are displayed. These spectra represent supplementary information not being component of the manuscript. The discussion about the respective vibration modes is given within chapter 6.

Appendix A

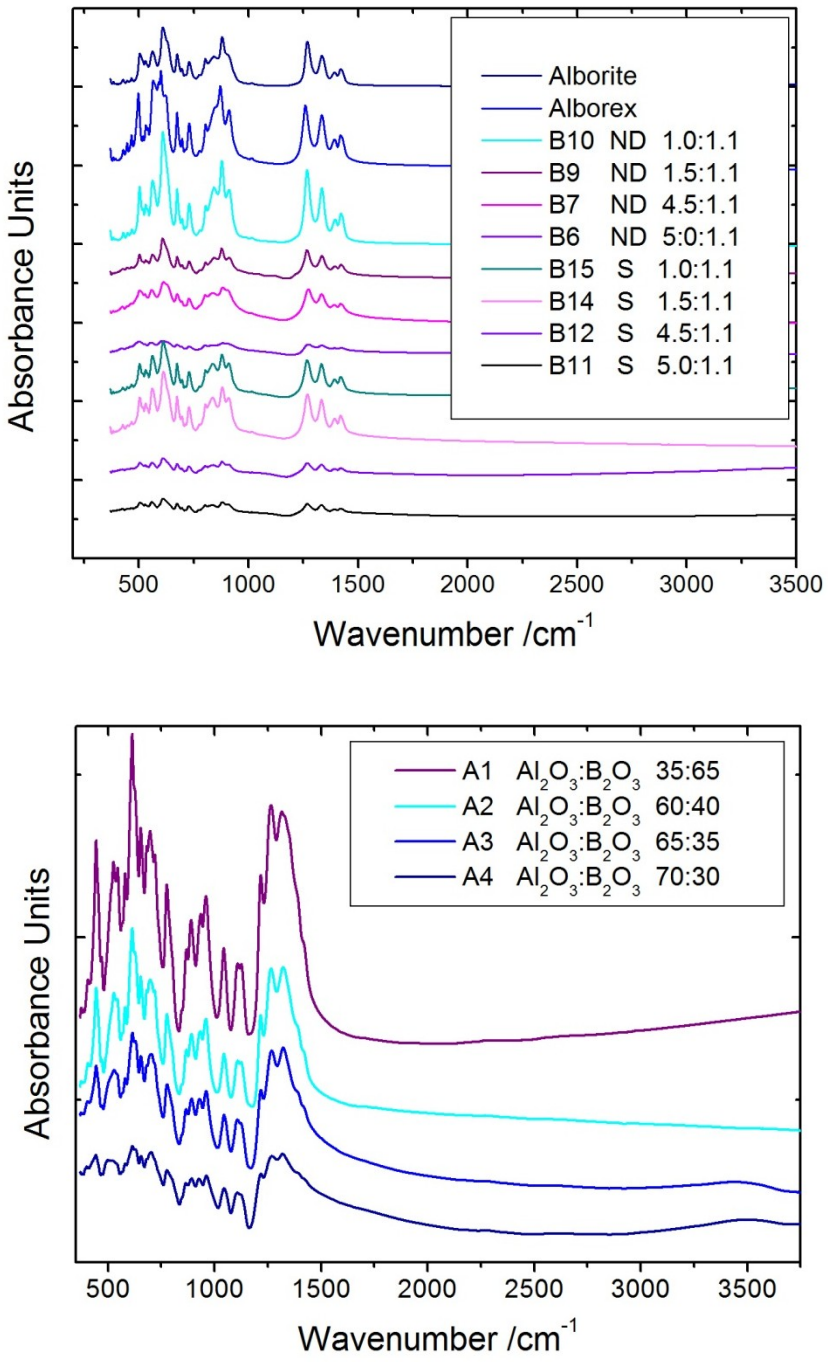

Figure S.6.1. Completed representation of all measured IR spectra for samples of the $Al_{5-x}B_{1+x}O_9$ series (top) and the $Al_4B_2O_9$ series (bottom).

Appendix B

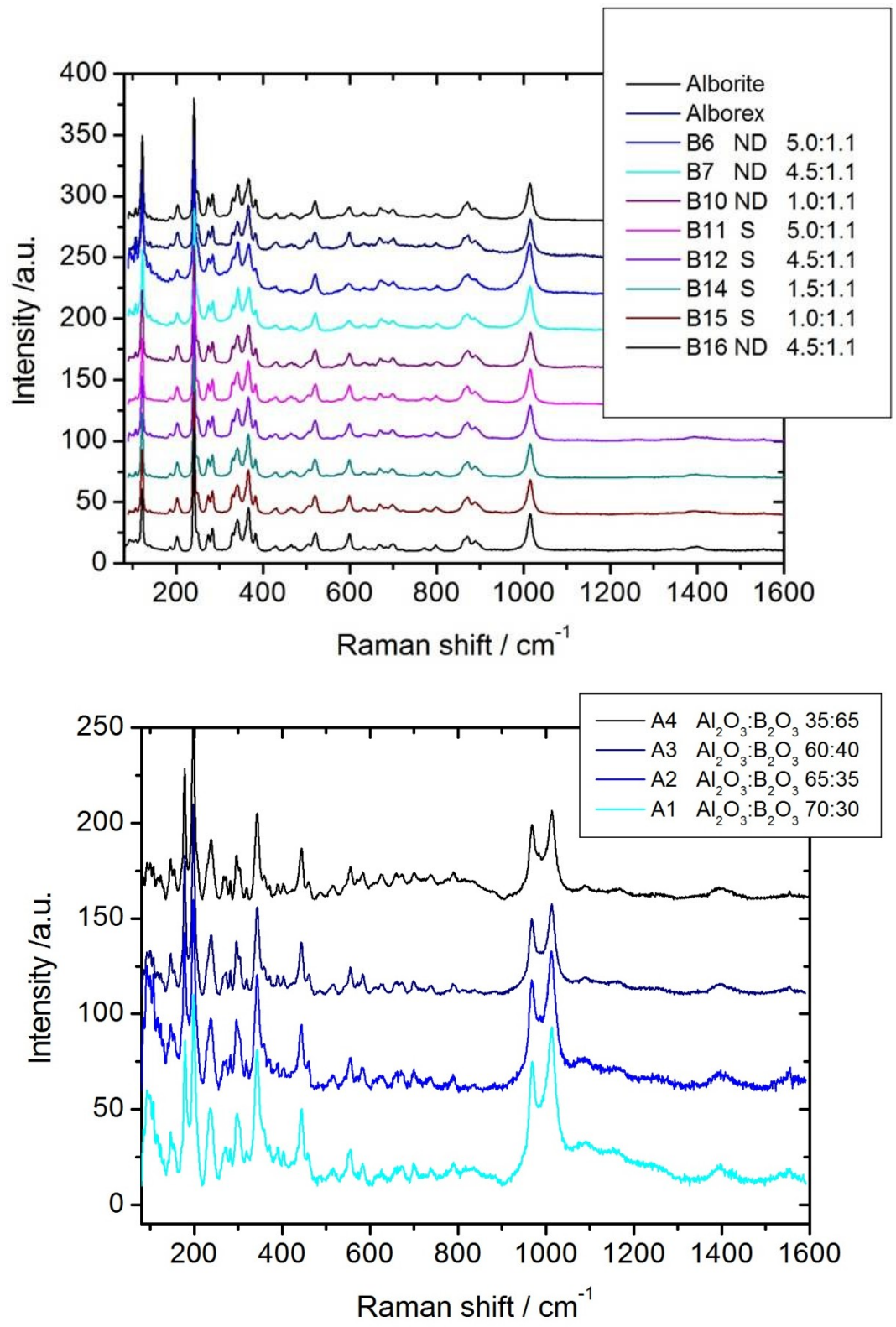

Figure S.6.2. Completed representation of all measured Raman spectra for samples of the $Al_{5-x}B_{1+x}O_9$ series (top) and the $Al_4B_2O_9$ series (bottom).

7 Conclusions and future perspectives

In the following the results of the chapters 4 - 6 are cross-summarized with respect to the given objectives:

Objective 1: The formation process of $Al_{18}B_4O_{33}$ (Al_5BO_9), $Al_4B_2O_9$ and $Al_{6-x}B_xO_9$

The formation of aluminum borate compounds synthesized from sol-gel precursors was investigated combining the results of HT-XRD and DTA methods with a special focus on the compositional range between the technically relevant compounds $Al_4B_2O_9$ and $Al_{18}B_4O_{33}$ (found to be better described as $Al_{5-x}B_{1+x}O_9$, c.f. objective 4). Upon increasing initial boron content a decrease of the formation temperature is observed revealed by thermal analyses, representing the formation of $Al_{6-x}B_xO_9$ compounds. In the high and low B_2O_3 region monoclinic A_2B and orthorhombic A_9B_2 are formed, respectively. HT-XRD experiments show $Al_{6-x}B_xO_9$ to be stable up to 1280 K, gradually transforming into A_9B_2, or into A_2B and A_9B_2 for samples with an initial composition near $x = 2$. An anomalous behave is observed for samples with the A_9B_2 structure in the high Al_2O_3 region compared to A_9B_2 compounds synthesized with an excess of boron (c.f. objective 4).

Objective 2: Detailed analyses of the crystal structure of $Al_4B_2O_9$ and analogous studies on $Ga_4B_2O_9$

The crystal structure of $Al_4B_2O_9$ was re-evaluated by electron diffraction experiments, resolving the question of oxygen disorder in the channels. Inside crystallites the structural details vary, showing domains with an ordered distribution of atoms without any significant signal for the second postulated channel oxygen atom O5, and other domains with a probable disordered configuration of O5 and O10. The later ones are indicated by diffuse scattering along the **b**-direction.

For the first time structural differences were investigated for samples with $Al_4B_2O_9$ structure dependent on a varying initial Al/B ratio, combining X-ray diffraction and NMR spectroscopy. A slight increase of BO_4 is determined relatively to BO_3 upon increasing initial boron content, accompanied by a slightly increasing cell volume. Although it is likely that the variations in the cell dimensions are based on the structural differences observed in the spectroscopic data, minor differences in the chemical composition might be possible, as this is observed for the related phases in the Al_2O_3-B_2O_3 system. Therefore it would be interesting to investigate the chemical composition for a series if samples, synthesized with various initial Al/B ratios. Further electron diffraction experiments might be useful in case of chemical differences.

For the first time a study on $(Al_{1-x}Ga_x)_4B_2O_9$ compounds is presented, illustrating the successful incorporation of about 70 mol% Al^{3+} and Ga^{3+} into the G_2B and A_2B structure, respectively. It is illustrated that the incorporation of the cations has a clear influence on the thermal behaviour of both

structures, improving the thermal stability of the gallium borate phase upon substitution of aluminum and reducing the decomposition temperature of the aluminum borate phase successively by substituting Al^{3+} by Ga^{3+}. It could be shown that the incorporation limit of gallium in the A_2B structure could be increased by varying the conditions of synthesis. Additional experiments would be interesting to find out if the incorporation limit could be increased furthermore and, with respect on the improvement on the thermal stability, if the substitution limit of aluminum in the G_2B structure could be improved.

Objective 3: Crystal structure analyses of the metastable compounds $Al_{6-x}B_xO_9$

It could be shown that the conditions for synthesis of $Al_{6-x}B_xO_9$ are best using a crystallisation temperature of 1173 K and a dwelling period of 6h. The lattice parameters represent an orthorhombic metric with $a \neq b$. Upon increasing boron content a continuous decrease of the lattice parameters is observed, most pronounced in **c**-direction. This and the results of NMR spectroscopy indicate a complete solid solution series with B substituting Al for samples synthesized in the compositional range of $1.09 \leq x \leq 2$. As shown by the ^{11}B NMR spectra and Difference Fourier calculations B occurs preferred in trigonal planar coordination.

An optimized theoretical crystal structure model for $Al_{6-x}B_xO_9$ is presented based on DLS refinements. Split positions for the oxygen atoms were calculated to simulate local geometries avoiding long B-O distances for the case that two octahedral chains are linked by a BO_3 group. The strong B-O bonds of the BO_3 groups lead to a distortion of neighboring octahedral, most probably causing the decrease of the cell parameters. Structure refinements with split positions in a lower symmetry are not possible due to significantly broadened and therefore overlapping diffraction peaks, caused by a very small crystallite size. Further experiments should be performed with the purpose to increase the crystallite size. The relative low synthesis temperature cannot be increased due to the transformation into the thermodynamically more ordered polymorphs. Therefore, an extended dwelling period should be used. To avoid a major loss of the volatile boron during the synthesis those experiments should be performed in a closed system, using e.g. sealed platinum capsules.

Objective 4: The compositional and thermal stability range of $Al_{18}B_4O_{33}$ / $Al_{20}B_4O_{36}$

Dependent on the results obtained by PGA analysis and NMR spectroscopy the compositional range for the Al-rich aluminum borate was assumed to be described as solid solution series $Al_{5-x}B_{1+x}O_9$, with boron substituting aluminum in the range of about 1 – 3 %. This is supported by the powder-diffraction experiments, observing 3.3(6) % vacancy on the Al2 site in a combined refinement of neutron and X-ray diffraction data.

X-ray diffraction experiments represent various broadened or narrowed diffraction peaks for samples synthesized from sol-gel precursors with a high amount of aluminum. This behavior varies within hkl series of different order and is assumed to be caused by disorder effects in the structure. ^{27}Al NMR confirm an increased disorder for these samples represented in a varying ratio of AlO_4/AlO_5 compared to $Al_{5-x}B_{1+x}O_9$ samples synthesized with a higher initial boron content and/or higher crystallizing temperature. In further experiments samples should be synthesized with an excess of alumina and an extended dwelling period to investigate a probable ordering process, correlating with impurities of amorphous alumina, if present.

A complete decomposition of the aluminum borate compound is observed for continuous heat treatment at 1673 K, as revealed by thermal analyses and X-ray diffraction. Incongruent melting is observed. Decomposition at 1473 K is likely, as a representative amount of alumina is observed after a dwell period of 44h. With respect to the technically relevance of this compound it would be interesting to proof the long-term stability in additional experiments successively varying the dwelling temperature and the dwelling period.

8 References

1. Fischer, R.X. and H. Schneider (2005): *The mullite-type family of crystal structures*, in: *Mullite*, H. Schneider and S. Komarneni, Editors., Wiley – VCH, Weinheim. p. 1-46, 128-140.

2. Fischer, R.X. and H. Schneider (2008): *Crystal chemistry of borates and borosilicates with mullite-type structures: a review.* European Journal of Mineralogy, **20**(5): p. 917-933.

3. Werding, G. and W. Schreyer (1984): *Alkali-free tourmaline in the system MgO-Al_2O_3-B_2O_3-SiO_2-H_2O.* Geochimica et Cosmochimica Acta, **48**(6): p. 1331-1344.

4. Bowen, N. and J. Greig (1924): *The system: Al_2O_3-SiO_2.* Journal of the American Ceramic Society, **7**(4): p. 238-254.

5. Schneider, H. (2005): *General introduction*, in: *Mullite,* H. Schneider and S. Komarneni, Editors., Wiley-VCH, Weinheim.

6. Schneider, H. (2005): *Basic Properties of Mullite*, in: *Mullite*, H. Schneider and S. Komarneni, Editors., Wiley-VCH, Weinheim. p. 141-225.

7. Fischer, R.X., H. Schneider, and M. Schmücker (1994): *Crystal structure of Al-rich mullite.* American Mineralogist, **79**: p. 983-990.

8. Fischer, R.X., H. Schneider, and D. Voll (1996): *Formation of aluminum rich 9:1 mullite and its transformation to low alumina mullite upon heating.* Journal of the European Ceramic Society, **16**(2): p. 109-113.

9. Fischer, R.X., A. Gaede-Köhler, J. Birkenstock, and H. Schneider (2012): *Mullite and mullite-type crystal structures.* International Journal of Materials Research, **103**(4): p. 402-407.

10. Shannon, R.D. (1976): *Revised Effective Ionic Radii and Systematic Studies of Interatomic Distances in Halides and Chalcogenides.* Acta Crystallographica A, **32**: p. 751-767.

11. Angel, R.J. and C.T. Prewitt (1986): *Crystal structure of mullite: A re-examination of the average structure.* American Mineralogist, **71**: p. 1476-1482.

12. Schneider, H. (2005): *Foreign cation incorporation in Mullite*, in: *Mullite*, H. Schneider and S. Komarneni, Editors., Wiley-VCH, Weinheim. p. 70-93, 128-140.

13. Scholze, H. (1956): *Über Aluminiumborate.* Zeitschrift für anorganische und allgemeine Chemie, **284**: p. 272-277 (in German).

14. Werding, G. and W. Schreyer (1996): *Experimental studies on borosilicates and selected borates.* Reviews in Mineralogy and Geochemistry, **33**(1): p. 117-163.

15. Alley, J.K. and R.C. Johnson, *Synthesis of aluminum borate whiskers*, in *U.S. patent 3350166*. 1967.

16. Reynaud, C. (1977): *Synthèse, analyse thermique et micrographie de nouveaux borates d'aluminium.* Bulletin de la Société Française de Minéralogie et de Cristallographie **100**: p. 28-32 (in French).

17. Lehmann, H.-A. and K. Teske (1973): *Über einige neue Borate des Aluminiums.* Zeitschrift für anorganische und allgemeine Chemie, **400**: p. 169-175 (in German).

18. Fisch, M. (2011): *Crystal chemistry of boron-bearing mullite-type compounds.* Dissertation Institut für Geologie, Universität Bern.

19. Kaduk, J.A., L.C. Satek, and S.T. McKenna (1999): *Crystal structures of metal aluminum borates.* The Rigaku Journal, **16**(2): p. 17-30.

20. Åhman, J., G. Svensson, and J. Grins (1997): *Lithium Aluminium Borate, $LiAl_7B_4O_{17}$.* Acta Chemica Scandinavica, **51**: p. 1045-1050.

21. Stephenson, D.A. and P.B. Moore (1968): *The crystal structure of grandidierite, $(Mg,Fe)Al_3SiBO_9$.* Acta Crystallographica Section B: Structural Crystallography and Crystal Chemistry, **24**(11): p. 1518-1522.

22. Hiroi, Y., E.S. Grew, Y. Motoyoshi, D.R. Peacor, R.C. Rouse, S. Matsubara, K. Yokoyama, R. Miyawaki, J.J. Mcgee, S.-C. Su, T. Hokada, N. Furukawa, and H. Shibasaki (2002): *Ominelite, $(Fe,Mg)Al_3BSiO_9$ (Fe^{2+} analogue of grandidierite), a new mineral from porphyritic granite in Japan.* American Mineralogist, **87**(1): p. 160-170.

23. Dzikowski, T.J., L.A. Groat, and E.S. Grew (2007): *The geometric effects of $^{V}Fe^{2+}$ for ^{V}Mg substitution on the crystal structures of the grandidierite-ominelite series.* American Mineralogist, **92**: p. 863-872.

24. Mazza, D., M. Vallino, and G. Busca (1992): *Mullite-type structures in the system Al_2O_3-Me_2O (Me = Na,K) and Al_2O_3-B_2O_3.* Journal of the American Ceramic Society, **75**(7): p. 1929-1934.

25. Fischer, R.X., V. Kahlenberg, D. Voll, K.J.D. MacKenzie, M.E. Smith, B. Schnetger, H.-J. Brumsack, and H. Schneider (2008): *Crystal structure of synthetic $Al_4B_2O_9$: A member of the mullite family closely related to boralsilite.* American Mineralogist, **93**: p. 918-927.

26. Garsche, M., E. Tillmanns, H. Almen, H. Schneider, and V. Kupcik (1991): *Incorporation of chromium into aluminium borate $9Al_2O_3{\cdot}2B_2O_3$ (A_9B_2).* European Journal of Mineralogy, **3**(5): p. 793-808.

27. Mazza, D., S. Ronchetti, A. Delmastro, M. Tribaudino, and W. Kockelmann (2001): *Silica-free mullite structures in the Al_2O_3-B_2O_3-P_2O_5 ternary system.* Chemistry of materials, **13**(1): p. 103-108.

28. Griesser, K.J., A. Beran, D. Voll, and H. Schneider (2008): *Boron incorporation into mullite.* Mineralogy and Petrology, **92**: p. 309-320.

29. Lührs, H., R.X. Fischer, and H. Schneider (2012): *Boron mullite: Formation and basic characterization.* Materials Research Bulletin, **47**(12): p. 4031-4042.

30. Lührs, H., A. Senyshyn, S.P. King, J.V. Hanna, H. Schneider, and R.X. Fischer (2013): *Neutron diffraction and ^{11}B solid state NMR studies of the crystal structure of B-doped mullite.* Zeitschrift für Kristallographie - Crystalline Materials, **228**(9): p. 457-466.

31. Park, H. and J. Barbier (2001): *$PbGaBO_4$, an orthoborate with a new structure-type.* Acta Crystallographica Section E: Structure Reports Online, **57**(9): p. i82-i84.

32. Park, H., J. Barbier, and R.P. Hammond (2003): *Crystal structure and polymorphism of $PbAlBO_4$.* Solid state sciences, **5**(4): p. 565-571.

33. Park, H., R. Lam, J. Greedan, and J. Barbier (2003): *Synthesis, crystal structure, crystal chemistry, and magnetic properties of $PbMBO_4$ (M= Cr, Mn, Fe): a new structure type exhibiting one-dimensional magnetism.* Chemistry of materials, **15**(8): p. 1703-1712.

34. Grew, E.S. and J.R. Hinthorne (1983): *Boron in sillimanite.* Science, **221**: p. 547-549.

35. Ihara, M., K. Imai, J. Fukunaga, and N. Yoshida (1980): *Crystal structure of boroaluminate, $9Al_2O_3 \cdot 2B_2O_3$.* Yogyo Kyokai Shi, **88**: p. 77-84.

36. Buick, I.S., E.S. Grew, T. Armbruster, O. Medenbach, M.G. Yates, G.E. Bebout, and G.L. Clarke (2008): *Boromullite, $Al_9BSi_2O_{19}$, a new mineral from granulite-facies metapelites, Mount Stafford, central Australia: a natural analogue of a synthetic "boron-mullite".* European Journal of Mineralogy, **20**(5): p. 935-950.

37. Peacor, D.R., R.C. Rouse, and E.S. Grew (1999): *Crystal structure of boralsilite and its relation to a family of boroaluminosilicates, sillimanite, and andalusite.* American Mineralogist, **84**: p. 1152-1161.

38. Grew, E.S., H.A. Graetsch, B. Pöter, M.G. Yates, I. Buick, H.-J. Bernhardt, W. Schreyer, G. Werding, C.J. Carson, and G.L. Clarke (2008): *Boralsilite, $Al_{16}B_6Si_2O_{37}$, and "boron-mullite:" Compositional variations and associated phases in experiment and nature.* American Mineralogist, **93**(2-3): p. 283-299.

39. Moore, J.M., D.J. Waters, and M.L. Niven (1990): *Werdingite, a new borosilicate mineral from the granulite facies of the western Namaqualand metamorphic complex, South Africa.* American Mineralogist, **75**(3-4): p. 415-420.

40. Grew, E.S., M.G. Yates, J.P. Huijsmans, J.J. McGee, C.K. Shearer, M. Wiedenbeck, and R.C. Rouse (1998): *Werdingite, a borosilicate new to granitic pegmatites.* The Canadian Mineralogist, **36**(2): p. 399-414.

41. Werding, G. and W. Schreyer (1992): *Synthesis and stability of werdingite, a new phase in the system MgO-Al_2O_3-B_2O_3-SiO_2 (MABS), and another new phase in the ABS-system.* European journal of mineralogy, **4**(1): p. 193-207.

42. Niven, M.L., D.J. Waters, and J.M. Moore (1991): *The crystal structure of werdingite, $(Mg, Fe)_2Al_{12}(Al, Fe)_2Si_4(B,Al)_4O_{37}$, and its relationship to sillimanite, mullite, and grandidierite.* American Mineralogist, **76**(1-2): p. 246-256.

43. Gielisse, P.J.M. and W.R. Foster (1962): *The system Al_2O_3-B_2O_3.* Nature, **195**: p. 69-70.

44. Zhang, J., J. Lin, H.S. Song, E.M. Elssfah, S.J. Liu, J.J. Luo, X.X. Ding, C. Tang, and S.R. Qi (2006): *Bulk-quantity fast production of $Al_4B_2O_9$/$Al_{18}B_4O_{33}$ single-crystal nanorods by a novel technique.* Materials Letters, **60**: p. 3292–3295.

45. Baumann, H.N. and C.H. Moore (1942): *Electric Furnace Boroaluminate* Journal of the American Ceramic Society, **25**(14): p. 391-394.

46. Sokolova, Y.V., A.V. Azizov, M.A. Simonov, N.I. Leonyuk, and N.V. Belov (1978): *Crystal structure of synthetic ortho-3-borate $Al_5(BO_3)O_6$.* Doklady Akademii Nauk SSSR, **243**: p. 655-658 (in Russian).

47. Gatta, G.D., N. Rotiroti, M. Fisch, and T. Armbruster (2010): *Stability at high pressure, elastic behavior and pressure-induced structural evolution of ''Al_5BO_9'', a mullite-type ceramic material.* Physics and Chemistry of Minerals, **37**: p. 227–236.

48. Fisch, M., T. Armbruster, D. Rentsch, E. Libowitzky, and T. Pettke (2011): *Crystal-chemistry of mullite-type aluminoborates $Al_{18}B_4O_{33}$ and Al_5BO_9: A stoichiometry puzzle.* Journal of Solid State Chemistry, **184**: p. 70-80.

49. Rymon-Lipinski, T., H.W. Hennicke, and W. Lingenberg (1985): *Zersetzung von $9Al_2O_3 \cdot 2B_2O_3$ bei hohen Temperaturen.* Keramische Zeitschrift, **37**(9): p. 450-453.

50. Birkenstock, J., R.X. Fischer, and T. Messner (2006): *BRASS 2, The Bremen Rietveld Analysis and Structure Suite.* Zeitschrift für Kristallographie, Supplementary, **23**: p. 237-242.

51. Massiot, D., F. Fayon, M. Capron, I. King, S. Le Calvé, B. Alonso, J.O. Durand, B. Bujoli, Z. Gan, and G. Hoatson (2002): *Modelling one-and two-dimensional solid-state NMR spectra.* Magnetic Resonance in Chemistry, **40**(1): p. 70-76.

52. Kemp, T.F. and M.E. Smith (2009): *QuadFit—a new cross-platform computer program for simulation of NMR line shapes from solids with distributions of interaction parameters.* Solid state nuclear magnetic resonance, **35**(4): p. 243-252.

53. NETZSCH, *NETZSCH Proteus - Thermal Analysis*. 2010, NETZSCH Gerätebau GmbH: Selb / Bayern.

54. Anovitz, L.M. and E.S. Grew (1996): *Mineralogiy, Petrology and Geochemistry of Boron: An Introduction*, in: *Boron - Mineralogy, Petrology and Geochemistry. Reviews in Mineralogy Volume 33*.

55. Söllradl, S., H. Lührs, Z. Révay, P. Kudějová, L. Canella, and A. Türler (2013): *Increasing the dynamic range for the analysis of boron in PGAA.* Journal of Radioanalytical and Nuclear Chemistry, **298**(3): p. 2069-2073.

56. Fazekas, B., T. Belgya, L. Dabolczi, G. Molnár, and A. Simonits (1996): *HYPERMET-PC: Program for automated analysis of complex gamma-ray spectra.* Journal of trace and microprobe techniques, **14**(1): p. 167-172.

57. Révay, Z. (2009): *Determining elemental composition using prompt γ activation analysis.* Analytical Chemistry, **81**(16): p. 6851-6859.

58. Baerlocher, C., A. Hepp, and W.M. Meier, *DLS-76, a program for the simulation of crystal structures by geometric refinements*. 1977: ETH Zürich, Switzerland.

59. Cong, R., T. Yang, K. Li, H. Li, L. You, F. Liao, Y. Wang, and J. Lin (2010): *Mullite-type $Ga_4B_2O_9$: structure and order-disorder phenomenon.* Acta Crystallographica, **B66**: p. 141-150

60. Hoffmann, K., M.M. Murshed, R.X. Fischer, H. Schneider, and T.M. Gesing (2014): *Synthesis and characterization of mullite-type $(Al_{1-x}Ga_x)_4B_2O_9$.* Zeitschrift für Kristallographie - Crystalline Materials, **229**(10): p. 699-708.

61. Gesing, T.M., R.X. Fischer, M. Burianek, M. Mühlberg, T. Debnath, C.H. Rüscher, J. Ottinger, J.-C. Buhl, and H. Schneider (2011): *Synthesis and properties of mullite-type $(Bi_{1-x}Sr_x)_2(M^{11-y}M^{2y})_4O_{9-x}$ (M = Al, Ga, Fe).* Journal of the European Ceramic Society, **31**: p. 3055-3062.

62. Robben, L. 2014, personal communication.

63. Brese, N.E. and M. O'Keeffe (1991): *Bond-Valence Parameters for Solids.* Acta Crystallographica **B47**: p. 192-197.

64. Brunauer, G., F. Frey, H. Boysen, and H. Schneider (2001): *High temperature thermal expansion of mullite: an in situ neutron diffraction study up to 1600 °C.* Journal of the European Ceramic Society, **21**: p. 2563–2567.

65. Schneider, H. and E. Eberhard (1990): *Thermal expansion of mullite.* Journal of the American Ceramic Society, **73**(7): p. 2073-2076.

66. Fisch, M. and T. Armbruster (2012): *Thermal Expansion of Aluminoborates*, in: *Minerals as Advanced Materials II*, S.V. Krivovichev, Editor. p. 255-268.

67. Murshed, M.M. and T.M. Gesing (2013): *Anisotropic thermal expansion and anharmonic phonon behavior of mullite-type $Bi_2Ga_4O_9$.* Materials Research Bulletin, **48**(9): p. 3284-3291.

68. Schneider, H., J. Schreuer, and B. Hildmann (2008): *Structure and properties of mullite—a review.* Journal of the European Ceramic Society, **28**(2): p. 329-344.

69. Ju, J., T. Yang, G. Li, F. Liao, Y. Wang, L. You, and J. Lin (2004): *PKU-5: An Aluminoborate with Novel Octahedral Framework Topology.* Chemistry - A European Journal, **10**(16): p. 3901-3906.

70. Vegas, A., F.H. Cano, and S. Garcia-Blanco (1977): *Refinement of aluminium orthoborate.* Acta Crystallographica Section B: Structural Crystallography and Crystal Chemistry, **33**(11): p. 3607-3609.

71. Douy, A. (2005): *Aluminium borates: synthesis via a precipitation process and study of their formation by DSC analysis.* Solid State Sciences, **7**: p. 117-122.

72. Hoelzel, M., A. Senyshyn, and O. Dolotko (2015): *SPODI: High resolution powder diffractometer.* Journal of large-scale research facilities JLSRF, **1**: p. A5.

73. Gesing, T.M., C.B. Mendive, M. Curti, D. Hansmann, G. Nénert, P.E. Kalita, K.E. Lipinska, A. Huq, A.L. Cornelius, and M.M. Murshed (2013): *Structural properties of mullite-type $Pb(Al_{1-x}Mn_x)BO_4$.* Zeitschrift für Kristallographie - Crystalline Materials, **228**(10): p. 532-543.

74. Lippmaa, E., A. Samoson, and M. Mägi (1986): *High-resolution ^{27}Al NMR of aluminosilicates.* Journal of the American Chemical Society, **108**(8): p. 1730-1735.

75. Rowles, M., J.V. Hanna, K. Pike, M.E. Smith, and B. O'Connor (2007): *^{29}Si, ^{27}Al, ^{1}H and ^{23}Na MAS NMR study of the bonding character in aluminosilicate inorganic polymers.* Applied Magnetic Resonance, **32**(4): p. 663-689.

76. Révay, Z., P. Kudějová, K. Kleszcz, S. Söllradl, and C. Genreith (2015): *In-beam activation analysis facility at MLZ, Garching.* Nuclear Instruments and Methods in Physics Research Section A: Accelerators, Spectrometers, Detectors and Associated Equipment, **799**: p. 114-123.

77. Révay, Z. (2015): *PGAA: Prompt gamma and in-beam neutron activation analysis facility.* Journal of large-scale research facilities, **1**(A20).

78. Zhang, G., Z. Fu, Y. Wang, H. Wang, W. Wang, J. Zhang, S.W. Lee, and K. Niihara (2010): *Boron-doped mullite derived from single-phase gels.* Journal of the European Ceramic Society, **30**(12): p. 2435-2441.

79. MacKenzie, K.J.D., M.E. Smith, T.F. Kemp, and D. Voll (2007): *Crystalline Aluminum Borates with the Mullite Structure: A ^{11}B and ^{27}Al Solid-State NMR Study.* Applied Magnetic Resonance, **32**: p. 647-662.

80. Massiot, D., D. Müller, T. Hübert, M. Schneider, A. Kentgens, B. Coté, J. Coutures, and W. Gessner (1995): *Double rotation and magic-angle spinning nuclear magnetic resonance study*

of ^{27}Al: reexamination of the aluminium borate $9Al_2O_3 \cdot 2B_2O_3$. Solid state nuclear magnetic resonance, **5**(2): p. 175-180.

81. Hung, I., A.P. Howes, T. Anupõld, A. Samoson, D. Massiot, M.E. Smith, S.P. Brown, and R. Dupree (2006): *^{27}Al double rotation two-dimensional spin diffusion NMR: Complete unambiguous assignment of aluminium sites in $9Al_2O_3 \cdot 2B_2O_3$.* Chemical Physics Letters, **432**(1): p. 152-156.

82. Merwin, L., A. Sebald, H. Rager, and H. Schneider (1991): *^{29}Si and ^{27}Al MAS NMR spectroscopy of mullite.* Physics and chemistry of minerals, **18**(1): p. 47-52.

83. MacKenzie, K.J.D. (2005): *Spectroscopy of mullite and compounds with mullite-related structures*, in: *Mullite*, H. Schneider and S. Komarneni, Editors., Wiley – VCH, Weinheim. p. 189-225.

84. Gesing, T.M., M. Schowalter, C. Weidenthaler, M.M. Murshed, G. Nénert, C.B. Mendive, M. Curti, A. Rosenauer, J.-C. Buhl, and H. Schneider (2012): *Strontium doping in mullite-type bismuth aluminate: a vacancy investigation using neutrons, photons and electrons.* Journal of Materials Chemistry, **22**(36): p. 18814-18823.

85. Murshed, M.M., A. Rusen, R.X. Fischer, and T.M. Gesing (2012): *Transition-metal substitution in $PbAlBO_4$: Synthesis, structural and spectroscopic studies of manganese containing phases.* Materials Research Bulletin, **47**(6): p. 1323-1330.

86. Senyshyn, A., H. Boysen, R. Niewa, J. Banys, M. Kinka, Y. Burak, V. Adamiv, F. Izumi, I. Chumak, and H. Fuess (2012): *High-temperature properties of lithium tetraborate Li2B4O7.* Journal of Physics D: Applied Physics, **45**(17): p. 175305.

87. Murshed, M.M., C.B. Mendive, M. Curti, M. Šehović, A. Friedrich, M. Fischer, and T.M. Gesing (2015): *Thermal expansion of mullite-type $Bi_2Al_4O_9$: A study by X-ray diffraction, vibrational spectroscopy and density functional theory.* Journal of Solid State Chemistry, **229**: p. 87-96.

88. Murshed, M.M., C.B. Mendive, M. Curti, G. Nénert, P.E. Kalita, K. Lipinska, A.L. Cornelius, A. Huq, and T.M. Gesing (2014): *Anisotropic lattice thermal expansion of $PbFeBO_4$: A study by X-ray and neutron diffraction, Raman spectroscopy and DFT calculations.* Materials Research Bulletin, **59**: p. 170-178.

89. Schreuer, J., M. Burianek, M. Mühlberg, B. Winkler, D.J. Wilson, and H. Schneider (2006): *Crystal growth and elastic properties of orthorhombic Bi2Ga4O9.* Journal of Physics: Condensed Matter, **18**(48): p. 10977.

90. Krenzel, T.F., J. Schreuer, T.M. Gesing, M. Burianek, M. Mühlberg, and H. Schneider (2012): *Thermal expansion and elastic properties of mullite-type Bi2Ga4O9 and Bi2Fe4O9 single crystals.* International Journal of Materials Research, **103**(4): p. 438-448.

91. López-de-la-Torre, L., A. Friedrich, E.A. Juarez-Arellano, B. Winkler, D.J. Wilson, L. Bayarjargal, M. Hanfland, M. Burianek, M. Mühlberg, and H. Schneider (2009): *High-pressure behavior of the ternary bismuth oxides Bi2Al4O9, Bi2Ga4O9 and Bi2Mn4O10.* Journal of Solid State Chemistry, **182**(4): p. 767-777.

92. Hoffmann, K., T.J.N. Hooper, M.M. Murshed, O. Dolotko, Z. Révay, A. Senyshyn, H. Schneider, J.V. Hanna, T.M. Gesing, and R.X. Fischer (2016): *Formation, stability and crystal structure of mullite-type $Al_{6-x}B_xO_9$* Journal of Solid State Chemistry, **243**: p. 124-135.

93. Tang, C.C., E.M. Elssfah, J. Zhang, and D.F. Chen (2006): *Morphology-and composition-controlled synthesis of aluminium borate nanowires without catalysts.* Nanotechnology, **17**(9): p. 2362-2367.

94. Peng, L.M., X.K. Li, H. Li, J.H. Wang, and M. Gong (2006): *Synthesis and microstructural characterization of aluminum borate whiskers.* Ceramics International, **32**: p. 365–368.

95. Tao, X., X. Wang, and X. Li (2007): *Nanomechanical characterization of one-step combustion-synthesized $Al_4B_2O_9$ and $Al_{18}B_4O_{33}$ nanowires.* Nano letters, **7**(10): p. 3172-3176.

96. Gesing, T.M., C. Mendive, M. Curti, D. Hansmann, G. Nénert, P. Kalita, K. Lipinska, A. Huq, A. Cornelius, and M. Murshed (2013): *Structural properties of mullite-type $Pb(Al_{1-x}Mn_x)BO_4$.* Zeitschrift für Kristallographie-Crystalline Materials, **228**(10): p. 532-543.

97. Murshed, M.M., R.X. Fischer, and T.M. Gesing (2012): *The role of the Pb^{2+} lone electron pair for bond valence sum analysis in mullite-type $PbMBO_4$ (M= Al, Mn and Fe) compounds.* Zeitschrift für Kristallographie-Crystalline Materials, **227**(8): p. 580-584.

98. Murshed, M.M., G. Nénert, and T.M. Gesing (2012): *Crystal structure of mullite-type $Pb(Mn_{0.5}Al_{0.5})BO_4$ determined by combined X-ray and neutron diffraction data.* Zeitschrift für Kristallographie-New Crystal Structures, **227**(3): p. 285-286.

99. Shikoku Chemical Corporation, Certificate of Analysis (Alborite PF03 and Alborex Y) 2008

100. Kolb, U., T. Gorelik, C. Kübel, M. Otten, and D. Hubert (2007): *Towards automated diffraction tomography: Part I—Data acquisition.* Ultramicroscopy, **107**(6): p. 507-513.

101. Clark, S.J., M.D. Segall, C.J. Pickard, P.J. Hasnip, M.I. Probert, K. Refson, and M.C. Payne (2005): *First principles methods using CASTEP.* Zeitschrift für Kristallographie - Crystalline Materials, **220**(5/6): p. 567-570.

102. Perdew, J.P., A. Ruzsinszky, G.I. Csonka, O.A. Vydrov, G.E. Scuseria, L.A. Constantin, X. Zhou, and K. Burke (2008): *Restoring the density-gradient expansion for exchange in solids and surfaces.* Physical Review Letters, **100**(13): p. 136406.

103. Révay, Z. (2015): *PGAA: Prompt gamma and in-beam neutron activation analysis facility.* Journal of large-scale research facilities JLSRF, **1**: p. A20.

104. Ishizawa, N., T. Miyata, I. Minato, F. Marumo, and S.I. Iwai (1980): *A structural investigation of α-Al_2O_3 at 2170 K.* Acta Crystallographica Section B: Structural Crystallography and Crystal Chemistry, **36**(2): p. 228-230.

105. Kolb, U., E. Mugnaioli, and T. Gorelik (2011): *Automated electron diffraction tomography – a new tool for nano crystal structure analysis.* Crystal Research and Technology, **46**(6): p. 542-554.

106. Zhao, H., Y. Krysiak, K. Hoffmann, B. Barton, L. Molina-Luna, R. Neder, H.-J. Kleebe, T.M. Gesing, H. Schneider, R.X. Fischer, and U. Kolb *Elucidating structural order and disorder phenomena in mullite-type $Al_4B_2O_9$ by automated electron diffraction tomography.* in preparation.

107. Baur, W. (1974): *The geometry of polyhedral distortions. Predictive relationships for the phosphate group.* Acta Crystallographica Section B: Structural Crystallography and Crystal Chemistry, **30**(5): p. 1195-1215.

Acknowledgements

At this place I want to thank all the persons who contributed to the success of this work.

In the first place I want to thank Prof. Dr. Reinhard X. Fischer for the opportunity to carry out this work in his research group. I am grateful for his continuous support, constructive guidance and discussions and his hones interest in this research work. His advices and ideas brought this thesis to the present form.

My thanks also go to my second and third supervisors Prof. Dr. Thorsten M. Gesing and Prof. Dr. Hartmut Schneider for their scholastic suggestions, helpful discussions and careful monitoring of the resulting manuscripts. I am grateful for the opportunity to use all the lab facility of the cKfS group.

I gratefully thank Prof. Dr. Josef-Christian Buhl for agreeing to be the second reviewer of this thesis and for the opportunity to use the lab facility of his group at the Leibniz University of Hannover.

I would like to express my sincere thank to all my colleagues in the group crystallography and the cKfS group for their support and encouragement: Gabriele Ebert, Dr. Iris Spiess, Dr. Michael Fischer, Dr. Christoph Vogt, Dr. Manfred Burianek, Dr. Lars Robben; my special thanks go to PD Dr. M. Mangir Murshed, Dr. Michael Wendschuh and Dr. Johannes Birkenstock for challenging and promoting me in many constructive discussions and giving technical support at various instruments, and to Thomas Messner for continuous technical support using the BRASS software. My heartfelt thank to Julia and to all my PhD colleagues, to Irma, Shahidur, Pei, Li, Hanna, Stephan, Michael, Malik, Hilke, Andrea, Mathias, Nils and Ariane for their cordial help, their ears for my concerns and their inspirations. I was happy to be part of this team.

I gratefully thank Dr. John V. Hanna and Thomas Hooper (NMR, University of Warwick, UK) for providing the NMR data and for many helpful and constructive discussions. I thank Dr. O. Dolotko, Dr. A. Senyshyn (FRM II, Garching) and Dr. G. Nénert (ILL, Grenoble) for providing the neutron powder diffraction data, Dr. Zs. Révay and Dr. P. Kudějová (FRM II, Garching) for providing chemical analysis, H. Zhao and Dr. Ute Kolb (University of Mainz) for the collaboration and for providing the electron diffraction data and Dr. M. Fischer (University of Bremen) for providing the DFT calculations. Finally I would like to thank the University of Bremen for the granting of the postgraduate grant and the Deutsche Forschungsgemeinschaft for the financial support of the grants Fi442/19-1 and GE1981/5-1.

A special place is reserved for my family and my friends. With all my heart I want to say thank you to my parents and my sister Jenny. They put me on the right path and gave me the chance to pursue my passion for science. Their support and love has been unconditional all this time. Thank you to Andreas, Nicole, Julia, Lisa and to all my friends who come along with me in this time, who encouraged me and made sure that I keep in mind the things I love. You are the best!

Appendix

Appendix A

Elucidating structural order and disorder phenomena in mullite-type $Al_4B_2O_9$ by automated electron diffraction tomography

H. Zhao[a], Y. Krysiak[a], K. Hoffmann[b,c], B. Barton[a], L. Molina-Luna[d], R. Neder[e], H.-J. Kleebe[d], Th. M. Gesing[c,f], H. Schneider[b], R. X. Fischer[b,f], U. Kolb[a]

[a]Institute of Inorganic Chemistry and Analytical Chemistry, Johannes Gutenberg-University Mainz, Germany
[b]Crystallography, Department of Geosciences, University of Bremen, Bremen, Germany
[c]Institute of Inorganic Chemistry, University of Bremen, Bremen, Germany
[d]Department of Materials and Geoscience, Technische Universität, Darmstadt, Germany
[e]Department of Physics, Lehrstuhl für Kristallographie und Strukturphysik, Erlangen, Germany
[f]MAPEX Center for Materials and Processes, University of Bremen, Bremen, Germany

In preparation; will be submitted soon[7]

*Corresponding author; email address: hzhao@uni-mainz.de; phone: +49 (0)6131 3923 148

Abstract

Automated diffraction tomography (ADT), a new method for collection and analysis of electron diffraction data, was applied to investigate the crystal structure of $Al_4B_2O_9$, an aluminum borate from mullite family. $Al_4B_2O_9$, prepared with initial Al/B ratio of 35/65 by sol-gel approach, crystallizes in a monoclinic mullite-type structure in space group *C*2/*m*. "*Ab initio*" structure determination from three dimensional electron diffraction data of single ordered crystals reveals edge-connected AlO_6 octahedra expanding along **b** axis constituting the backbone of the structure. The ordered structure (*A*) was confirmed by HRTEM and HAADF-HRSTEM images. In addition, disordered crystals with diffuse scattering along **b** axis are observed. Analysis of the modulation pattern implies a mean superstructure (*ABA*) with a threefold **b** axis, where *B* is shifted ½ **a** and ½ **c** from *A*. Diffraction patterns simulated for *ABA* sequence including additional stacking disorder correspond to the experimental electron diffraction patterns.

[7] The related manuscript will be submitted to the Journal of Solid State Chemistry

Keywords: Electron crystallography; automated electron diffraction tomography; Aluminum borate; Crystal structure determination; Disorder

Supplementary CD

Content of the supplementary CD:

- digital version of the thesis

- *.cif files of the $(Al_{1-x}Ga_x)_4B_2O_9$ phases
  $(Al_{1-x}Ga_x)_4B_2O_9$ - A: CSD numbers 428199, 428202 – 428207
  $(Ga_{1-x}Al_x)_4B_2O_9$ - G: CSD numbers 428200 and 428201

- data of all measurements which were performed in the faculties Geoscience and Chemistry/Biology at the University of Bremen and at the Institute of Mineralogy at the Leibniz University of Hannover; this includes: diffraction data, FTIR data, Raman data and STA data

Erklärung

Versicherung an Eides Statt

gem. § 5 Abs. 5 der Promotionsordnung vom 15.07.2015

Ich,

_____

(Vorname, Name, Anschrift, Matr.-Nr.)

versichere an Eides Statt durch meine Unterschrift, dass ich die vorstehende Arbeit selbständig und ohne fremde Hilfe angefertigt und alle Stellen, die ich wörtlich dem Sinne nach aus Veröffentlichungen entnommen habe, als solche kenntlich gemacht habe, mich auch keiner anderen als der angegebenen Literatur oder sonstiger Hilfsmittel bedient habe, und die zu Prüfungszwecken beigelegte elektronische Version der Dissertation mit der abgegebenen gedruckten Version identisch ist.

Ich versichere an Eides Statt, dass ich die vorgenannten Angaben nach bestem Wissen und Gewissen gemacht habe und dass die Angaben der Wahrheit entsprechen und ich nichts verschwiegen habe.

Die Strafbarkeit einer falschen eidesstattlichen Versicherung ist mir bekannt, namentlich die Strafandrohung gemäß § 156 StGB bis zu drei Jahren Freiheitsstrafe oder Geldstrafe bei vorsätzlicher Begehung der Tat bzw. gemäß § 161Abs. 1 StGB bis zu einem Jahr Freiheitsstrafe oder Geldstrafe bei fahrlässiger Begehung.

_____ _____

Ort, Datum Unterschrift